

**Construction and Performance of a Liquid Argon Calorimeter
for Use in Experiment E-706
at the Fermi National Accelerator Laboratory**

by

William Edward DeSoi

Submitted in Partial Fulfillment

of the

Requirements for the Degree

DOCTOR OF PHILOSOPHY

Supervised by: Professor Frederick Lobkowicz

Department of Physics and Astronomy

College of Arts and Sciences

University of Rochester

Rochester, New York

1990

**Construction and Performance of a Liquid Argon Calorimeter
for Use in Experiment E-706
at the Fermi National Accelerator Laboratory**

by

William Edward DeSoi

Submitted in Partial Fulfillment

of the

Requirements for the Degree

DOCTOR OF PHILOSOPHY

Supervised by: Professor Frederick Lobkowicz

Department of Physics and Astronomy

College of Arts and Sciences

University of Rochester

Rochester, New York

1990

Curriculum Vitae

William Edward DeSoi [REDACTED]

He attended

Texas Agricultural and Mechanical University as an undergraduate where he received a B.A. in Physics and a B.A. in Mechanical Engineering in August 1981. He entered graduate school at the University of Rochester where he received a M.A. in Physics in May 1983. For the past 8 years he has been a member of the E706 collaboration at the Fermi National Accelerator Laboratory. During that time responsibilities included; design and supervision of construction work on the electromagnetic liquid argon calorimeter for E706. This included construction of two computer controlled routing and etching tables for the mass production of calorimeter parts and design analysis of the calorimeter's critical stress bearing members. Other responsibilities included the installation and testing of a cryogenic temperature and stress monitoring system for the calorimeter, shift work for data acquisition and monitoring of the cryogenic system, and computer analysis of data from the calorimeter for calibration

Abstract

The subject of this thesis is a liquid argon calorimeter developed by the E-706 collaboration. This device was used in measuring the energy content of showers produced by the interaction of nucleons with 530 GeV/c pions at the Fermi National Accelerator Laboratory. A description of the calorimeter's construction and design considerations precedes the analysis of its performance, which is the central topic to be discussed. The calorimeter was found to have an intrinsic energy for electromagnetic showers of $14.5\%/\sqrt{E}$ and for hadronic showers a resolution of $183\%/\sqrt{E}$. The position resolution of showers for the calorimeter was found to be 1.0 mm or better for energies greater than 2.0 GeV.

Acknowledgements

I would like to thank my adviser, Prof. Frederick Lobkowicz, for his help and criticism which figured greatly in my work. I would like to acknowledge the work and help of everyone who has participated in the E706 collaboration. In particular I would like to thank Prof. Paul Slattery for his leadership as collaboration spokesman. I would like to thank Prof. Joey Huston and Dr. George Ginther for their guidance in the construction of the calorimeter. I would like to thank Chris Lirakis and Alex Sinanidas for many enlightening discussions on the construction of the Hadron Calorimeter and the reconstruction software associated with it. I would like to thank Dane Skow and Eric Prebys for their explanations of the Calorimeter Electronics and John Mansour for his help with the reconstruction software used for the electromagnetic Calorimeter.

I would also like to thank the Department of Energy, the National Science Foundation and the UGC of India for supporting the research program. Many thanks go also to Betty Cook and Betty Bauer who provided support and a much needed link with the university during my time at Fermilab. Finally I would like to express appreciation to my parents, who provided support in many ways over the years, and to my wife, who spent many hours proof reading my thesis.

Table of Contents

Chapter	page
I Motivation for Building the E-706 Spectrometer	1
I.1 Direct Single Photon Production	1
I.2 Direct Diphoton Production	5
I.3 Higher Twist Production of Direct Photons	8
I.4 Physics Goals of E-706	8
I.5 Production Rates and Background for Single Photon Production	9
I.5.1 Bremsstrahlung	10
I.5.2 Decays of Neutral Particles	10
I.5.3 Muon Beam Halo	11
I.6 Production Rates and Background for Diphoton Production	12
II Description of E-706 Experimental Setup	14
II.1 The M-West Beamline	15
II.1.1 The Cerenkov Beam Counter	17
II.1.2 The Calibration Magnet	18
II.1.3 The Interaction and Trigger Counters	19
II.2 Description of E-706 Tracking System	20
II.2.1 The Silicon Strip Detector	21
II.2.2 The Analysis Magnet	22
II.2.3 The Multi-Wire Proportional Chambers	22
II.3 Calorimetry	24
II.3.1 The LAC	24
II.3.2 The Forward Calorimeter	25
III Design Criteria for the Liquid Argon Calorimeter	28

III.1 Choice of Calorimeter Type	29
III.2 Design of the EMLAC	32
III.2.1 Determination of the EMLAC Depth	32
III.2.2 Selection of the EMLAC Argon Gap Thickness and Sampling Frequency	34
III.2.3 Selection of r/ϕ Focused Geometry for the EMLAC	39
III.2.4 Selection of the EMLAC Strip Width for γ/π^0 Separation	41
III.2.5 Determination of the EMLAC Front/Back Ratio	43
III.2.6 EMLAC Acceptance	44
III.3 Design of the HALAC	48
III.3.1 Determination of HALAC Depth	49
III.3.2 Selection of HALAC Argon Gap Thickness and Sampling Frequency	50
III.3.3 Selection of HALAC Pad Size	51
III.3.4 Selection of the HALAC Front to Back Ratio	52
III.4 Selection of Construction Materials	53
IV Physical Construction of the LAC	55
IV.1 Physical Description of the EMLAC	55
IV.1.1 The EMLAC Lead Absorber Sheets	56
IV.1.2 The EMLAC Charge Collection Boards	57
IV.1.3 The Structure of the EMLAC Central Stack	59
IV.1.4 The Structure of an EMLAC Quadrant	62
IV.1.5 The Final Assembly of the EMLAC	68
IV.2 The Physical Construction of the HALAC	68
IV.2.1 Description and Assembly of the Cookies	69
IV.2.2 Cookie Anode and Cathode Board Preparation	70
IV.2.3 Description of the Cookie G-10 Strips and Ribs	71

IV.2.4 Composition and Application of the Cookie Glue	71
IV.2.5 Assembly of a Cookie	72
IV.2.6 Description of the Cookie Support System	73
IV.2.7 Description of the HALAC Steel Structure	73
IV.2.8 The HALAC Steel Absorber Plates	74
IV.2.9 Installation of Sway Bars	76
IV.2.10 The HALAC Copper Fins	76
IV.2.11 The Installation of the Cookies	77
IV.2.12 The Alignment of the HALAC	77
IV.2.13 Patchboard Installation and Cabling the HALAC	78
IV.3 The Physical Construction of LAC Gantry	78
V The LAC Electronics System	82
V.1 The LAC High Voltage System	82
V.2 The LAC Readout Cables	84
V.3 The RABBIT Electronics Crates	85
V.3.1 Channel Amplifier Electronics	87
V.3.2 Signal Digitization	91
V.4 Description of Data Acquisition System	92
V.5 Description of the LAC Trigger Electronics	94
VI Adjustment of the LAC Parameters	96
VI.1 High Voltage Testing of the LAC	96
VI.2 Capacitance and Isolation Testing of Strips and Pads	97
VI.3 Monitoring of the Liquid Argon Purity	98
VI.4 History of the Electron Beam Calibration for the LAC	101
VI.5 Selection of the Before/After Timing Gate	101
VI.6 Electronic Sources of Energy Fluctuations	102

	viii
VI.7 Zero Suppression Window	103
VI.7.1 Pedestal Stability	106
VI.7.2 Measurement of the Amplifier Gains	109
VI.8 LAC Data Transfer Reliability	109
VI.9 Determination of the TVC Pedestals	110
VI.10 Image Charge Effects	111
VII Reconstruction of LAC showers into Photons and Hadrons	114
VII.1 Conversion of Raw ADC Data to Energy	114
VII.2 EMLAC Reconstruction	114
VII.2.1 Correction for Dead Strips	115
VII.2.2 Group and Peak Finding	115
VII.2.3 Gamma Construction	116
VII.2.4 Gamma Correlation and Photon Reconstruction	118
VII.3 Hadron Reconstruction	120
VII.3.1 Grouping Pads into Energy Clusters	122
VII.3.2 Reconstruction of Individual Hadrons from the Clusters	123
VII.3.3 Correct Energy for Shower Tail Losses	125
VII.3.4 Energy Correlation between the EMLAC and the HALAC	125
VII.3.5 Correct Energy for the $\frac{e}{h}$ Effect	126
VII.4 TVC Reconstruction	127
VIII Operational Performance of the LAC	128
VIII.1 The Calibration Beam	128
VIII.2 Electron Sample from the Run Data	129
VIII.3 Directionality Resolution	131
VIII.4 Timing Resolution	133

VIII.5 Particle Identification Using the EMLAC E_{front}/E_{total} Ratio	136
VIII.6 XY Position Resolution	139
VIII.6.1 EMLAC XY Position Resolution	139
VIII.6.2 HALAC XY Position Resolution	141
VIII.7 Uniformness of the Calorimeter's Energy Response	143
VIII.8 Linearity of Measured Energy	144
VIII.9 Results of E/P Analysis	147
VIII.10 Energy Resolution of the LAC	150
VIII.10.1 The Contribution of Incoherent Noise to the Energy Resolution	150
VIII.10.2 Intrinsic Resolution of the EMLAC	152
VIII.10.3 HALAC Energy Resolution	156
VIII.11 Analysis of the Rest Masses for the π^0 and η	156
VIII.12 Particle Detection Efficiency	158
IX Conclusions	162
IX.1 Summary of the Performance Characteristics of the LAC	162
IX.1.1 Comparison of LAC with other Liquid Argon Calorimeters	165
IX.2 Remaining Avenues of Investigation	167
IX.3 Changes in the LAC that would Improve Performance	168
Bibliography	170

List of Figures

Figure	page
1 Feynman Diagrams of the Primary Direct Photon Processes	2
2 Feynman Diagrams of the Primary Direct Diphoton Processes	6
3 Feynman Diagram of the Drell-Yan Process	7
4 Background Processes which mimic Direct Photons	9
5 Detector Layout of the E-706 Spectrometer	15
6 Distributions of $\delta p/p$ for MW Beamline Positive and Negative Beams	16
7 Plot of Cerenkov Pressure Curve for Positive Beam	18
8 Plane View of Trigger System Counters	20
9 Layout of Silicon Strip Detector and Target	22
10 Isometric Drawing of the Forward Calorimeter	26
11 Drawing of Two Types of Calorimeter Readout Schemes	30
12 Plot of the Accumulated Material Thickness in Radiation Lengths vs. Z Position for the E-706 Spectrometer	35
13 Effect of Argon Gap Thickness on Intrinsic Energy Resolution	38
14 Cut View Drawing of the EMLAC Illustrating R-Strip Focusing	40
15 Plot of the Probability that the Width of a Pi-Zero is less than the width of a Photon versus Strip Width	42
16 Diagram of a π^0 Decay	43
17 Plots of Energy Distributions for Different EMLAC Front/Back Ratios.	45
18 Examples of Layouts for Single Arm and Inclusive Experiments.	46
19 Plot of Lab Angle versus COM angle to Illustrate EMLAC Acceptance	47
20 Drawing of HALAC Pad Configuration	53

21	Drawing of the Physical Boundaries to the Sensitive Area for an EMLAC Quadrant	58
22	Layout Drawing of the EMLAC Anode Board Production Facility	60
23	Cross Section Drawing of an EMLAC Cell at the Outer Edge of the Calorimeter.	61
24	Examples of EMLAC readout boards	62
25	Isometric Drawing of the EMLAC with an Exploded View of One Quadrant	65
26	Drawing of the Assembly Jig Used for Assembling the EMLAC Quadrants	66
27	Cross Section Drawing of the EMLAC Quadrant Support	67
28	Exploded View of a HALAC Cell	70
29	Drawing of the HALAC Steel Structure	74
30	Illustration of the Dead Zone Created by the HALAC	75
31	Cut View of the LAC Gantry.	79
32	Schematic of EMLAC High Voltage System	84
33	Schematic of LAC Amplifier Showing Sample and Hold, TVC and Fastout Circuits	89
34	Drawing of Time Shift for a Second TVC Hit	90
35	Sample and Hold Time line	92
36	Flowchart of LAC Data Acquisition System	93
37	Voltage Curves of Argon Indicating Level of Contamination	99
38	LAC Signal Height Dependence on Width of Before/After Timing Gate	103
39	Distribution of EMLAC Channel Noise with and without Zero Suppression	104
40	Distribution of Pedestal Settings for a Crate of Amplifiers from Cold Start Data over a Two Week Period	105
41	LAC Channel Noise Distributions with Pedestal Subtracted	107
42	Channel Pedestal Shifts for the First Ewe of a Crate	108

43	Distribution of the Amplifier Gains for the LAC	110
44	Drawing of Image Charge signal with and without Diode Clipping	112
45	Drawing of Signal with Image Charge for Inner and Outer ϕ sections of the EMLAC	113
46	Distribution of Overlapping EMLAC Showers	117
47	Examples of the Correlation of One r Gamma to One ϕ Gamma	120
48	Example of the Correlation of One ϕ Gamma to Two r Gammas	121
49	Examples of the Three Hexagon Area Used for Reconstructing Hadrons	122
50	Location of Calibration Points for 25, 50, and 100 GeV/c Electron Beams	130
51	Reconstructed Tracks of a Zero Mass Pair	132
52	Distribution of EMREC Directionality for ZMP Electron showers Subtracted from the PWC Track Directionality	133
53	Distribution of TVC Timings for Photon Showers with a Directionality Cut	134
54	TVC Efficiency for Photon Showers as a Function of Energy	135
55	Plot of Directionality versus TVC Time for the Leading p_T Shower of an Event with a p_T Greater than 4 GeV	137
56	Comparison of E_{front}/E_{total} Distributions for ZMP Electrons and Pions from K_S^0 Decays	138
57	Plots of EMREC Shower Position Minus the PWC Projected Track Position for ZMP Electrons with Energy Greater than 10 GeV/c	140
58	Plot of the X,Y Position Resolutions for ZMP Electrons as a Function of Energy	142
59	Plot of the Distribution Width for the Square of the Distance Between the Projected ZMP Track Position and the EMLAC Shower Position versus the Z Position of the Projection Plane	143
60	Plots of the Projected HCREC Shower Position Subtracted from the EMREC Shower Position for Hadrons with Energy Greater than 10 GeV/c	144
61	Distribution of the Mean Reconstructed Energies for the LAC Calibration Points	145

62 Plot of LAC Energy versus Calibration Beam Momentum	146
63 Plot of Energy versus Momentum for ZMP Electrons	147
64 Plot of Shower Energy Divided by Track Momentum versus Track Momentum for ZMP Electrons	149
65 Plots of the Number of Strips in a ZMP Shower versus Energy for the Inner and Outer ϕ regions of the EMLAC	152
66 Plots of the Number of Pads in a Hadron Shower versus Energy the HALAC	153
67 Plot of $\sigma^2(E_r - E_\phi)$ vs Energy for Calibration Beam Electron Showers in the EMLAC	154
68 Plot of $\sigma^2(E_r - E_\phi)$ vs Energy for ZMP Electron and π^0 Photon Showers in the EMLAC	155
69 Plot of HALAC Energy Resolution from π^- Beam Calibration Studies	157
70 Plot of the Two Photon Invariant Mass for Photons with no Matching Tracks	158
71 Plot of Detection Efficiency of the LAC for all Linked Tracks	159
72 Plot of EMLAC ZMP Electron Detection Efficiency	161

List of Tables

Table	page
1 List of Spectrometer Detectors	14
2 Nominal MW Particle Production at 530 GeV/c per 1×10^{12} Interacting 800 GeV/c Protons	16
3 Tracking System Parameters	23
4 Thermal Contraction of EMLAC Construction Materials between 300 K and 88 K	64
5 EWE Data and Control Registers	86
6 Amplifier Design Criteria	87
7 Percent Charge Collection Efficiency of the LAC with the EMLAC at 2.5 KV and the HALAC at 3.0 KV	100
8 Calibration Beam Parameters	129

Introduction

The subject of this paper is the design, construction and operational characteristics of the liquid argon calorimeter used in Fermilab experiment E-706. This experiment is a fixed target experiment so the calorimeter was designed to subtend as much of the center of mass solid angle as possible. It was also optimized to measure the energy and position of electromagnetic showers because the principle focus of investigation for the experiment is direct photon physics. A description of the calorimeter's construction and design considerations precedes the analysis of its performance, which is the central topic to be discussed. The analysis of the calorimeter's performance starts by examining the fundamental quantities, such as channel noise, that are independent of software. It then proceeds to the more software dependent quantities, such as position and energy resolution, which define the performance of the detector. A chapter outline follows below.

Chapter I discusses the physics involved in E-706. This provides the motivation for constructing a calorimeter and details some of the constraints imposed on its design.

Chapter II describe the layout of the E-706 spectrometer and gives a brief description of each of the detector systems involved.

With chapter III the heart of the discussion about the calorimeter begins. Here the design parameters and how they were chosen are explained in great length. Chapter IV contains a physical description of the calorimeter and outlines its construction. Chapter V describes the electronics system used to gather data from the calorimeter.

Chapters VI, VII and VIII bring the paper to a conclusion. Chapter VI describes several of the tasks done to tune the operating parameters of the calorimeters. Chapter VII lays a foundation for Chapter VIII by briefly describing the software user for reconstructing the showers generated in the calorimeters. Chapter VIII outlines the performance characteristics of the calorimeters and is followed by the conclusions in Chapter IX.

Chapter I

Motivation for Building the E-706 Spectrometer

The primary goal of experiment E-706 is the study of high transverse momentum (p_T) direct photons produced in pion/nucleon reactions. High p_T direct photons are photons that proceed directly from the constituent parton interaction vertex of hadronic collisions with high transverse momentum " p_T " and are not the result of some subsequent secondary process such as particle decay or bremsstrahlung from a fragmenting parton. This chapter introduces the concepts of direct photon physics and the motivations for exploring such physics. It also contains a brief description of the background processes to the physics involved. Both of these subjects have heavily influenced the design of the liquid argon calorimeter (LAC) used in this experiment, which is the main subject of this thesis.

I.1 Direct Single Photon Production

There are two first order processes that contribute to the production of direct photons. They are the quark annihilation, $q\bar{q} \rightarrow \gamma g$, and Compton, $gg \rightarrow \gamma q$, diagrams (See Fig.1). In the Compton diagrams a gluon is always an incoming, never an outgoing particle. The opposite is true of the annihilation diagrams. Because direct photons are not accompanied by hadrons, i.e. do not undergo fragmentation^[1], they do not have the interpretation problems of the more common reactions $q\bar{q} \rightarrow gg$ or $qg \rightarrow qg$. In these processes both of the scattered partons fragment into jets of particles. The problems of accurately defining a jet and measuring its energy complicate the interpretation of hadronic jet data^[2]. Direct photons, on the other hand, by coupling directly to the parton scattering process, provide an uncluttered view of

[1] Partons, being bearers of the color charge, cannot propagate through space unaccompanied: so they pull additional colored objects out of the vacuum until all the particles are assembled into neutral color groups. The scattered parton can be thought of as fragmenting into a shower of hadronic particles.

[2] L. Cormell and J. F. Owens, "High- p_T Production of Direct Photons and Jets in Quantum Chromodynamics", *Physical Review D*, Vol.22, No.7, pp.1609-1616, (1980).

the underlying kinematics involved. Furthermore, using three quark types, there are 127 two body scattering processes that contribute to single particle inclusive hadron production^[3], which makes it extremely difficult to disentangle gluon from quark effects. This is not the case with direct photon production. If the Compton and annihilation processes can be separated, they can provide direct information on the distributions of gluons within hadronic particles and the fragmentation properties of the gluon respectively. A large part of the interest in direct photons comes from this possibility of separating quark and gluon effects.

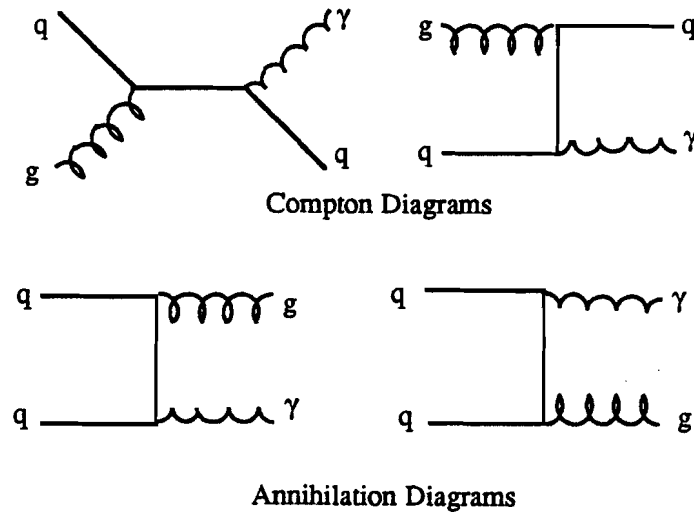


Figure 1: Feynman Diagrams of the Primary Direct Photon Processes

Interest in high p_T direct photon production also stems, in part, from the fact that its cross section is an instance where the QCD prediction is thought to be reliable. QCD predictions are based on perturbative expansions and are only valid when the value of the strong coupling

^[3] J. F. Owens, "Large-Momentum-Transfer Production of Direct Photons, Jets and Particles", *Reviews of Modern Physics*, Vol.59, No.2, pp.465-503, (1987).

constant α_s is small. Now α_s is dependent on the amount of momentum transferred (Q^2) in the scattering according to the relation:

$$\alpha_s(Q^2) = \frac{12\pi}{(33 - 2f)\ln(Q^2/\Lambda^2)}, \quad (1)$$

where f is the number of quark flavors and Λ is a parameter that sets the scale for Q^2 . From Eq.1 it follows that $\alpha_s(Q^2)$ approaches 0 as Q^2 approaches ∞ which implies that a condition known as "asymptotic freedom" exists and that perturbative QCD predictions are possible at large Q^2 ^[4]. Thus examining direct photon production in the region where the scattering angle is in the vicinity of 90° in the center of momentum frame of reference, which is equivalent to high p_T scattering for collisions with large \sqrt{s} , ensures that the reactions have a large Q^2 and that perturbative QCD calculations are plausible.

The Lorentz invariant cross section for direct photon production is:

$$E_\gamma \frac{d^3\sigma}{d^3p_\gamma}(A + B \rightarrow \gamma + X) = \sum_{a,b} \int dx_a dx_b G_{a/A}(x_a, Q^2) G_{b/B}(x_b, Q^2) E_\gamma \frac{d^3\hat{\sigma}}{d^3p_\gamma} \quad (2)$$

where,

$$E_\gamma \frac{d^3\hat{\sigma}}{d^3p_\gamma} = \frac{\hat{s}}{\pi} \frac{d\sigma}{dt}(a + b \rightarrow \gamma + d) \delta(\hat{s} + \hat{t} + \hat{u}) \quad (3)$$

is the elementary parton scattering cross section with $\hat{s}, \hat{t}, \hat{u}$ as the parton Mandelstam variables and $G_{a/A}(x_a, Q^2)$ is the structure function of parton a in hadron A .

At low p_T the Compton term of the direct photon cross section dominates in the reactions $\pi^\pm + p/n \rightarrow \gamma + X$. But as p_T rises the annihilation term begins to dominate because presumably the gluon momentum distributions decrease faster with increasing x than do the valence quark distributions. Here x is taken to be the fraction of the hadron's momentum that a parton carries. Furthermore, significant differences between the cross sections $\sigma(\pi^+ + n/p \rightarrow \gamma + X)$

^[4] David J. Gross and Frank Wilczek, "Asymptotically Free Gauge Theories", *Physical Review D*, Vol. 8, No. 10, p. 3633, (1973).

and $\sigma(\pi^- + n/p \rightarrow \gamma + X)$ arise from the differences in the valence quark content of the pions. The contribution of the Compton diagram in each reaction is the same so the difference in the cross sections must come from the annihilation term. Now the π^+ has an $u\bar{d}$ valence quark pair and the π^- has an $\bar{u}d$ valence quark pair. By counting the valence quarks of the pions and nucleons one finds that the charge factor in the annihilation term of the cross section favors the $(\pi^-, p/n)$ reactions by a factor of four because of the difference in the charge magnitude of the u and d quarks. In principle this should allow the separation of the two production mechanisms.

From the measured cross sections for $\pi^\pm + p/n \rightarrow \gamma + \text{jet} + X$ one can use differences in the π^\pm data to extract several interesting quantities. In the Compton term the away side jet is a fragmenting quark. Analysis of the charge distributions in these jets should yield a net positive charge bias due to the difference in magnitudes of the u and d quark charges^[5]. With sufficient constraints on particle identification and interaction kinematics one could also in principle obtain the fragmentation functions $D_{h/g}(z_h, Q^2)$ where z_h is the fraction of the scattered quark momentum carried away by hadron h . Likewise, the excess caused by the annihilation term consists of events in which the jet associated with the direct photon is produced by a fragmenting gluon (See Fig.1) offering the possibility of extracting the gluon fragmentation functions $D_{h/g}(z_h, Q^2)$ ^[6].

Examination of this data might also allow the determination of the gluon structure functions $G_{g/\pi, p}(x_g, Q^2)$. If the quark structure functions $G_{q_i/\pi}(x_{q_i}, Q^2)$ and $G_{q_i/p}(x_{q_i}, Q^2)$ are taken as input, then the measured difference in the two cross sections can be used to determine the gluon structure functions^[7]. Determination of $G_{g/\pi, p}(x_g, Q^2)$ is important because presently there is no theoretical basis for *a priori* predicting their shape. The distribution functions are parametrized from experimental data using parton counting rules and QCD Q^2 evolution

[5] F. Halsen, M. Dechantsreiter, and D. M. Scott, "Structure of Direct-Photon Events", *Physical Review D*, Vol. 22, No. 7, (1980).

[6] A. P. Contogouris, S. Papadopoulos, and C. Papavassiliou, "Large- p_T Direct Photon and Opposite-Side Photon-Hadron Correlations in QCD", *Nuclear Physics*, Vol. B179, pp. 461-476, (1981).

[7] L. Cormell, op. cit., pp. 1613-1615.

requirements to constrain the fits^[8]. While the quark/gluon distribution functions have been extracted from deep inelastic lepton/hadron scattering, high mass dilepton (Drell-Yan), and hadronic J/Ψ production data, only the quark distributions are well determined. The gluon distribution functions are not as well known. For deep inelastic scattering, the distributions can be constrained to some extent by how they influence the Q^2 evolution of the quark distributions. However, the gluon distributions depend sensitively on the value chosen for the QCD scale parameter Λ so that care must be taken in choosing Λ when fitting the distributions to obtain consistent results. For the massive dilepton data, there is a large amount of uncertainty due to nuclear effects. Since the gluon has no electric charge, the coupling occurs only in the next to leading logarithm terms of a QCD expansion for these data sets. While the J/Ψ data constrain the gluon distributions directly by virtue of its production through the process $gg \rightarrow J/\Psi$, there is some concern over the fact that the J/Ψ data was fitted using a “duality” type model. All of this has prompted the creation of a set of distribution functions but a lack of certainty about their final form still exists^[9].

I.2 Direct Diphoton Production

Two body parton scattering can also produce two direct photons with no accompanying hadron jets. There are two basic subprocesses for direct diphoton production, $q\bar{q}$ and gg annihilation (See Fig.2). While the expected signal for this should be considerably lower than the single direct photon signal there are several items of interest that could be extracted from a measurement of the production cross sections.

For a collinear parton pair annihilating into two photons, the measured p_T of the resulting γ 's should exactly cancel so that any p_T imbalance is a measurement of the intrinsic energy “ k_t ”

[8] G. Altarelli and G. Parisi, “Asymptotic Freedom in Parton Language”, *Nuclear Physics*, Vol.B126, pp.298-318, (1977).

[9] D.W.Duke and J.F.Owens, “ Q^2 -Dependent Parameterizations of Parton Distribution Functions”, *Physical Review D*, Vol.30, No.1, pp.49-45, (1984).

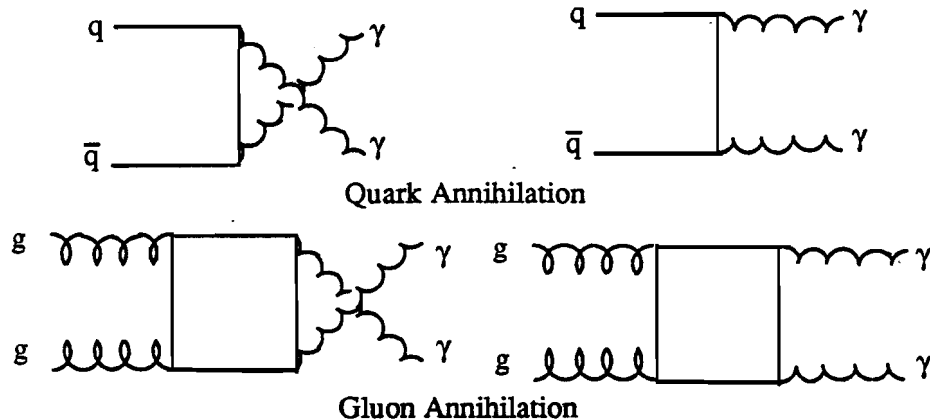


Figure 2: Feynman Diagrams of the Primary Direct Diphoton Processes

of the colliding hadrons constituent partons. This is true in general for two body scattering but the fragmentation of the scattered partons obscures the underlying kinematics because of the uncertainty associated with reconstructing hadronic jets. With direct diphoton production the scattering kinematics is precisely determined^[10].

Because $d\hat{\sigma}/dt(q\bar{q} \rightarrow \gamma\gamma)$ is proportional to the fourth power of the quark charge the ratio;

$$\frac{d\hat{\sigma}(q\bar{q} \rightarrow \gamma\gamma)}{d\hat{\sigma}(q\bar{q} \rightarrow \gamma g)} = \frac{3}{4} \frac{\alpha}{\alpha_s} e_q^2 \quad (4)$$

provides a way to determine the quark charges e_q ^[11]. One might find the *u* quark charge using the reaction $\pi^- + p \rightarrow \gamma\gamma + X$, and $\pi^+ + p \rightarrow \gamma\gamma + X$ might yield the *d* quark charge. This ratio also provides a check on the strength of the strong coupling α_s .

The items of interest from $q\bar{q}$ annihilation must be extracted from a background that includes contributions from gg annihilation. If the contributions from the two subprocesses can be extracted then by comparing the diphoton cross sections to that for the Drell-Yan process

[10] T. Ferbel and W. R. Molson, "Direct Photon Production in High-Energy Collisions", *Reviews of Modern Physics*, p. 181, (1984).

[11] E. L. Berger, E. Braaten, and R. D. Field, "Large- p_T Production of Single and Double Photons in Proton-Proton and Pion-Proton Collisions", *Nuclear Physics B*, Vol. 239, pp.52-92, (1984).

$AB \rightarrow l^+ l^- X$ (See Fig.3) there are a couple of things to be learned. One is that the contribution of $(gg \rightarrow \gamma\gamma)$ to the ratio:

$$\frac{d\sigma(AB \rightarrow \gamma\gamma X)}{d\sigma(AB \rightarrow l^+ l^- X)} \approx 2 \frac{e_u^4 u(x) + e_d^4 \bar{d}(x)}{e_u^2 u(x) + e_d^2 \bar{d}(x)} \quad (5)$$

which is very model dependent, would provide a check on the gluon structure functions $G_{g/\pi,p}(x_g, Q^2)$ while the $q\bar{q} \rightarrow \gamma\gamma$ process would provide a test of QCD. This is because the almost model independent $q\bar{q} \rightarrow \gamma\gamma$ process has the same higher order correction terms as Drell-Yan and any excess in the ratio of the two processes should be from $gg \rightarrow \gamma\gamma$ and not from corrections^[12]. A second thing to be learned is that equation 5 is directly dependent on the quark charges so that for (π^-, p) reactions one could again measure the u quark charge and for (π^+, p) the d quark charge^[13].

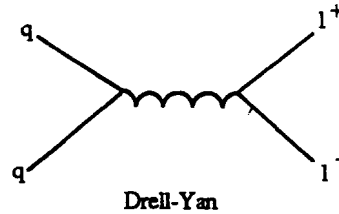


Figure 3: Feynman Diagram of the Drell-Yan Process

I.3 Higher Twist Production of Direct Photons

Possible contributions to the direct photon cross section come also from “higher twist” processes. Higher twist processes include many of the ideas from the older constituent interchange model (CIM) which attempted to account for the differences between the expected p_T^{-4}

[12] C. Carimalo, et.al, “Direct-Photon Pair Production in Hadron Collisions as a Check of QCD”, *Physics Letters*, Vol.98B, No.1,2, pp.105-109, (1981).

[13] M. Krawczyk and W. Ochs, “Direct and Indirect Production of Photon, Lepton, and Hadron Pairs in Hadron-Hadron Collisions”, *Physics Letters*, Vol.79B, No.1,2, pp.119-122, (1978).

dependence of many cross sections and the measured p_T^{-8} dependence. Scaling violations, with a p_T^{-6} dependence, could not account for the difference. The CIM model tried explaining the remaining discrepancy by invoking processes in which coherent scattering of quarks and gluons occurred. While higher twist type reactions are expected to dominate cross sections at low p_T , they make only small contributions near the edge of phase space for $p_T > 6 \text{ GeV}/c$ ^[14]. It is possible, however, that their presence might be detected; reactions such as $\pi q \rightarrow \gamma q$ have a distinctive signature in that there is no beam jet of consequence.

I.4 Physics Goals of E-706

It is apparent from the above discussion that the study of direct photon production can potentially lead to information on the substructure of hadronic matter that is not readily available from other types of experiments. From the diverse set of possible measurements E-706 has chosen several of them as goals, as listed below [15]:

- 1) The determination of the γ/π^0 production ratio as a test of QCD.
- 2) Determination of the gluon structure functions $G_{g/\pi,p}(x_g, Q^2)$ by the comparative analysis of data from $\pi^\pm + n/p \rightarrow \gamma + X$.
- 3) Determination of the gluon fragmentation functions $D_{C/g}(z_c, Q^2)$ by a similar analysis.
- 4) Study of $q\bar{q} \rightarrow \gamma\gamma$ production for comparison to Drell-Yan production $q\bar{q} \rightarrow l\bar{l}$ as a test of QCD.

The study of these reactions is a critical test of QCD predictions and will provide phenomenological information on the gluon content of hadronic particles.

[14] J.F. Owens, op.cit., pp.474-476.

[15] Paul Slattery, et.al., "A Proposal to Measure Direct Photon Production at Tevatron Energies", FNAL document P695/P706, pp.3-8, (1981).

I.5 Production Rates and Background for Single Photon Production

High p_T direct single photon production is suppressed relative to hadron jet production by a factor of α/α_s . This is reasonable, since the subprocesses involved are similar except that a gluon is replaced by a photon. Because the jet/hadron production ratio is of the order of $10^2 \rightarrow 10^3$, a ratio such as γ/π^0 maybe of the order of 1. This arises primarily because photons, which arise directly from the interaction, carry away the full p_T of the interaction. Scattered partons, on the other hand, must fragment into several hadronic particles which reduces the transverse momentum any one of the fragments can have^[16]. Even though it appears that direct photon production competes favorably with a process such as π^0 production, there are still several sources of background that must be dealt with to extract the signal.

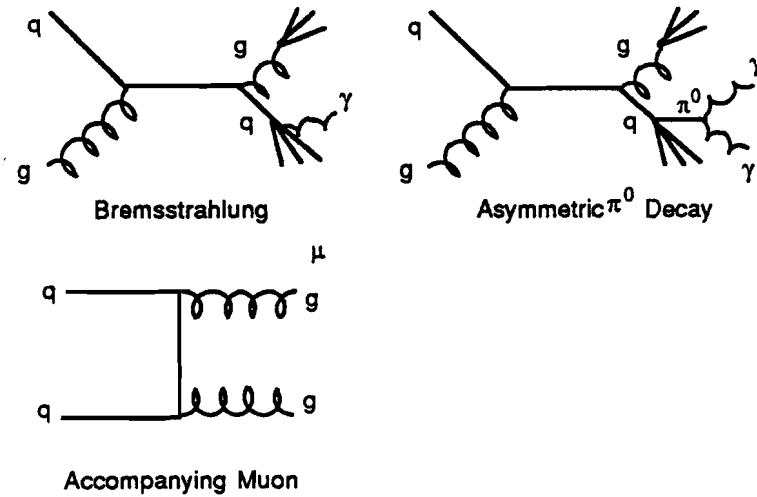


Figure 4: Background Processes which mimic Direct Photons

[16] J.F. Owens, op.cit., p.466.

I.5.1 Bremsstrahlung

Bremsstrahlung production of γ 's by fragmenting parton jets is a considerable source of background to direct photon production. The reason for this can be seen from the following argument. The lowest order direct photon processes are proportional to $\alpha\alpha_s$, and two body parton scattering is proportional to α_s^2 . Given that the photon fragmentation functions $D_{\gamma/g,q}(z_\gamma, Q^2)$ are proportional to α/α_s , then bremsstrahlung production is of the same order as direct photon production, ie. $\alpha\alpha_s$,^[17]. Next to leading log calculations have predicted that $q\bar{q} \rightarrow q\bar{q}\gamma$ is 30-40% of the value of the Compton process $qg \rightarrow q\gamma$ for $p_T \approx 13\text{GeV}/c$ for $\sqrt{s} = 63\text{GeV}$ and $\Theta_{CM} = 90^\circ$ ^[18]. A large part of this background should be eliminated by special cuts which isolate the photon from accompanying hadrons and by kinematic cuts on the momentum balance of the event. This is important for photon-jet correlation studies since the inclusion of the bremsstrahlung component can drastically affect the results^[19]. It should be noted that a correlation study of γ 's with same side hadrons could determine the form of the fragmentation function $D_{\gamma/g}(z_\gamma, Q^2)$ ^[20].

I.5.2 Decays of Neutral Particles

Another source of background to direct photon events are the decays of neutral particles, such as a π^0 or an η , into two photons. In highly asymmetric decays the low energy photon is often lost and only the high energy photon is detected. For very high energy π^0 's that decay symmetrically the two photons tend merge into a single shower. Both cases allow the π^0 to masquerade as a direct photon. A large number of these events should be discovered by making isolation cuts since the π^0 comes from a fragmenting parton jet. A word of caution is

[17] J. F. Owens, op.cit., p.474.

[18] M. Nowak and M. Praszalowicz, "Direct Photon Production Beyond Leading Log Approximation - $q + q \rightarrow \gamma + q + q$ Contribution", *Zeitschrift fur Physik C Particles and Fields*, Vol.17, pp.249-257, (1983).

[19] R. Baier, J. Engels, and B. Peterson, "Correlation with Large Transverse Momentum Photons and Gluon Structure Functions", *Zeitschrift fur Physik C Particles and Fields*, Vol. 6, pp. 309-316, (1980).

[20] M. Dechantsreiter, op.cit., pp. 2859-2860.

appropriate at this point because π^0 's may not be easily isolated at high p_T . If the π^0 carries most of the momentum, then the rest of the jet has relatively little momentum and may go undetected. Therefore, it is necessary to carefully measure the π^0 production cross section so that its contribution to the direct photon production background can be subtracted. This necessitates a fine spatial resolution for the calorimetry to resolve the very high energy π^0 's.

1.5.3 Muon Beam Halo

Another large source of background for direct photon physics are the events in which the trigger is satisfied by the passage of a muon from the halo which accompanies the beam. Because the pion beam is produced by the interaction of a primary proton beam on a production target there is a large number of unwanted muons also produced. A certain number of these muons will accompany the beam as a diffuse extended halo, despite spoilers installed in the beamline to strip them away. Muons from this halo can interact via bremsstrahlung in the outer region of the calorimeter depositing energy which mimics a high p_T direct photon event. While many of the remaining muons can be tagged with the use of a veto wall, some of them will get through undetected.

There are several means available to eliminate these unwanted events from the data. Very often a false event can be produced by a muon that is not in time with the interaction it causes the trigger to save. By providing timing information of the energy deposited in the calorimeter a large number of these events can be eliminated during data analysis. Another means of cutting out these events is through a directionality cut. Since the triggering muon does not come from the interaction vertex, information on the direction of the particles is an efficient way of disposing of false events. This makes it important for the calorimetry to have more than one longitudinal section so that the direction of the showers can be determined from the separate position measurements in each section. A final method for eliminating false events is by the analysis of the shower shapes produced by particles in the calorimeter. Muons are highly

penetrating and tend to deposit significant energy only when they undergo bremsstrahlung, which can happen anywhere in a calorimeter. Photons, on the other hand, shower rapidly upon interacting with matter. Analysis of the longitudinal development of energy deposition in the calorimeter should provide a useful way of cutting false direct photon events from the data sample.

I.6 Production Rates and Background for Diphoton Production

It is expected that the diphoton production rate is of the same order of magnitude as that for the Drell-Yan process. The ratio of the two cross sections should be bound by the following limits^[21]:

$$\frac{2}{3} < \frac{d\sigma(q\bar{q} \rightarrow \gamma\gamma)}{d\sigma(\text{Drell-Yan})} < \frac{8}{9}, \quad (6)$$

for (π^-, p) reactions. Also, by naively taking the ratio^[22]:

$$\frac{d\hat{\sigma}(q\bar{q} \rightarrow \gamma\gamma)}{d\hat{\sigma}(q\bar{q} \rightarrow \gamma g)} = \frac{3}{4} \left(\frac{\alpha}{\alpha_s} \right) e_q^2, \quad (7)$$

it can be seen that diphoton production should be roughly 1% of that for single direct photons.

The background sources for direct diphoton production are basically the same as those involved in single photon production. In this case it can be any combination of two of the following processes bremsstrahlung photon, asymmetric neutral decay, halo muon, or a single direct photon. The rate for $gq \rightarrow \gamma(q \rightarrow q\gamma)$ has been estimated at about 35% of the rate for the two principal production processes^[23]. Here again, isolation cuts and kinematic requirements should help clean up the event sample.

[21] C. Carimalo, op.cit., p.106.

[22] E.L. Berger, op.cit., p.79.

[23] E.L. Berger, ibid., p.88.

A great deal of work has been done in the area of direct photons and there are several excellent reviews of this work^{[24][25]}. There still remain a number of unanswered questions, however, and E-706 should make a substantial impact on the field with a spectrometer designed specifically for direct photon physics.

[24] J. F. Owens, *op. cit.*

[25] T. Ferbel and R. Molzon, *op. cit.*

Chapter II

Description of E-706 Experimental Setup

To study the physics involved in direct photon production a new particle spectrometer has been built at the Fermi National Accelerator Laboratory(FNAL). Located in the new Meson West (MW) beamline the spectrometer consist of several new instruments, each of which was assembled by a different member of the E-706 collaboration. Each of these instruments was designed to handle the high interaction rates necessary to produce sufficient data from which to extract direct photon physics. Each detector was also designed to subtend as much of the center of mass solid angle of the interactions as possible so that acceptance losses could be minimized. The major spectrometer components and the institutions responsible for them are listed below. This chapter contains a brief description of the beam line and each of the pieces of the spectrometer.

Cerenkov beam counter (CC)	FNAL
Silicon strip detector (SSD)	University of Pittsburgh
Momentum Analysis magnet	FNAL
Proportional wire chambers (PWC)	Michigan State University Penn State University
Electromagnetic liquid argon calorimeter (EMLAC)	University of Rochester
Hadronic liquid argon calorimeter (HALAC)	Northeastern University FNAL University of Rochester
Forward calorimeter (FCAL)	University of Minnesota

Table 1: List of Spectrometer Detectors

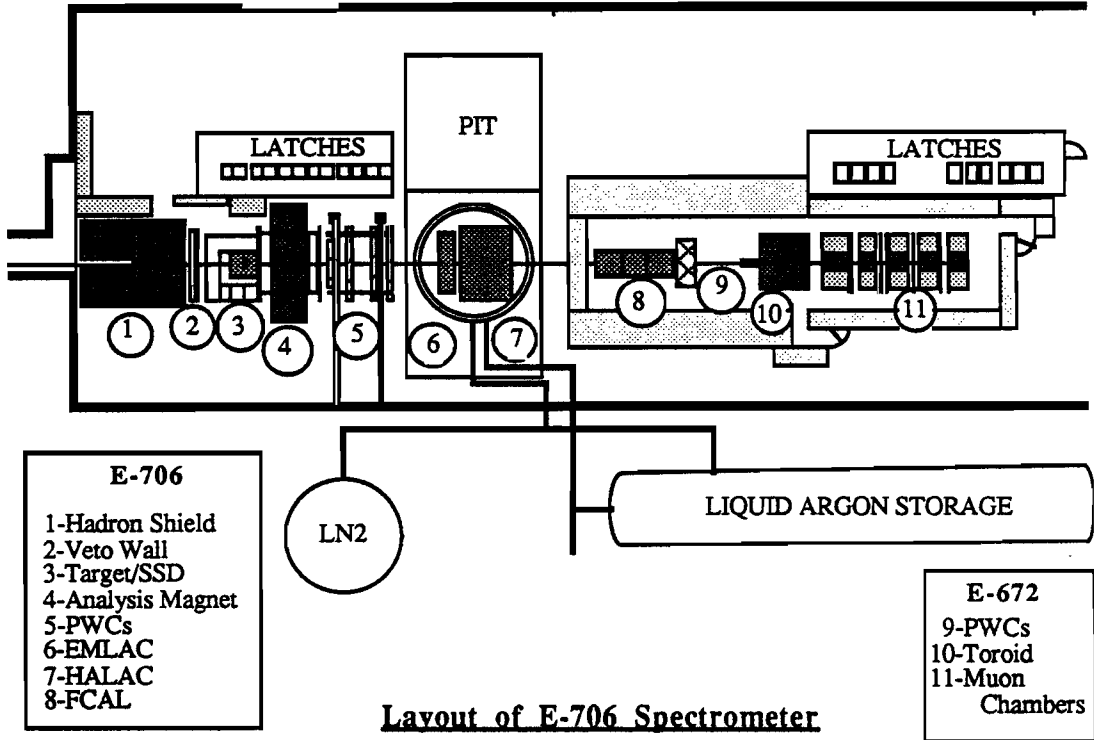


Figure 5: Detector Layout of the E-706 Spectrometer

II.1 The M-West Beamline

The primary beamline used for E-706 has a 800 GeV/c primary proton beam with a maximum intensity of 2×10^{12} protons per spill. The beam has a 19.9 ns bucket structure and spills were 23 s long, separated by 40 s. This beam is used to generate a 530 GeV/c secondary beam from a one interaction length aluminum target. The secondary beam can be selected to be either positively or negatively charged. The secondary beam momentum of 530 GeV/c was selected so that the momentum content of the pion quark constituents would be approximately the same as that for the quark constituents of the 800 GeV/c primary proton beam. The comparison of pion and proton data is facilitated when the constituent partons have approximately the same momentum. A secondary beam intensity of 3×10^7 pions per spill produces an interaction rate

of the order of 1×10^6 interactions per second^[1]. The bucket occupancy rate for the secondary beam was approximately 4%, of these 2% were doubly occupied. The momentum spread of the beam is typically less than 6% (See Fig.6).

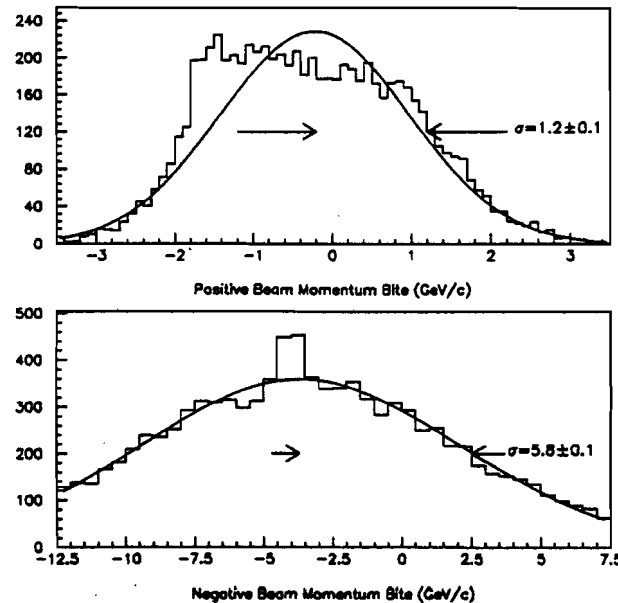


Figure 6: Distributions of $\delta p/p$ for MW Beamline Positive and Negative Beams

Particle	Flux
p	1×10^8
π^+	1×10^7
K^+	2×10^6
\bar{p}	4×10^4
π^-	2×10^7
K^-	4×10^5

Table 2: Nominal MW Particle Production at 530 GeV/c per 1×10^{12} Interacting 800 GeV/c Protons

[1] G. Ginther, *Private Communication*.

The beamline contains three spoilers to deflect the muon halo away from the beamline. Stray muons which travel parallel to the beamline are a principal part of the trigger background for this experiment (See Chapter I). Muon contamination in the beam was measured to be 0.4% for positive beam and 0.5% for negative beam. At the end of the beamline there is a hadron shield, 4.3 m wide, 4.7 m long, and 3.7 m high, made from scrap battleship armour plate. It has a 10 cm wide vertical slot along the beamline. The two iron slabs that fill the slot are removable by overhead crane for calibration so that the beam can be scanned in the vertical direction. The beam pipe extends through the slot in the hadron shield and terminates in a 76 μm thick titanium window

II.1.1 The Cerenkov Beam Counter

E-706 uses a differential Cerenkov counter to discriminate pions, kaons and protons in the secondary beam. A Cerenkov counter works on the principle that charged particles traveling through some medium faster than the speed of light in that medium give up some of their energy in the form of electromagnetic radiation. This radiation is emitted at a specific angle relative to the direction of motion of the particle. For particles of different masses at the same momentum the radiation is emitted at different angles according to the relation;

$$\theta_c = \cos^{-1}\left(\frac{1}{\beta n}\right), \quad (8)$$

where $\beta = v/c$ and n is the index of refraction of the medium.

The Cerenkov counter is 42.1 m long and has a radius of 24.4 cm. It uses helium gas, in a range of 4-7 psia, as its radiator. It has a 32.4 m focal length mirror which focuses light at two rings of scintillator. The rings are 10.3 cm and 19.2 cm in radius and each is equipped with 6 phototubes. The inner ring is used in coincidence and the outer ring in anticoincidence with two scintillation counters. The counters are 10 \times 10 cm and are placed at the upstream and downstream ends of the detector. By adjusting the pressure of the helium gas the index of

refraction changes allowing the light emitted by pions or protons or kaons to be focused on the coincidence ring.

The Cerenkov detector was usually set to trigger on the minority beam particle. It had an efficiency of 57% for tagging the K^- in the negative beam with less than 5% contamination by π^- . The efficiency for tagging π^+ in the positive beam was 80-85% with less than 8% contamination by K^+ and negligible contamination by protons^[2].

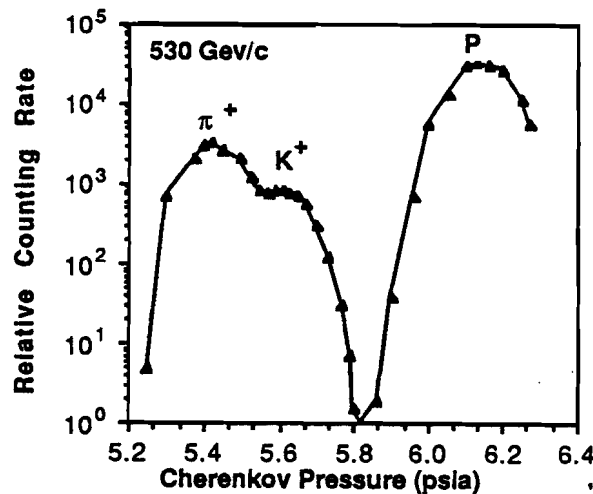


Figure 7: Plot of Cerenkov Pressure Curve for Positive Beam

II.1.2 The Calibration Magnet

The MW beamline contains a dipole magnet that can deflect the beam vertically. This magnet is used during the calibration of the spectrometer and is normally off during data

^[2] I. Kourbanis, *Private Communication*.

acquisition. It is 3 m long with an aperture of 7.6×15.2 cm. The magnet is 54.7 m from the target. The magnetic field (B) can be estimated from the following equation

$$B(KG) = 0.0166 \times I(\text{amps}) + 0.019 \quad (9)$$

The final quadrupole section of the beamline, which is downstream of the calibration magnet, can be pushed out of the way during calibration.

II.1.3 The Interaction and Trigger Counters

There were several counters used in the trigger to define an interaction. These are made of acrylic scintillator with phototubes attached. The signals from these counters are sent to discriminator modules whose outputs are saved in a set of electronic latches. When a trigger occurs, the data is then read by a computer from the latches.

The beam is defined by three scintillation counters which make up the beam hodoscope. Two of them, BA and BB, are $2.5 \times 2.5 \times 0.15$ cm and the third, BH, is $12.7 \times 12.7 \times 0.7$ cm and has a 1 cm hole. Together they logically define a beam particle (BM) as $BM \equiv BA \wedge BB$. The beam counters are positioned just downstream of the hadron shield (See Fig.8).

An interaction can be signaled by any one of four scintillation counters; SE1, SW1, SE2, and SW2. SE1 and SW1 are 7.6×15.2 cm and are positioned just upstream of the analysis magnet. SE2 and SW2 are 10.2×20.4 cm and are positioned just downstream of the magnet. Both sets of scintillators mate to form a 2 cm hole around the beamline. These four counters define an interaction as $INT \equiv BM \wedge (SE1 \vee SW1 \vee SE2 \vee SW2)$. This interaction definition was fed to a logic unit which kept a history of the number of interactions for a time interval equivalent ± 3 beam buckets. The final interaction definition is then defined as $LINT1 = BM \wedge \overline{BH} \wedge CLEAN \wedge CR$. Here CLEAN is defined as no interactions within ± 3 beam buckets and CR is a computer ready

signal. The number of beam particles and interactions are tallied in electronic counters for use in the normalization of production cross sections^[3].

The veto wall (VW) is made of two layers of four 213×160 cm modules arranged in an overlapping manner so that there is a 10×10 cm hole on the beamline. Each module contains eight scintillation counters. The two layers of the veto wall are in coincidence so that events that have muons in the same region as the trigger from the EMLAC can possibly be vetoed by the trigger (See Chapter III.2.3).

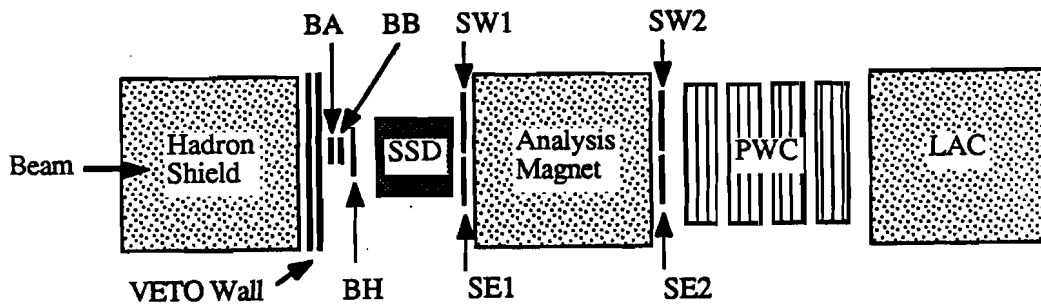


Figure 8: Plane View of Trigger System Counters

II.2 Description of E-706 Tracking System

To understand the structure of an event the momentum and direction of all the particles coming from an interaction must be determined. For charged particles the reconstruction of the tracks both before and after the magnet can determine the momentum of the particles. The field of a magnet causes a bend in the the track of a charged particle. For a field of constant strength the amount of this bend is inversely proportional to the momentum of the particle. Therefore, the angle measured between the upstream and downstream tracks is a measure of the particle's momentum (P). The tracking system for E-706 consists of a silicon strip detectors for upstream

^[3] C. Yosef, "Production of High Transverse Momentum Neutral Pions in Hadronic Collisions", *North-eastern University Ph.D. Thesis* in preparation.

tracking, an analyzing magnet, and a set of proportional wire chambers for downstream tracking. The momentum resolution ($\Delta P/P$) of the system was determined from a Monte Carlo calculation to be^[4],

$$\frac{\Delta P}{P} = 0.09P\%, P \text{ in } \text{GeV}/c. \quad (10)$$

II.2.1 The Silicon Strip Detector

The purpose of the silicon strip detectors (SSD) is to provide information for the reconstruction of upstream tracks and vertices of charged particles. The design of the upstream tracking system had to take several things into account. It had to be compact along the beam axis so that the LAC acceptance could be maximized. The angular resolution had to be such that ambiguities in the track reconstruction of the PWCs could be resolved and so one could determine which particles are a result of secondary interactions^[5].

There are 14 SSDs. Each SSD is a silicon wafer that contains sense lines for measuring the position of the particles in one dimension. The wafers come in orthogonal pairs of X and Y planes. Four of these pairs are 3x3 cm and the last three pairs are 5 x 5 cm. All of the wafers have a thickness of 250-300 μm and a 50 μm pitch between sense lines. The angular resolution of the SSDs has been estimated to be 0.08 mr. There are a total of 8800 channels for the SSD system of which 6600 are instrumented. The wafers are mounted to a series of three signal fanout boards. These boards increase the spacing between the strips so that on the outermost board preamplifiers and communication cables can be attached to each channel.

Three pairs of the SSDs are positioned upstream of the target to provide tracking of the beam particle. The other pairs are positioned downstream of the target to track the particles coming from the interaction. The target is a set of 20 plates spaced 1.6mm apart. Each plate

[4] K. Hartman, *Private Communication*.

[5] S. Mani, et al., *E-706 Internal Note 125*.

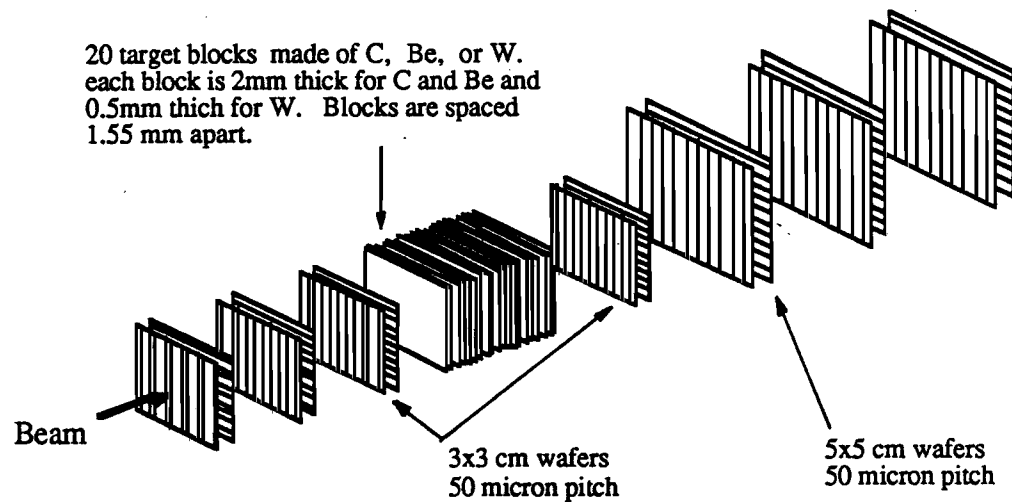


Figure 9: Layout of Silicon Strip Detector and Target

is 2×10 cm in area and 1/200 of an interaction length thick. The materials used for the target are Be, C, or Cu.

II.2.2 The Analysis Magnet

The momentum analyzing magnet is a vertical dipole with a maximum field of 15.2 KG, centered 2 m downstream of the target. The magnet current was adjusted to generate a 450 MeV/c kick to charged particles passing through its aperture. The magnet aperture expands from 35.6×25.4 cm to 137.2×124.5 cm over a length of 3.9 m. The magnet has upstream and downstream mirror plates, to reduce the fringe field outside the volume of the magnet so that the charged particles would travel linearly through the SSDs and PWCs.

II.2.3 The Multi-Wire Proportional Chambers

There are 16 planes of multi-wire proportional chambers with a rate capability in excess of 1 MHz. The 16 planes are constructed in 4 modules. Each of these modules contains 4 planes with wires in the X, Y, U(+37°), and V(-53°) orientation. The spacing between the chambers

is much larger than the spacing between the SSDs (See Table 3). So, the spacing between the sense wires can be larger and still maintain approximately the same angular resolution. The sense wires of each plane have a pitch of 0.25 cm and the angular resolution of the chambers has been estimated using Monte Carlo methods to be 0.3 mr. The cathodes are constructed of graphite coated mylar. The graphite coating is segmented into pads so that regions near the beam can be selectively adjusted to lower voltages. This prevents the channels near the beam from being overloaded by too many hits [6].

The electronics for both the SSDs and the PWCs is identical except for the preamplifiers used with the SSDs. The signals are all processed in a Nanometric electronic system produced by Nunamaker Electronics. The front end of the system is a N-277C amplifier board that contains a wide band video amplifier followed by a threshold discriminator and an ECL line driver. The data from the discriminators is saved by N-278 latches controlled by an N-280 controller. All of these modules are housed in CAMAC crates. When a trigger is issued, the data from the latches is transmitted by the controllers to a PDP-11/34. [7]

Module	Aperture	Pitch	Z Position
SSD 1	$3.0 \times 3.0 \text{ cm}^2$	$50 \mu\text{m}$	-128.5 cm
SSD 2	$3.0 \times 3.0 \text{ cm}^2$	$50 \mu\text{m}$	-32.5 cm
SSD 3	$3.0 \times 3.0 \text{ cm}^2$	$50 \mu\text{m}$	-15.0 cm
SSD 4	$3.0 \times 3.0 \text{ cm}^2$	$50 \mu\text{m}$	-2.0 cm
SSD 5	$5.0 \times 5.0 \text{ cm}^2$	$50 \mu\text{m}$	3.5 cm
SSD 6	$5.0 \times 5.0 \text{ cm}^2$	$50 \mu\text{m}$	9.0 cm
SSD 7	$5.0 \times 5.0 \text{ cm}^2$	$50 \mu\text{m}$	14.5 cm
PWC 1	$1.22 \times 1.63 \text{ m}^2$	2.5 mm	382.0 cm
PWC 2	$2.03 \times 2.03 \text{ m}^2$	2.5 mm	476.0 cm
PWC 3	$2.03 \times 2.03 \text{ m}^2$	2.5 mm	570.0 cm
PWC 4	$2.44 \times 2.44 \text{ m}^2$	2.5 mm	661.0 cm

Table 3: Tracking System Parameters

[6] Carl Bromberg, *E-706 Internal Note 94*.

[7] S. Mani, op. cit., p.11.

II.3 Calorimetry

The E-706 spectrometer has three calorimeters. It has two calorimeters, collectively referred to as "LAC", which are sampling calorimeters that use liquid argon for the active medium and use lead and steel for their energy absorbers respectively. The forward calorimeter is a steel and plastic scintillator sampling calorimeter. The LAC subtends approximately 50% of the event center of mass solid angle and is used to measure the energy of the scattered partons (See Chapter III). The forward calorimeter is used to measure the energy of the unscattered beam partons which fragment in a narrow forward cone and are missed by the LAC.

II.3.1 The LAC

The LAC is the heart of the spectrometer since its design was optimized to measure the electromagnetic energy of particles coming from an interaction. This is very important for doing direct photon physics. For the moment a brief description of the LAC is sufficient. A full description of the LAC will follow in the subsequent chapters.

The LAC is suspended from a steel I-beam frame called the "gantry". The gantry can be moved transverse to the direction of the beam. This allows all the detector channels to be exposed to the beam for calibration by using the calibration magnet to provide vertical motion of the beam. The dewar, which contains the liquid argon for the LAC, attaches to the top of the gantry. As mentioned above the LAC is actually two calorimeters. One is used to measure the amount of electromagnetic energy in each event and the other is used to measure the amount of hadronic energy in each event. They are referred to as the EMLAC and the HALAC respectively. Both calorimeters hang in the dewar from the gantry and each has a 20 cm radius hole that allows beam particles that do not interact to pass through. This hole is present because a liquid argon calorimeter can only take data at a maximum rate of 1 MHz. Since the beam rate was approximately 10 MHz the central region of the LAC would have been dead and unable to measure the energy in the forward scattering region.

The EMLAC is the true heart of E-706. Its purpose is to detect and measure the energy of all electromagnetic type particles, ie. photons, electrons, positrons. It is 26 radiation lengths thick, 2 interaction lengths thick and the first sampling cell is positioned 9 m from the target. It was designed to have a high level of discrimination between electromagnetic and hadronic showers. The EMLAC has a strip type readout using an r, ϕ rather than X, Y system. The strip width was optimized to distinguish between photon and π^0 charge showers.

The purpose of the HALAC is to measure the energy of the high momentum hadrons which penetrate through the EMLAC. In particular, the energy measurement of neutral hadrons is important for the determination of fragmentation functions. This is one of the main goals of the experiment (see Chapter I). The HALAC is 7.8 interaction lengths thick and has a triangular pad type readout. The pad size was chosen so that the shower from a single hadron is contained in a hexagon of six pads.

II.3.2 The Forward Calorimeter

Since the LAC has a hole along the beamline, a significant percentage of energy from any given interaction can escape detection. Most of this energy is contained in the fragmentation of the beam jet partons of the beam particle and to a lesser extent the stragglers from the breakup of the target nucleus. To measure this escaping energy, the forward calorimeter was constructed downstream from the LAC.

The forward calorimeter is a sampling calorimeter constructed of 1.9 cm thick steel absorber plates and 4.6 mm thick plexipopTM sheets^[8]. It is 114 cm in diameter so that it laterally contains any hadronic shower that escapes down the edge of the LAC hole. It has 3 modules that each contain 28 steel plates, spaced 6.3 mm apart, and 29 interleaved scintillator sheets each for a detector total of 9.5 interaction lengths. Into both the steel plates and the scintillator sheets a set of 76 holes have been drilled on a 11.5 cm grid. Inserted into these holes are 1.0 cm diameter

[8] Plexipop is an acrylic scintillator.

wave shifter rods which have phototubes attached at one end. The wave shifter rods are made from acrylic and are doped with an organic dye (BBQ) that shifts the blue light created by the passage of charged particles through the scintillator sheets to green light which can be detected by the phototubes. These rods have also been doped to absorb UV light produced by particles that might pass down the BBQ bars creating an anomalous signal^[9].

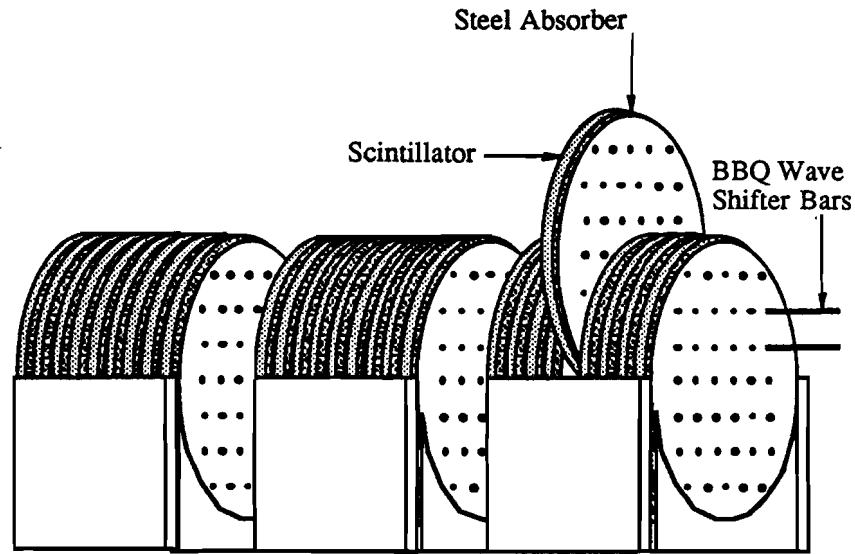


Figure 10: Isometric Drawing of the Forward Calorimeter

The signal from each wave shifter is digitized by a Siemens 5200S 6-bit flash encoder chip. The output of the ADC is clocked to a 256×4 bit memory at 100 MHz. The reference voltage supplied to the ADCs is not a constant but obeys the following relation;

$$V_{ref} = V_0 + A \times V_{input} \quad (11)$$

This gives the ADC a dynamic range of 8 bits, for $A=3/4$, but one pays a price in resolution for pulses that are near the top of the range. When the experimental trigger is received, a $2.56\mu s$ long time history of each phototube output can be read out by the data acquisition system.

^[9] P. Lukens and K. Ruddick, *E-706 Internal Note 141*.

The energy resolution of the forward calorimeter was parametrized using Monte Carlo methods and the energy scale was fixed using data from a 530 GeV/c pion beam. The detector was found to be dominated by systematics and has an energy resolution of $161\%/\sqrt{E}$ independent of energy. The position resolution for single particle showers was found to be 0.75 cm. Multi particle showers can only estimate the centroid of the deposited energy because of the geometry of the detector^[10].

[10] R. S. Benson, "Characteristics of Forward Energy Production in Proton-Nucleus and Pion-Nucleus Collisions at $\sqrt{S} = 31.5$ GeV", *University of Minnesota Thesis* 1989.

Chapter III

Design Criteria for the Liquid Argon Calorimeter

With this chapter the formal discussion of the LAC begins. In order to put the results presented later into proper perspective, it is necessary to understand the design limitations of the LAC. It is the purpose of this chapter to outline those limitations. As stated in the previous chapter the LAC is actually two separate calorimeters. The purpose of the EMLAC is to measure the energy of high p_T photons with resolution sufficient to determine if they are the result of a π^0 or η decay. The HALAC was built to measure the energy of the hadrons that either accompany or recoil against the photon. In designing the calorimeters there were seven criteria which controlled the process for selecting the appropriate calorimetry technology. They are^[1]:

1. The calorimeters should have as large an acceptance as possible.
2. The segmentation of the EMLAC lateral to the direction of the beam should be sufficiently fine that photons resulting from π^0 and η decays can be resolved adequately. This is essential in reducing the background to the direct photon signal.
3. The lateral segmentation of the EMLAC should be such that a trigger based on the electromagnetic p_T content of each event can be easily formed so that they can be selected and stored for analysis.
4. The energy resolution and linearity should be such that π^0 's and η 's can be reliably reconstructed and the event kinematics can be tightly constrained.
5. The large number of detector channels required by item 2 demands that their outputs over time should be stable due to the impracticality of performing frequent calibrations.
6. The calorimeters should have the ability to distinguish between photons and neutral hadrons.
7. The calorimeters have to be able handle interaction rates on the order of 1-2 MHz.

^[1] F. Lobkowicz, "Superiad", *E-706 Internal Note 002*, (1981).

The rest of this chapter starts by providing some of the reasons for using a liquid argon calorimeter. This is followed in turn by discussions of how each of the design requirements affects the structure of the calorimeter.

III.1 Choice of Calorimeter Type

A calorimeter is a block of matter which causes a primary particle to shower into a collection of less energetic particles. These less energetic particles then produce a signal within the calorimeter which indicates the presence of a particle shower. Most of the energy for a shower is dissipated away by the production of heat. Some fraction of the shower energy, however, goes to the production of scintillation light or ionization charge which can be readily detected by conventional methods. Calorimetry is possible because the number of particles in a shower is directly proportional to the energy of an incident particle. Since it is the low energy shower particles that put a relatively constant fraction of their energy into the calorimeter signal then the signal itself is directly proportional to the energy of the incident particle.

The technologies available for calorimeter development can be grouped into two broad categories, homogeneous and sampling calorimeters. The homogeneous calorimeters are also called total absorption calorimeters, by virtue of their ability to measure the energy of an entire shower. Homogeneous calorimeters are built of blocks of a single material, such as lead glass or NaI. By allowing the shower to develop within one material these calorimeters maximize the amount signal that is measured from a shower. Sampling calorimeters have layers of an inactive absorber material interleaved with an active sampling medium. The inactive material absorbs most of the shower energy and produces no signal. The sampling layers then sample the shower energy at periodic points within the detector.

Homogeneous calorimeters, such as lead glass, have intrinsically better energy resolution for electromagnetic showers. If electronics effects are ignored, they are limited only by the fluctuations of the shower. This is unlike sampling calorimeters, which are dominated by the

fluctuations introduced from sampling the energy. The two categories of calorimeters can be subdivided according to the readout scheme, ie. whether it is strip readout or pad (See Fig.11). Homogeneous calorimeters tend to be constructed with a pad type readout while sampling calorimeters tend to have a strip type readout. Building a homogeneous calorimeter that can satisfy both the need for fine granularity and a fast p_T trigger virtually demands that it have a pad type readout. If one compares the number of channels between a calorimeter with a strip type read out and a calorimeter with a pad type readout, where the calorimeters have comparable spatial resolution, then the number of pads is approximately the square of one half the number of strips. A pad type readout then becomes extremely expensive because of the number of electrical channels involved. If each channel of electronics cost \$50 then a 10,000 channel strip calorimeter has \$500,000 in electronics costs and an equivalent pad type readout would need 25,000,000 pads and cost \$1,250,000,000. A Sampling calorimeter structure with a strip readout was selected for E-706 because of this.

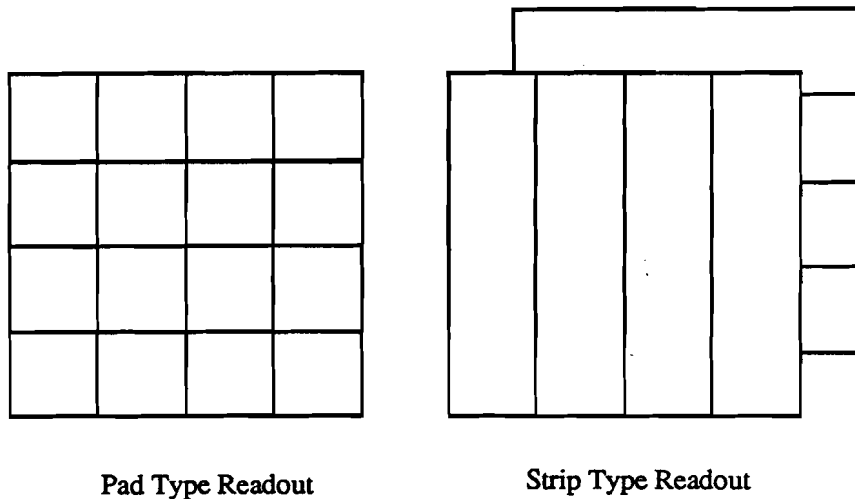


Figure 11: Drawing of Two Types of Calorimeter Readout Schemes

There are several options for measuring the deposited energy with a sampling calorimeter. The active layers can be constructed of scintillator with phototube readout, proportional wire chambers, or ionization chambers with capacitive readout. As with absorption calorimeters it is difficult to achieve a finely segmented detector which can provide a signal proportional to p_T at a reasonable cost using PWCs or scintillator. There are other problems with using PWCs or scintillator. The energy resolution that can be achieved with PWCs is worse than that for liquid argon because of the increased importance of Landau fluctuations and path length fluctuations^[2]. Further problems with PWCs are the limited dynamical range ($\approx 20 : 1$)^[3] and lack of stability due to pressure and temperature variations. Scintillators also have problems with long term stability due to radiation damage. Position dependence of the output pulse height due to nonuniformities in the scintillator doping is also a problem.

A calorimeter that uses liquid argon does not have the rate capabilities of one made with scintillator or PWCs. An added complication is the necessity of maintaining a cryogenic environment, which adds to the construction and maintenance cost. It can, however, sustain interaction rates of the order of 1×10^6 and has superior stability and potentially better energy resolution because the systematic effects are easier to control^[4]. This last point is very important, if one hopes to measure the direct diphoton cross section or constrain the kinematics sufficiently so that the structure functions can be extracted. Liquid argon has the added advantage that a readout geometry which yields a signal proportional to p_T is easily constructed. For these reasons it was decided to use liquid argon calorimetry to study direct photon physics.

[2] Ugo Amaldi, "Fluctuations in Calorimetry Measurements", *Physica Scripta*, Vol.23, pp.409-424, (1981).

[3] F. Lobkowicz, op. cit, p.III-2.

[4] C. W. Fabjan and T. Ludlam, "Calorimetry in High-Energy Physics", *Annual Review of Nuclear and Particle Science*, Vol. 32, pp. 335-389, (1982).

III.2 Design of the EMLAC

The design of a calorimeter generally focuses on four points: energy resolution, spatial resolution, particle identification, and rate. To optimize the energy resolution the calorimeter must be thick enough to contain the particle showers since any leakage of energy through the back degrades the resolution. For sampling calorimeters the width of the absorbers and sampling medium determine the sampling frequency. This greatly influences the energy resolution especially for electromagnetic showers where it is dominated by sampling fluctuations. The spatial resolution is determined to a large extent by the degree of lateral segmentation of the sampling medium and to a lesser extent by the degree of longitudinal segmentation. Nevertheless, there are limits to the achievable resolution due to the spatial distribution of the showers.

The amount of lateral and longitudinal segmentation also greatly influences the detector's particle identification ability. The interaction rate that is sustainable by a calorimeter depends in large part on the sampling medium used. What follows in this section is a detailed consideration of these points for the EMLAC.

III.2.1 Determination of the EMLAC Depth

In building a calorimeter that has the capability to distinguish between electromagnetic particles, such as photons and electrons, and hadronic particles the absorber material should have a small radiation length (X_0), so that the electromagnetic particles will shower quickly and deposit their energy in the shortest distance along the initial direction of motion. The material should also have a large interaction length (λ_I) compared to X_0 so that the hadronic particles have a larger longitudinal shower distribution relative to electromagnetic showers. This aids in distinguishing between the two types of particles by enhancing the difference in their patterns of longitudinal energy deposition. Now $X_0 \approx 180A/Z^2\text{g/cm}^2$ and $\lambda_I \approx 35A^{1/3}\text{g/cm}^2$, where Z is the atomic number of the material and A is the atomic weight^[5]. From the above definitions it

[5] Ugo Amaldi, op. cit., p. 411.

can be seen that $X_0/\lambda_I \approx 5A^{2/3}/Z^2$ and that a low value of this ratio is dominated by materials with high Z . Lead is an excellent material for this purpose. With a radiation length of 0.56 cm and an interaction length of 17.1 cm there are few materials, produced in quantity, that are better for this purpose. Bismuth, and uranium have a higher Z and are produced in limited quantities, but are considerably more expensive than lead.

While lead is readily available from industry at a moderate cost, there are a couple of drawbacks to using lead as the absorbing material. One is that it has a high coefficient of thermal expansion which can cause difficulties when the detector is in a cryogenic environment. Another problem with using lead is that it is a relatively soft and malleable material. This makes it difficult to build a structurally stable detector of large mass. The ideal absorber material would have the structural properties of steel with the radiation properties of lead. Other materials such as uranium or bismuth have comparable radiation properties and better structural properties but are difficult to manufacture and very expensive. Still other materials, like copper and steel which are readily available and inexpensive, have less attractive radiation properties. If steel were used instead of lead as the absorber material, with a radiation length of 1.76 cm and an interaction length of 16.8 cm, it would take steel absorbers three times as thick as ones made of lead to build a detector with the same number of radiation lengths. At the same time the number of interaction lengths would triple and the detector mass would double.

A detector built with steel absorbers would have a worse electron/hadron resolution than one with lead absorbers. In principle, the steel calorimeter could have improved energy resolution by creating more cells with thinner absorbers. The improved resolution comes at the price of a rise in the noise seen by the channel amplifiers. This is a result of the increase in channel capacitance from more strips being tied to each amplifier^[6]. Furthermore, the cost savings will not equal the price difference between lead and steel. Because of the cryogenic environment, it

[6] W. J. Willis and V. Radeka, "Liquid-Argon Ionization Chambers as Total-Absorption Detectors", *Nuclear Instruments and Methods*, Vol. 120, pp. 221-236, (1974).

might be necessary to use costlier stainless steel to avoid the brittleness problems of carbon steel. With the finer segmentation there is an attendant increase in the number of detector components, such as anode boards and spacers, with a corresponding increase in the cost of the calorimeter^[7].

To construct a calorimeter with good energy resolution it is important to contain the longitudinal development of the showers at the energy of interest. For electromagnetic showers the depth of the calorimeter to contain a specified fraction of the shower energy can be found from the equation^[8]:

$$L(98\%) \approx 2.6 \left(\ln\left(\frac{E}{\epsilon}\right) + a - 1.5 \right) @ 100 \text{ GeV/c} \quad (a = 0.4 \text{ for } e' \text{'s}, 1.2 \text{ for } \gamma' \text{'s}) \quad (12)$$

where L is in units of radiation lengths (X_0) and the critical energy ϵ for ionizing particles is given roughly by:

$$\epsilon \approx \frac{550 \text{ MeV}}{Z} \quad (13)$$

For 800 GeV/c incident protons or 530 GeV/c incident pions the parton constituents carry on average 135 GeV/c momentum, which can serve as an upper bound on the energies of interest. Calculation, using $Z = 82$ for Pb, yields $L(98\%) = 25.0 X_0$ ^[9]. The EMLAC as designed has a sensitive volume $26.76 X_0$ thick with $2.34 X_0$ of material in front of the sensitive volume.

III.2.2 Selection of the EMLAC Argon Gap Thickness and Sampling Frequency

Selection of the width of the argon gap is a balance between the desire to maximize the signal to noise ratio by increasing the width and the need to maximize the rate of the calorimeter by decreasing the gap width. Starting with the latter criteria, ie. the data rate, one can impose an upper limit on the gap thickness.

[7] F. Lobkowicz, *ibid*, p.III-5.

[8] Ugo Amaldi, *op. cit.*, p.414.

[9] Tom Ferbel, "Remarks on E706 Calorimetry, *E-706 Internal Note 049*, (1982).

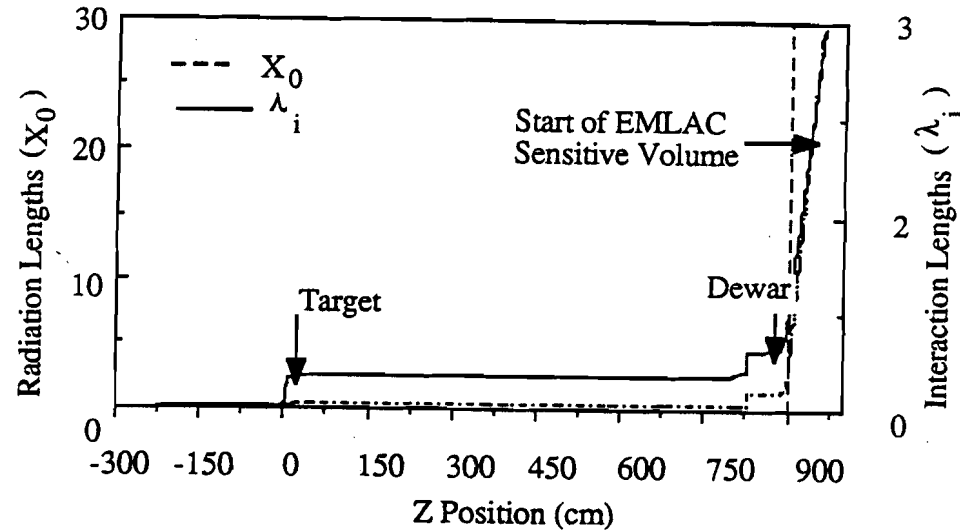


Figure 12: Plot of the Accumulated Material Thickness in Radiation Lengths vs. Z Position for the E-706 Spectrometer

At the most elementary level the rate achievable by an argon calorimeter is directly related to the risetime of the signal or rather the time it takes electrons to drift across the ionization gap. For a 1 MHz device this means signals with a 1 μ s risetime. The amount of charge collected in a time t on the anode of an ionization cell can be found from the formula^[10]

$$q(t) = Ne \left(\frac{tv_d}{d} - \frac{1}{2} \left(\frac{tv_d}{d} \right)^2 \right); t < \frac{d}{v_d}, \quad (14)$$

where v_d is the drift velocity of the electrons, d is the argon gap width, and Ne is the amount of charge deposited in the gap. From this the maximum amount of charge that can be collected is $Ne/2$ and if the risetime t_R is defined to be the time to collect from 10-90% of the charge then:

$$t_R = .63 \frac{d}{v_d}. \quad (15)$$

^[10] W. J. Willis, op. cit..

If the ionization cells are operated with an electric field of 10 kV/cm then $v_d = 4.5 \times 10^5 \text{ cm/s}$ ^[11]. So, to achieve a 1 μs risetime the gap width can be no larger than .7 cm and no larger than .35 cm for a 0.5 μs risetime or a 2 MHz rate.

The lower limit on the gap thickness is governed by the desired signal to noise ratio or alternatively the intrinsic energy resolution. The energy resolution of sampling calorimeters is limited by the fluctuations introduced by sampling the deposited energy. This is equivalent to the fluctuations in the number of charged tracks N crossing the sampling cells. Assuming that the energy is deposited solely by minimum ionizing particles and that the track crossings are independent, then;

$$\left(\frac{\sigma(E)}{E}\right)_{Sampling} \approx \frac{1}{\sqrt{N}}. \quad (16)$$

After correcting for scattering of low energy electrons and introducing a cutoff in the energy detectable by a calorimeter, the energy resolution limit of the EMLAC due to sampling fluctuations can be estimated with the use of the following formula^[12]:

$$\left(\frac{\sigma(E)}{E}\right)_{Sampling} = 3.2\% \sqrt{\frac{\epsilon}{F(z) \cos(E_s/\pi\epsilon)}} \sqrt{\frac{t}{E}}. \quad (17)$$

In Eq.(17), E is the particle energy in GeV, $\epsilon \approx 550/Z$ (MeV) is the critical energy of electrons in the absorber material, $E_s = 21 \text{ MeV}$ is the multiple scattering constant, t is the thickness of the sampling layers in units of radiation lengths, and $F(z)$ is the fraction of useful energy deposited in the calorimeter. $F(z)$ is defined as:

$$F(z) \approx \exp z(1 + z \ln(z/1.525)), z = 4.58 \frac{Z}{A} \frac{E_c}{\epsilon}, \quad (18)$$

[11] L. S. Miller, S. Howe, W. E. Spear, "Charge Transport in Solid and Liquid Ar, Kr, and Xe", *Physical Review*, Vol 166, No. 3, pp. 871-878, (1968).

[12] Ugo Amaldi, *op. cit.* p. 413.

where E_c is the cutoff energy or minimum energy detectable by the calorimeter and Z and A are the atomic number and mass of the absorber material. E_c can be estimated as half the energy deposited in one active layer of the calorimeter by one minimum ionizing particle:

$$E_c = \frac{z_a}{2} \frac{\delta E}{\delta z}. \quad (19)$$

In addition to sampling errors there are variations in the measured energy resulting from path length fluctuations of the showering particles and fluctuations in the way individual charged particles deposit their energy in a medium, better known as Landau fluctuations. For calorimeters with dense active layers such as liquid argon they are less important than sampling fluctuations. These contributions can be taken into account with the formula^[13],

$$\left(\frac{\sigma(E)}{E}\right)_{Landau} \approx \frac{1}{\sqrt{N}} \frac{2}{\ln(10^4 z)}, \quad (20)$$

where z is the thickness of a detector cell in g/cm^2 . The energy resolution can then be written as:

$$\left(\frac{\sigma(E)}{E}\right) = \left(\frac{\sigma(E)}{E}\right)_{Sampling} \left(1 + \left(\frac{2}{\ln(10^4 z)}\right)^2\right)^{\frac{1}{2}}. \quad (21)$$

Optimally, the lead absorber plates should be as thin as is practical until noise from such sources as strip capacitance begins to dominate over sampling fluctuations. The thinnest lead plate currently available from industrial sources is 2.0 mm. This leaves the size of the argon gap to determine the resolution. One can study the effect of the argon gap size on the intrinsic energy resolution using Eq.21. As can be seen in Fig.13, there is not a great deal of variation in the resolution over the range of gap thickness that is of interest. From this, the conclusion can be drawn that it is the risetime which is the factor of importance in choosing the gap thickness.

In making the argon gaps narrower one must beware that as the average distance between the anodes and cathodes shrinks the high voltage applied to the gap will become less stable.

[13] Ugo Amaldi, op. cit., p.415.

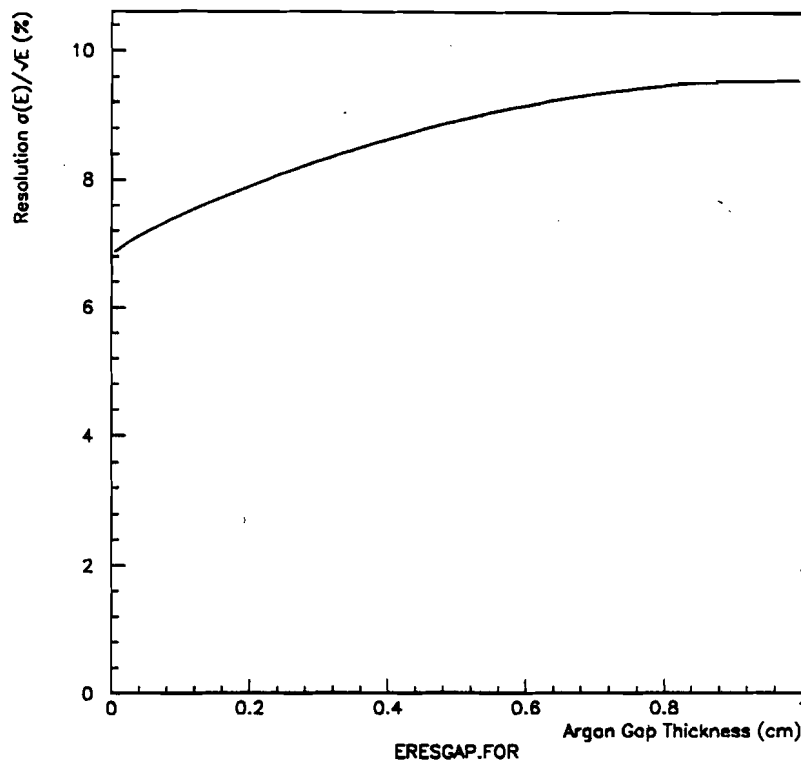


Figure 13: Effect of Argon Gap Thickness on Intrinsic Energy Resolution

Thickness variations and waves in the electrodes will be more likely to cause the voltage to arc from one to the other causing damage to the electronics. The gap thickness finally chosen was 0.25 cm. This determines a limiting rate for the calorimeter of 2.9 MHz and an intrinsic resolution of $\sigma(E)/E = 8\%/\sqrt{E}$.

This estimate put only a lower bound on the energy resolution. It has not taken into account the variations in the thickness of the lead absorbers or the argon sampling gaps. Nor does it account for electronics effects such as capacitance noise and gain variations. These and other effects conspire to degrade the resolution of the detector. A more realistic approach is to

base the estimate of the energy resolution on previous experience. Thus the expected energy resolution based on results from a previous detector of similar design is $\Delta E/E = 14\%/\sqrt{E}$ ^[14].

One further point should be made about timing in the calorimeter. Given the caveat that the hit rate for individual channels is substantially lower than the interaction rate, then the timing resolution is not the same as the rate at which data can be taken. The former is a measure of the limit one can reliably separate two different events in time while the latter is the limit that one can reliably measure the energy of an event.

III.2.3 Selection of r/ϕ Focused Geometry for the EMLAC

A trigger that identifies candidate events is important to reduce the number of events that must be sifted through to find direct photon events. Given a hadron and a photon of the same energy the hadronic shower is much broader in both its lateral and longitudinal development. This implies that hadronic showers deposit less energy over a larger number of strips than electromagnetic showers. Thus, an expedient method to trigger on high p_T direct photon events is for the calorimeter to provide a signal indicating the presence of a highly localized concentration of deposited energy with a significant amount of p_T .

To do this with a simple X,Y geometry would require a complicated electronic system that could properly weight and correlate the X and Y views of the event, then add them together, and then discriminate between all of the possible combinations to properly identify candidate events. In addition this must all be done within a relatively short amount of time. This is obviously a formidable if not impossible task. However, if an r/ϕ geometry is chosen, then there is no need to do the correlations of the X,Y views since the r view automatically provides an immediate estimate of the amount of p_T inherent in the shower, considerably simplifying the task at hand.

^[14] C. Nelson, "Operational Performance of a Large Liquid Argon Photon Calorimeter", *Nuclear Instruments and Methods*, Vol. 216, pp. 381-391, (1983).

If in addition the geometry is constructed so that it focuses at the target (See Fig.14) then there is no complex adding of strips within the r -view since energy deposited within a unit of solid angle defined by one strip is almost completely confined within that strip to the approximation that multiple scattering is considered insignificant. Thus a p_T trigger becomes a matter of weighting the r -strips in an appropriate fashion, adding the signals from a set of adjacent strips together where that set is large enough to contain the lateral development of a typical electromagnetic shower, and then discriminating the result against the combinations of the neighboring sets of strips to see if the shower is isolated.

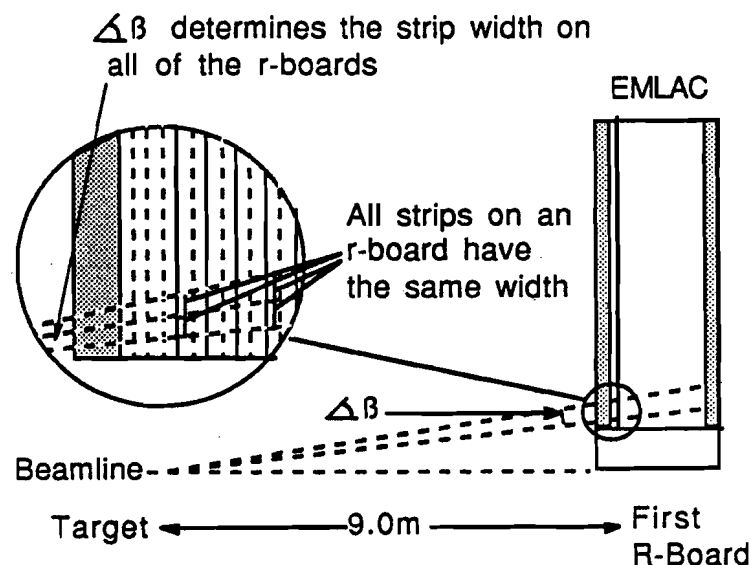


Figure 14: Cut View Drawing of the EMLAC Illustrating R-Strip Focusing

To this end the readout of the EMLAC has been broken into four quadrants of a circle centered on the beamline. Each quadrant is broken into octants and is divided longitudinally into two sections, front and back. Each octant has alternating layers of anode boards with either

radius position measuring strips(r-strips) or azimuthal position measuring strips(ϕ -strips). The r-strips are designed to focus at the target. The ϕ -strips are broken into inner and outer sections by a focused boundary at a radius of 40 cm.

III.2.4 Selection of the EMLAC Strip Width for γ/π^0 Separation

As pointed out in Chapter I, it is extremely important to be able to distinguish between a γ and a π^0 with a high degree of accuracy in order to extract reliable data for direct photon physics. The selection of an appropriate width for the calorimeter's anode strips can significantly enhance this ability. To get a feel for the dimensions involved, the minimum separation of two photons from a 100 GeV/c π^0 at distance of 9 m from the target is 2.5 cm. The ability to distinguish a γ from a π^0 is limited by the natural width of electromagnetic showers. This obscures highly energetic π^0 decays, making them appear as single photon showers and implies that decreasing the strip width beyond a certain point does nothing to increase the detectors ability to resolve a π^0 and may begin to adversely affect the energy resolution because of increased noise and fluctuations in the shower distributions.

A Monte Carlo study was performed to determine the optimum strip width for the EMLAC. Using the shower shape for a photon determined from experiment E-629, π^0 distributions with selected asymmetries were generated. These distributions included energy fluctuations introduced into each strip from a normal distribution of mean zero and variance:

$$\sigma(\Delta E_i)^2 = (0.14)^2 E_i + q \times \left(\frac{w}{1.25\text{cm}}\right)^n \quad (22)$$

The first term of the variance represents the intrinsic fluctuation of energy in a sampling calorimeter based on experience from E-272. The second term is a noise contribution from the capacitance of the detector strips which depends on the strip width(w) and the effective noise per channel $q = 0.0007 \text{ GeV}^2$. Taking $\Gamma(\delta^2)$ and $\Pi(\delta^2)$ as the distributions of:

$$\delta_{\gamma/\pi^0}^2 = \frac{\sum_i E_i (x_i - \bar{x})^2}{\sum_i E_i} + \frac{\sum_j E_j (y_j - \bar{y})^2}{\sum_j E_j} \quad (23)$$

for the γ 's and π^0 's respectively then one can find the distribution:

$$\rho(\xi), \xi = \frac{(\delta_{\pi^0}^2 - \delta_\gamma^2)}{\sqrt{\sigma_{\pi^0}^2 - \sigma_\gamma^2}} \quad (24)$$

The decision algorithm used minimized of the probability $P(\delta_{\pi^0}^2 < \delta_\gamma^2)$, where the strip width dependence enters only through the variances of $\Gamma(\delta^2)$ and $\Pi(\delta^2)$, $\sigma_{\pi^0}^2$ and σ_γ^2 ^[15]. This is because $\delta_{\pi^0}^2$ related to δ_γ^2 by the "Walker Mass" formula^[16] and contain no strip width dependencies. Results indicate that a strip width of 6 mm is optimum (See Fig.15).

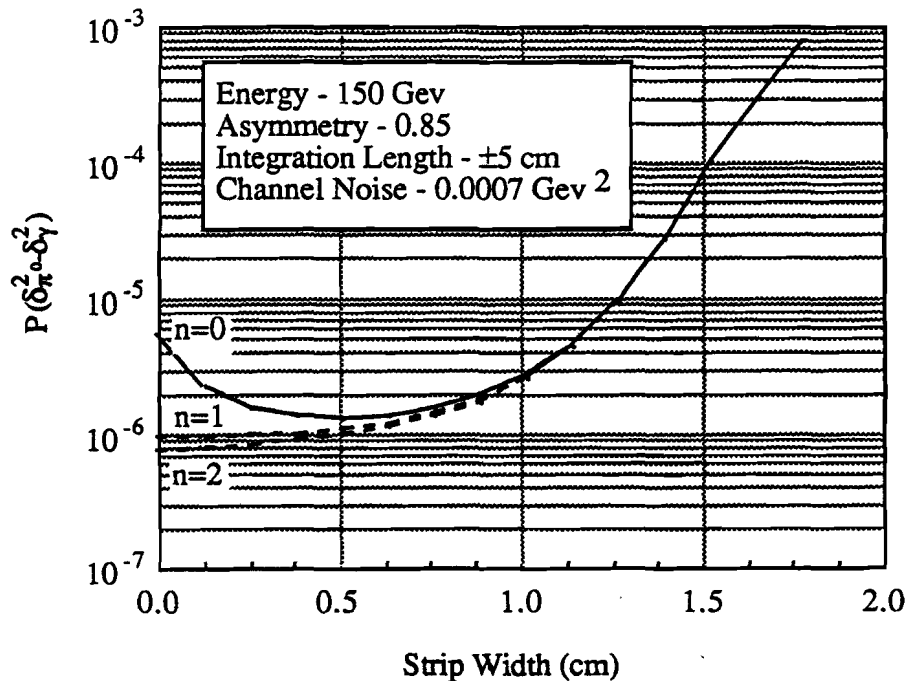


Figure 15: Plot of the Probability that the Width of a Pi-Zero is less than the width of a Photon versus Strip Width

^[15] D.Dunlap, "Comments on Optimal Strip Width of LAC", E-706 Internal Note 042.

^[16] R. L. Walker, "Identification of π^0 , η , and X^0 ", CTSI internal Report, May 14, 1971.

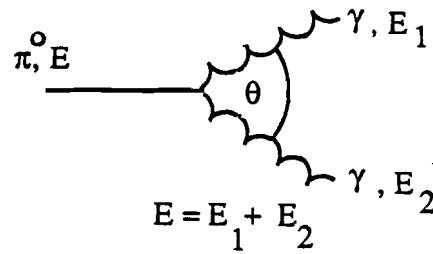


Figure 16: Diagram of a π^0 Decay

III.2.5 Determination of the EMLAC Front/Back Ratio

Selection of the proper front/back thickness ratio for the EMLAC is critical for two reasons. One is the ability to discriminate between electromagnetic and hadronic showers, the other is the need for good π^0 resolution. Electrons tend to shower early and deposit most of their energy in the front of the calorimeter, while hadrons tend to shower later and deposit more energy in the back of the calorimeter. A 50/50 split might have been sufficient to give the EMLAC a good e/h discrimination. Having a hadronic calorimeter downstream of the EMLAC reduces the need for good e/h discrimination in the EMLAC. This makes the π^0 resolution the determining factor for the front/back ratio.

When discussing the decay of π^0 's it is useful to define a quantity called the decay asymmetry α ,

$$\alpha = \frac{|E_1 - E_2|}{E_1 + E_2}, \quad (25)$$

where E_1 and E_2 are the energies of the two photons from the π^0 decay. From the kinematics of the decay one can find the angle of decay θ between the two photons as a function of α ,

$$\cos(\theta) = 1 - \frac{2m_{\pi^0}^2}{E^2(1 - \alpha^2)}, \quad (26)$$

where m_{π^0} is the mass of the π^0 and $E = E_1 + E_2$. This relation indicates that as the asymmetry increases so does the angle between the photons.

Because electromagnetic showers generally start in the front of the EMLAC it is desirable to make the front section substantially thinner than the back section. This allows one to separate the two showers from a π^0 decay before they reach their full lateral spread^[17]. This becomes more important for highly energetic π^0 's with a small decay asymmetry. At high energies the two showers begin to coalesce and appear as a single shower. To determine the optimum ratio, computer studies were done by Selcuk Cihangir and Dave Dunlap using the EGS software package from CERN. These studies showed that the ability of the EMLAC to resolve photons from highly asymmetric π^0 decays was optimized at a front/back ratio of 15/51 layers (See Fig.17). Because of concern over the capacitance of strips in the back section affecting the energy resolution, a front/back ratio of 11/22 layers was chosen^[18].

Once the lateral and longitudinal segmentation parameters were chosen, the position resolution of the detector could be modeled by Monte Carlo methods. Results of this study indicate that for single photon showers the position resolution for the r -view is $\sigma_r = 0.25$ mm and for the ϕ -view is $\sigma_\phi = 0.5$ mr. Longitudinal segmentation of the calorimeter allows for the determination of the directionality of particles passing through it. This is very useful for eliminating stray particles such as halo muons which are not part of the event structure. Given the predicted spatial resolution the expected directional resolution is $\sigma_\theta = 5$ mr^[19].

III.2.6 EMLAC Acceptance

A large calorimeter with uniform 2π acceptance around the beamline can redress some of the trigger bias that is a problem with single arm detectors (See Fig.18). Detector systems with a p_T trigger preferentially select events in which the intrinsic k_t of the colliding partons are collinear. This biases the measured cross section towards higher p_T . A detector system with

[17] Dave Dunlap, "How Front/Back Separations Affect the Shower Shape", *E-706 Internal Note 075*.

[18] Tom Ferbel, "Comment on Front/Back Separation for EMLAC", *E-706 internal note 056*.

[19] S. Hossain, E. Pothier, and G. Ballocchi, "Photon Reconstruction in E706 Liquid Argon Calorimeter", *E-706 Internal Note 130*, (1985).

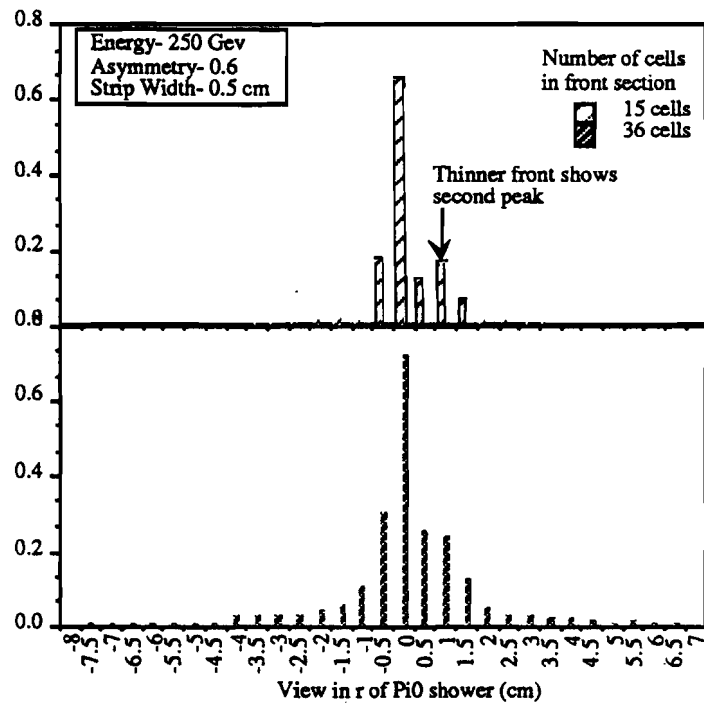


Figure 17: Plots of Energy Distributions for Different EMLAC Front/Back Ratios.

uniform acceptance can trigger on a p_T signal while measuring the p_T of the opposite side jet. This can help determine part of the trigger bias by measuring the p_T imbalance between the recoiling jets. For two photon events it is possible for the EMLAC to measure the p_T balance but for single photon plus jet events input from the HALAC is required.

To estimate the geometrical acceptance of the calorimeter one needs to relate the center of momentum frame of reference *com* scattering angles to the laboratory frame of reference *Lab* angles. This can be accomplished by taking the ratio of the transverse momentum to the longitudinal momentum for a scattered particle in the *Lab* frame and then transforming the momentum to the *com* frame. The resulting equation relates the tangent of the *Lab* angle (ψ)

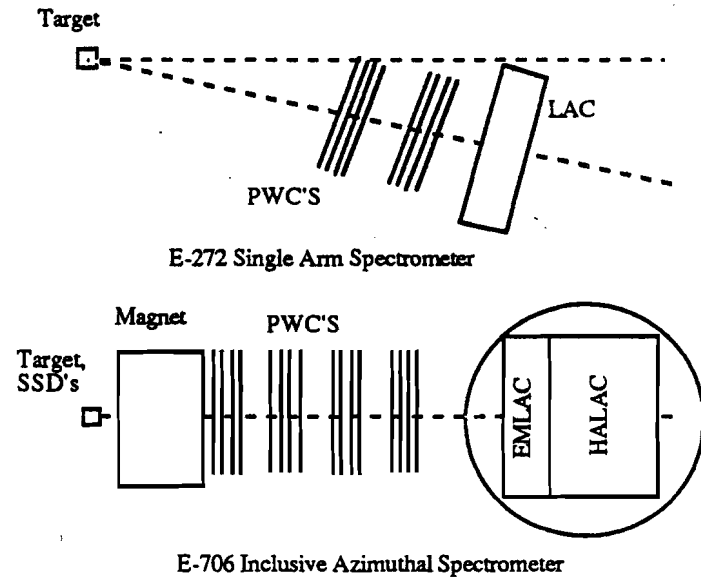


Figure 18: Examples of Layouts for Single Arm and Inclusive Experiments.

as a function of the *com* angle (θ):

$$\tan(\psi) = \frac{P_{Trans}}{P_{Long} \cdot E_{Lab}} = \frac{1}{\gamma_{com} \cos(\theta) + \beta_{com}} \sin(\theta) \quad (27)$$

where,

$$\gamma_{com} = \frac{(m_\pi^2 + m_n^2 + 2m_n E_{Lab})^{1/2}}{E_{Lab} + m_n}, \quad \beta_{com} = \frac{E_{Lab}}{E_{Lab} + m_n} \quad (28)$$

and E_{Lab} equals 530 GeV/c, m_π equals 139 MeV, and m_n equals 938 MeV. The relativistic limit $E_{Lab} = P_{Lab}$ has been taken here.

In estimating the angular acceptance, the radial distances listed below are 9.0 m from the target in the laboratory frame of reference. The angles listed are in the center of momentum frame of reference. The extreme radial boundaries for the EMLAC sensitive area are at 21.6 cm and 150.4 cm. These correspond to ϕ angles of 44° and 141° in the *com* frame. The inner/outer

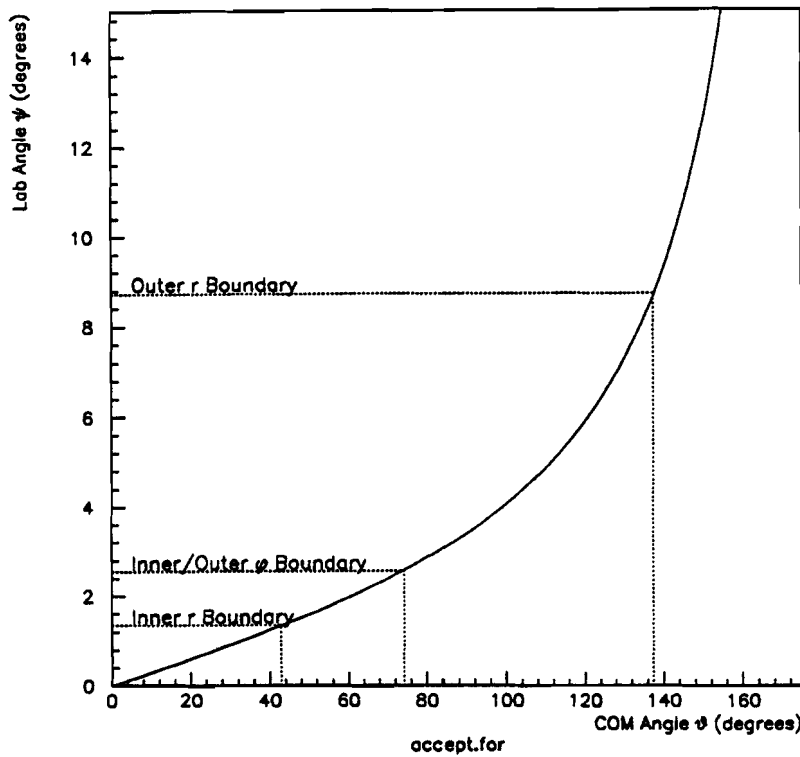


Figure 19: Plot of Lab Angle versus COM angle to Illustrate EMLAC Acceptance

ϕ strip boundary at a 40 cm radius was supposed to correspond to 90° in the com frame for 530 GeV/c pions, it is closer to 74° (See Fig.19).

In designing a calorimeter it is desirable to minimize the area that is made inactive by the presence of mechanical support and signal readout structures. This is important, because the size of the effective active area is reduced by more than the size of the dead area. Because one of the photons from a π^0 decay can disappear into these inactive regions, as it can near the edges of the detector annulus, there is a resulting increase in the background to direct photon production. This can be ameliorated to an extent by imposing fiducial cuts which would require any π^0 decay to be completely contained within the active region of the calorimeter. The price

that is paid for this a reduction of the effective acceptance of the detector and a corresponding increase in the uncertainty of the measurements of the cross sections. With some calorimeter designs, such as lead glass arrays, this is not much of a problem because all of the readout is done at the back of the calorimeter. This is not so for the EMLAC. With its geometry of charge sampling strips, the readout creates a significant amount of dead space within the annulus of the detector (See Fig.21). The amount of dead area in the EMLAC was minimized without compromising the structural integrity of the detector.

The dead areas along the radial edges of an EMLAC quadrant can be bound by a line that is 2.9° from the X or Y axis. Calculation of the solid angle included by the EMLAC yields a value of 6.4 str. The lateral spread of electromagnetic showers must be taken into account since a shower with its peak at or near the edge of a quadrant can not be reliably reconstructed. It has been found that about 95% of the energy of a shower is contained within a cylinder with a radius of twice the Molière radius (R_M)^[20]:

$$R(95\%) = 2R_M \approx 14 \frac{A}{Z} \frac{g}{cm}, \quad (29)$$

which corresponds to about 3.1 cm in lead. With this in mind the effective acceptance of the EMLAC is then 5.1 str or 41% of the *COM* solid angle.

III.3 Design of the HALAC

The attainable energy resolution of hadronic showers is much worse than that of electromagnetic showers. Part of the energy from a hadronic shower escapes as ν 's and μ 's from the decays of π s and K s. Energy is also lost in compensating for the binding energy involved in the breakup of nuclei and in the loss of neutrons produced in these interactions. Approximately one to two thirds of the hadrons in a shower are π^0 's that decay into γ 's forming electromagnetic showers. The presence of two different types of showers complicates matters. If the first

[20] Ugo Amaldi, op. cit., p. 411.

interaction of the hadron is of the charge exchange type then the fraction of energy dissipated as electromagnetic showers, " f_{π^0} ", is large otherwise it can be very small. If the response to the electromagnetic and hadronic components are not the same, ie. $e/h^{intr} \neq 1$, then the large nongaussian fluctuations of f_{π^0} will cause the energy resolution not to scale as $E^{-1/2}$ [21].

Since the EMLAC uses liquid argon as its sensitive medium there are fewer complications if the HALAC is based on liquid argon. The electronics used for the EMLAC can be employed by the HALAC. This keeps to a minimum the number of different systems used by the experiment. Putting the HALAC in the dewar with the EMLAC also simplifies the design of the dewar. With just the EMLAC the dewar would probably have been oval in shape to reduce the material thickness between the EMLAC and HALAC. Unfortunately, an oval dewar requires a thicker wall to meet the construction codes for pressure vessels than does a cylindrical dewar. With the HALAC inside, the dewar could be cylindrical in shape and made of thinner material. This puts less material between the calorimeter and the target, which is always desirable.

III.3.1 Determination of HALAC Depth

The amount of absorber material needed to longitudinally contain a hadronic shower can be estimated with the formula^[22]:

$$L(95\%) = A(0.54\ln(E) + 0.4)\lambda_i. \quad (30)$$

Here E is in GeV, A is 2.5 if L is in units of interaction lengths λ_i . For a 200 GeV/c pion the formula gives $8.15\lambda_i$ or 136.6 cm of iron. The resolution of a calorimeter is very sensitive to longitudinal containment of energy, so for $A = 3.0$, $L(99\%) = 9.78\lambda_i$ or 168.2 cm Fe^[23]. With 2.03 interaction lengths of material already contained in the EMLAC (See Fig.12), this leaves

[21] R. Wigmans, "On the Energy Resolution of Uranium and Other Hadron Calorimeters", *Nuclear Instruments and Methods*, Vol. A259, pp. 389-429, (1987).

[22] U. Amaldi, op. cit., p. 419.

[23] J. Huston, "Some Remarks on E706 Calorimetry", *E-706 Internal Note 055*, (1983).

7.75 interaction lengths to be built into the HALAC or 133.3 cm of Fe. Steel can be used in the HALAC because electron/hadron discrimination is done by the EMLAC and it is cheaper. One can turn the question of containment around and ask what percentage of hadronic showers of a given energy will penetrate a calorimeter that is $9.78\lambda_i$ thick. Examination of experimental data reveals that about 60% of all showers from 200 GeV/c hadrons will to some extent penetrate through the calorimeter. Even for 25 GeV/c hadrons, about 6% will penetrate though. Most of this leakage is due to decay muons^[24]. Clearly, complete containment of a hadron shower is a battle of diminishing returns. The best that can be hoped for is to contain the hadrons and correct the energy for muons using Monte Carlo methods.

III.3.2 Selection of HALAC Argon Gap Thickness and Sampling Frequency

In selecting the sampling frequency a balance between the cost of the sampling components and the desired resolution must be struck. In the case of the HALAC there is an additional constraint, that of size. Because the LAC is based on a liquid argon active medium it requires a pressure vessel to contain the cryogenic environment. Making the HALAC larger requires making the dewar larger. This entails a thicker dewar which puts additional material in front of the EMLAC that worsens its resolution. This means that it was desirable to minimize the depth of the HALAC which in turn meant minimizing the sampling frequency.

Selection of the steel absorber thickness for the HALAC was based on a Monte Carlo study of liquid argon/steel calorimeters^[25]. The HALAC was originally designed with 1 cm plates. Various constraints, such as the one detailed above, forced the HALAC design to have 72 steel plates 1.9 cm thick. It was thought that the increased absorber thickness would have only a minor affect on the energy resolution, ie. $80\%/\sqrt{E}$ for 1.9 cm steel instead of $75\%/\sqrt{E}$ for

[24] F. S. Merritt, et. al., "Hadron Shower Punchthrough for Incident Hadrons of Momentum 15, 25, 50, 100, 200, and 300 GeV/c", *Nuclear Instruments and Methods*, Vol A245, pp. 27 - 34, (1986).

[25] T. A. Gabriel, et.al., "", *Nuclear Instruments and Methods*, Vol. 134, p.271.

1.0 cm steel^[26]. Unfortunately, a steel plate that is 1.9 cm thick does not necessarily take up only 1.9 cm of space. When steel plate is produced, it is rolled from an ingot. Because steel is a mechanically stiff material the plate will have a certain amount of warpage that results from its being rolled. This causes the plates to occupy more space than their thickness would indicate because they can not be compressed without damaging the sensitive planes. Because the size of the dewar was fixed, when the flatness requirements for the steel could not be met by the manufacturer the HALAC was redesigned to have 52 plates 2.5 cm thick for a total of 132.1 cm of Fe.

Hindsight now says that the hadronic energy resolution of a steel/liquid argon calorimeter cannot be parametrized in a simple manner. An inability to convert thermal neutrons into measurable energy makes it impossible for this type of calorimeter to have the parameter e/h^{intr} equal to one. This means that the resolution depends upon f_{π^0} and cannot scale as $E^{-1/2}$. Detailed computer calculations indicate that the best energy resolution likely for a calorimeter with 2.5 mm argon gaps and 2.5 cm steel absorbers is 110%/ \sqrt{E} for 100 GeV Hadrons^[27].

The width of the argon gap for the HALAC was chosen to be 3 mm which implies a maximum rate of 2.4 MHz. The reason for the increase size of the gap width over that of the EMLAC was to increase the signal height for HALAC, which has thicker absorbers than the EMLAC. This increased width does not significantly affect the intrinsic rate of the calorimeter.

III.3.3 Selection of HALAC Pad Size

Hadronic showers are rather broad by the time they reach the HALAC. This obviates the need for fine spatial segmentation. A pattern of strips similar to that used in the EMLAC could be used but the channel noise would be much larger than in the EMLAC because of the larger strip capacitances. Instead of strips a pad readout could be used. This entails a larger cost due

[26] J. Huston,, op. cit., p.12.

[27] R. Wigmans, op.cit., p. 426.

to the increased number of electronics channels but each channel will have lower noise levels from the reduced channel capacitance. More important, however, is the resulting simplification of the software for reconstructing hadron showers. Towers of pads do not require the correlation of energy deposited in two views that has to be done for the reconstruction of showers in the EMLAC^[28].

To this end the HALAC has been designed with charge readout boards that are pertiled with pads that are equilateral triangles. By grouping the triangles into hexagons of various sizes the calorimeter can be tessellated into intervals of constant rapidity and azimuth(See Fig.20). This structure lends itself to the formation of a p_T type trigger should it be desirable to study "jet" physics at some future date. The characteristics of hadronic showers were studied by the Monte Carlo method^[29]and the pad size was chosen so that 93% of the energy would be contained in a hexagon formed from six triangles. Like the EMLAC r-strips, the HALAC pads grow in size and change in radial position so that a tower of pads focuses on the target. The pads increase in size from 10.8 cm to 13.7 cm and are addressed by a three axis coordinate system^[30](See Fig.20). This focusing causes some of the triangles to drop off the edge of the detector planes as the Z position of the detector plane increases.

III.3.4 Selection of the HALAC Front to Back Ratio

The HALAC was divided longitudinally into two sections. There are thirteen layers in the front section and thirty nine layers in the back section. When the front section is taken together with the EMLAC the ratio of the interaction lengths of the front to back sections is of the proportion one to two. This was done principally to keep the noise due to capacitance fluctuations at a uniform minimum for all channels^[31]. There are two reasons for this. One is

[28] F. Lobkowics, *E-706 Internal Note 004*, (1981).

[29] S. Hossain, "Hadronic Shower Simulation in E706 Calorimeter", *E-706 Internal Note 051*, (1983).

[30] Mike Glaubman, "The Liquid Argon Hadron Calorimeter", *E-706 Internal Note 063*, (1983).

[31] P. Slattery et. al., op. cit., p. 16.

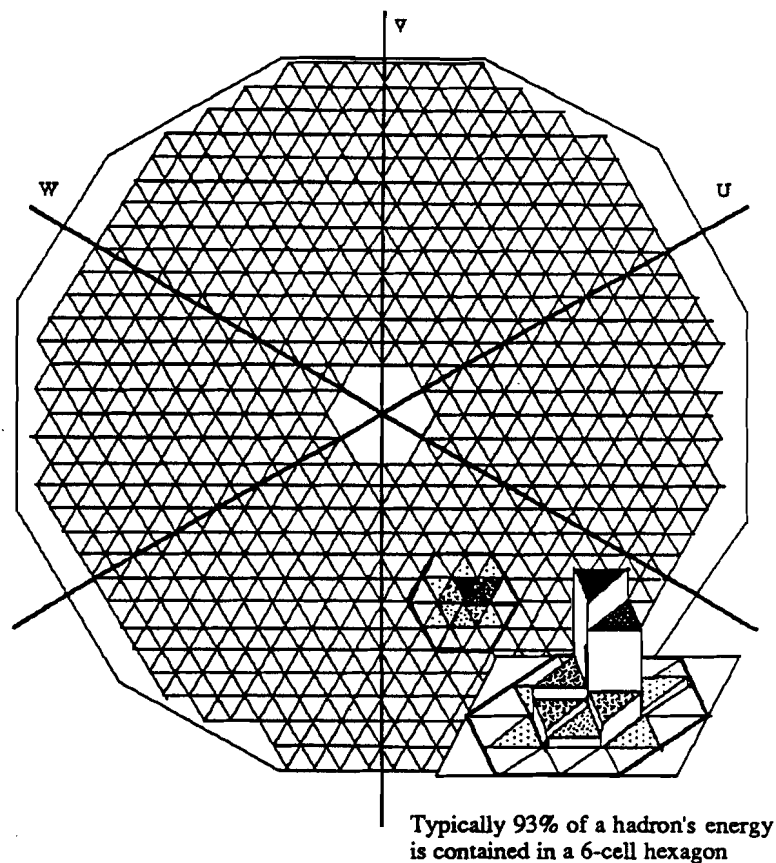


Figure 20: Drawing of HALAC Pad Configuration

that the output signals from the HALAC are much smaller than those from the EMLAC because of the larger thickness ratio of absorption material to active material used in its construction. The other is that the capacitances of the pads are a factor of 10 larger than those of the EMLAC strips. This introduces a greater level of noise in the hadronic signals.

III.4 Selection of Construction Materials

Materials selected for the construction of the LAC and to perform under cryogenic conditions. For the charge collection boards, copper clad G-10 was chosen. G-10 is an industry code name for a specific type of glass epoxy laminate. Copper clad G-10 is readily available and a

broad spectrum of methods exist for imprinting circuit patterns into the copper cladding. Normally, G-10 contains a fire retardant because of OSHA regulations governing the flammability of circuit boards. Because the impurity level in liquid argon must be kept at a minimum, a special order for G-10 without fire retardant was placed. This order included the request to use Kevlar instead of mold release to prevent the G-10 from sticking to the press. Plain G-10 was used as needed for dielectric spacers between the anodes and cathodes of the charge collection cells.

Many of the nonmetallic components used to build the LAC were tested for their potential to contaminate liquid argon. Several different glues for the cookies, various cables for the readout system, and other items were tested for their electron affinity in an ionization chamber constructed at the University of Rochester. This helped in choosing products that were least likely to cause a reduction in the amount collected charge^[32]

Structural components for the two calorimeters were constructed from type 304 stainless steel. This is a low carbon, high nickel content steel that retains its plasticity in cryogenic environments. It is difficult to accurately machine type 304 stainless into large structural components because the process of machining relieves internal stresses causing the material to warp. Normal steel is, however, unacceptable because it becomes brittle at cryogenic temperatures and is not structurally reliable. The HALAC absorber plates are made from a type 410 stainless steel, which is a high carbon content low-grade stainless. Type 410 stainless has inconsistent strength properties at cryogenic temperatures but is slightly less expensive than type 304.

The EMLAC absorber plates are made from lead, which is more of a problem at room temperature than at cryogenic temperatures. At room temperature lead is a soft malleable material which has large creep characteristics and is not suitable for structural purposes. If large lead sheets can be properly supported at room temperature then they make suitable absorbers at cryogenic temperatures where they become stiff and self supporting.

[32] Armando Lanaro, "A Liquid Argon Ionization Chamber for Testing Samples of Constituent Materials for the E706 LAC", *E-706 Internal Note 138*.

Chapter IV

Physical Construction of the LAC

The EMLAC and the HALAC are collectively referred to as the "LAC". They are sampling calorimeters which use liquid argon for the active medium and lead and steel for their respective absorbers. The LAC subtends a large portion of the event center of mass solid angle and is used to measure the energy of the scattered constituents from pion/nucleon interactions (See Chapter III).

The construction of a liquid argon calorimeter requires a balance of two conflicting principles. First, relatively fine tolerances must be maintained on the parts and assembly of the calorimeter. This is necessary to keep fluctuations in the sampling ratio at a minimum. At the same time, the assembled calorimeter must be loose enough to allow for the differential contraction of the various materials used in its construction. Otherwise, the stresses that develop during the cooldown of the calorimeter will cause internal damage that might be severe enough to impair its function. The EMLAC and the HALAC present two novel solutions to this problem.

IV.1 Physical Description of the EMLAC

The E706 electromagnetic calorimeter was built as four structurally self supporting quadrants of a cylinder of approximately 3 m diameter and 0.75 m depth. Each quadrant contains a central stack of alternating lead absorber plates and copper clad G-10 anode planes which contain the charge collection pads. On the upstream and downstream ends of this core there are additional readout boards which map the detector strips to the signal cables. Each stack is enclosed in a structural frame that allows the four quadrants to be aligned and assembled into the completed calorimeter. The calorimeter when assembled has an internal radius of 20 cm and

an external radius of 165.33 cm. It is centered on the beamline so that the first anode board is 9.0 m from the target.

IV.1.1 The EMLAC Lead Absorber Sheets

The lead absorber sheets are 2 mm thick and have the shape of a single quadrant. Lead is mechanically a soft material and because the sheets are exceptionally thin for their size, there was concern that when stood on edge at room temperature, they would creep under their own weight and eventually buckle. To prevent this an alloy of lead with superior strength properties was used. Normally "hard lead" contains antimony to give it mechanical stiffness for use in such applications as automotive batteries. The lead-antimony alloy achieves its strength through a two phase structure that consists of dendritic lead crystals surrounded by a lead antimony eutectic. Unfortunately, antimony has a high diffusivity at room temperature and so the tensile strength of the material will degrade with time. Therefore, the lead used for the absorber sheets was a lead-calcium alloy^[1] specially processed for this detector. Lead-calcium alloys form a $Pb-Sn$ solid solution with a precipitated highly dispersed Pb_3Ca phase. The tensile strength of lead-calcium alloys is comparable to that of lead-antimony alloys and calcium has a very low diffusivity at room temperature. Additionally, lead-calcium alloys have a 20% greater electrical conductivity^[2].

Due to the large size of the lead sheets their mechanical processing posed some difficulties. The ingots were cast at the lead manufacturer and then sent to a steel mill with rollers large enough to accommodate sheets of the required size. Since the lead was precipitation hardened, the plates became excessively work hardened when they were rolled to thickness, which caused them to warp. Consequently they were sent to another steel mill with machines which could

[1] The lead used contained .065% Ca and 1.3% Sn.

[2] Earle E Schumacher and G. S. Phipps, "Some Physical and Metallurgical Properties of Lead-Calcium Alloys for Storage Cell Grids and Plates", *Trans. Electrochem. Soc.*, Vol. 68 (1935), p.309-319.

stretch the sheets until they were flat. After processing the lead sheets were flat to 150 μm over a distance of 30 cm and variations in thickness were less than 75 μm .

IV.1.2 The EMLAC Charge Collection Boards

There are two types of anode boards used in this calorimeter. One has strips which measure the radial position (r -boards) of a charge shower and the other has strips which measure angular position (ϕ -boards). They are made from double sided copper clad G-10 1.59 mm thick. Both types of boards are octant shaped and have matching sets of strips on opposite sides of a board.

The r -strips are a series of concentric strips centered on the beamline. The width of the strips on any given r -board is a constant determined by the width of the strip corresponding to the inner most strip on the first r -board. The width and radial position of these strips scale according to their distance in Z from the target in proportion to the radial position and the width of the first strip on the first r -board. This results in the effect that towers of corresponding strips from all of the r -boards subtend approximately the same solid angle and focus at the target (See Fig.14).

The r -strips are numbered from 0-255 per octant, where strips 0 and 255 are the flash left at the inner and outer edges of the board after the strips have been cut into the copper. They are capable of producing a signal but are not generally used. The remaining 254 strips are 0.5456 cm wide on the first r -board. The ϕ -strips are divided into two sections by a boundary with a 40.0 cm radius at 9.0 m. This boundary forms a cone which is focused at the target 9 m from the first r -board and corresponds to an angle of 90° in the center of momentum reference frame at an incident beam energy of 530 GeV/c. The inner ϕ -strips subtend an azimuthal angle of $\pi/192$ and are numbered 1-96 per quadrant, the outer ϕ -strips subtend an angle of $\pi/384$ and are numbered 1-192 per quadrant(See Fig.21). Because of support structures the first few strips at the beginning and end of each ϕ -view do not physically exist.

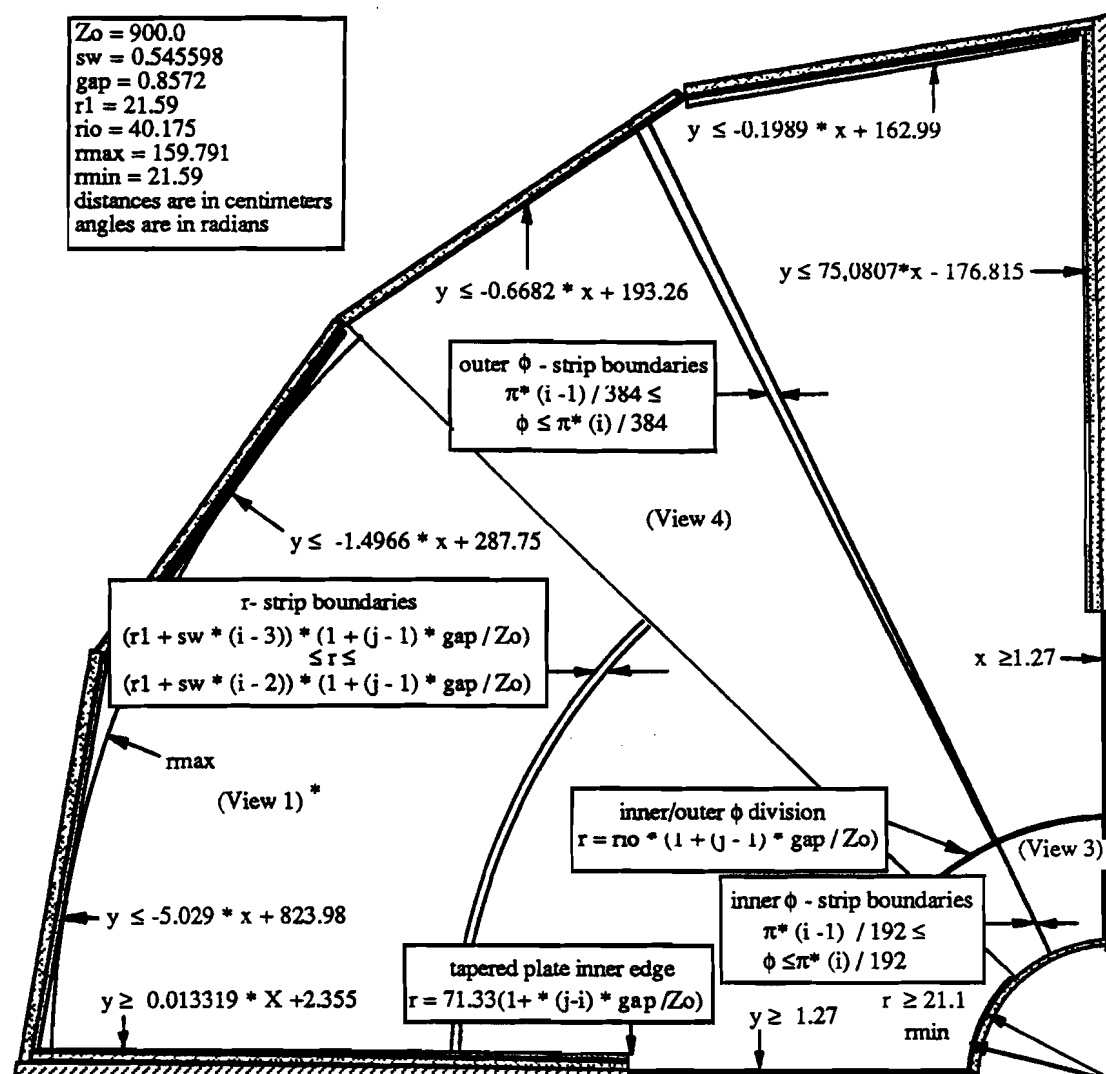


Figure 21: Drawing of the Physical Boundaries to the Sensitive Area for an EMLAC Quadrant

Because the anode boards required are large, the usual method of creating the charge collecting strips with photo-resist and acid etching would not have produced boards with the required uniform position tolerances of 0.5 mm. Therefore, a pair of computer controlled etching and milling machines were designed and built at the University of Rochester for the production of the anode boards.

These machines were built in the old Rochester cyclotron control building. Both machines had identical quadrant shaped machining tables which featured a computer controlled arm that was pivoted at the apex of the quadrant and a machine tool carriage that moved radially along the arm. With this arrangement the focused $r-\phi$ geometry of the detector could be efficiently transcribed into strips cut into blank anode boards with an accuracy of 200 μm . To produce an anode board, a blank copper clad G-10 board with predrilled alignment holes was mounted on the first machine, where a tapered circular saw 500 μm thick cut the lines defining the strips for either an r -board or a ϕ -board. The board was then moved to the second machine where three mill heads routed the outer edge of the board and drilled the holes where the binding rods were later inserted. Alignment between the 2 machines was ensured by a set of three accurately located pins set in to each table, which held a board in place by means of its alignment holes. In addition, each table was covered with a rubber mat equipped with a vacuum system that would hold the boards firmly in position (See Fig.22).

IV.1.3 The Structure of the EMLAC Central Stack

The central stack consists of 33 charge collecting cells. Each cell contains 2 lead sheets, which serve as the cathodes, that are interleaved with 2 planes of G-10 sheets, which serve as anodes. The first lead plate is followed by an r -board which is followed by the second lead plate and a ϕ -board. A set of G-10 spacers, .71 cm thick, separate pairs of anode boards along their outer edges. These spacers have slots which allow connectors to be inserted and attached to the strips. None of the spacers along the radial edges of a quadrant are identical as a result of

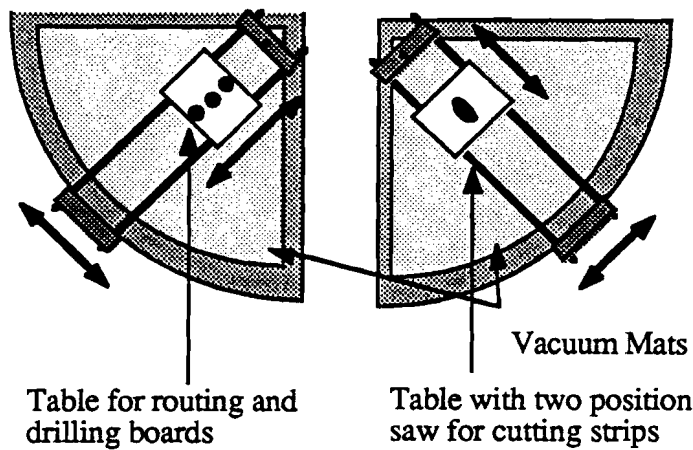


Figure 22: Layout Drawing of the EMLAC Anode Board Production Facility

the strip focusing. This led to the spacers being shaped on a computer controlled mill. The lead plates were cut to size so that they lie inside the boundary defined by the spacers and are separated from the anode boards by G-10 buttons that are inserted into a series of holes drilled into the anode boards. This creates 2.5 mm thick gaps between the lead sheets and anode boards that are eventually filled with liquid argon. All of these cells are identical except that the first cathode of the first cell is made of aluminum to reduce the amount of material in front of the stack.

Towers of strips are connected together by a 1/32 in wide braided copper wire which has connectors for each strip soldered to it. These connectors were stamped from a bronze spring metal and were electroplated with tin. The spacers have grooves cut in them through which the strings of connectors can be attached to the anode boards (See Fig.23). The strip edges on all of the anode boards were also electroplated with tin to ensure a good connection between the connectors and the strips.

At both ends of the detector stack there is a set of 3 pairs of G-10 boards to which the signal cables for the detector attach. The connector strings attach to channels cut on one side of

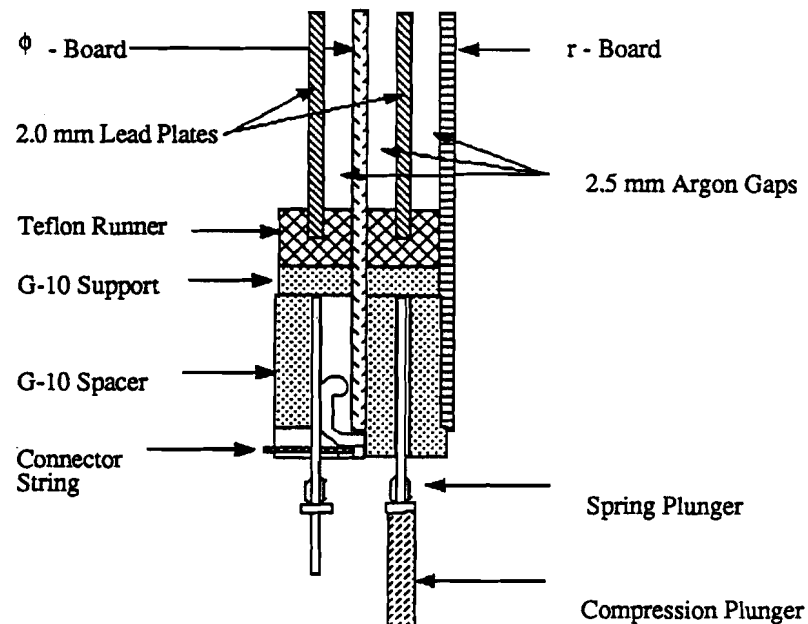


Figure 23: Cross Section Drawing of an EMLAC Cell at the Outer Edge of the Calorimeter.

the board. These channels conduct the signals to the outer edge of the detector where the signal cables are attached and were designed to take into account the effects of strip focusing (See Fig.24). Each board was made with channels on only one side so that the opposite side could be grounded to isolate the signals on one board from those on adjacent boards. Also, the copper cladding on the ground side of these boards was stripped from the areas where the connector strings attach to avoid grounding the signals and the channel edges were tinned to ensure good contact with the connector strings. There are 2 sets of readout boards so that signals from the first 11 cells could be read out separately from those of the last 22 cells. This division is adhered to for all but r-strips 1, 2, and 239-254. Because of the strip focusing, r-strips 1 and 2 do not extend through the front portion of the detector and are therefore read out only through the back readout boards with all cells being ganged together. Likewise, r-strips 239-254 drop off the

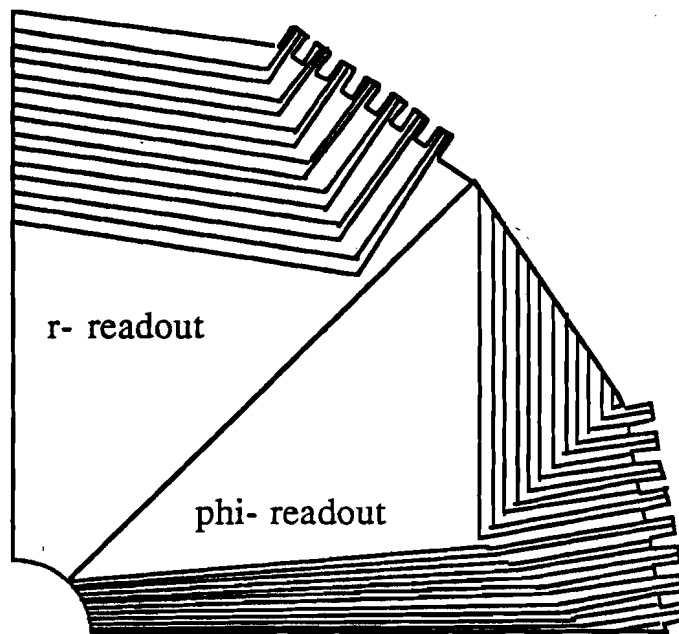


Figure 24: Examples of EMLAC readout boards

outer edge of the detector before they reach the back and are thus only read out through the front read out boards (See Fig.14).

IV.1.4 The Structure of an EMLAC Quadrant

The detector stack is embedded in a quadrant frame between two 3.7 cm thick G-10 plates placed at the ends of the stack. Seven steel plates, made from 304 stainless steel, join them together. Two of these plates are 3 mm thick and are attached to the horizontal and vertical edges of the G-10 plates extending from the inner edge of the G-10 plates to a radius of 90 cm. Two more stainless plates attached to these sides extend from this point to the outer edge of the G-10 plates. These plates taper in thickness from 1.5 cm to 4.0 cm to minimize the amount of dead space. The boundary between these plates has an angle that focuses back at the target so that it does not cross any of the r-strip boundaries. The last two stainless plates are 3.7 cm thick and attach to the G-10 end plates at two nonadjacent positions on the outer edge of the

G-10 end plates. All of the steel plates are covered on the inside of the quadrant with a layer of G-10 to prevent electrical contact with the connector strings embedded in the spacers (See Fig.25).

The detector stack is bound to the quadrant frame by a set of epoxy coated stainless steel rods that pierce the anode boards and spacers around the perimeter of the quadrant. The epoxy coating prevents any of the strips which they penetrate from being inadvertently grounded. These rods bind the detector stack to the front end plate. Since the rods pierce the anode boards and the spacers perpendicular to the weave of the G-10, bellville washers are used to maintain the tension in the rod after cooldown. This is because in the direction perpendicular to the fiberglass weave the amount of thermal contraction for G-10 is larger than that for stainless steel. This structure is self supporting so that quadrants can be built and transported individually and then assembled at a later time. Table 4 contains a list of the thermal contractions for G-10^[3], lead^[4], aluminum^[5], copper^[6], stainless steel^{[7][8]}, and teflon^[9].

A problem encountered in building a liquid argon calorimeter is designing the detector to withstand the trials of a cryogenic environment. For example, a problem with using lead for the absorber plates is that lead is a structurally soft malleable material that has a large coefficient of thermal expansion. This makes it difficult to construct a support structure that will hold the lead sheets in position but not damage them. The sheets in this detector are cradled inside the

[3] M. B. Kasen et al., "Mechanical, Electrical, and Thermal Characterization of G-10CR and G-11CR Glass-Cloth/Epoxy Laminates Between Room Temperature and 4 K" *Advances in Cryogenic Engineering Materials* (New York: Plenum Press, 1980), p.241.

[4] Y. S. Touloukian and C. Y. Ho eds., "Thermal Expansion of Metallic Elements and Alloys", *Thermophysical Properties of Matter, The TPRC Data Series*, Vol. 12, p. 178, Plenum Pub., New York, (1975).

[5] *ibid*, p.2..

[6] *ibid*, p.77..

[7] Advanced Research Projects Agency and the Cryogenics Division of the National Bureau of Standards, " Mechanical, Thermal, Electrical and Magnetic Properties of Structural Materials", *Handbook on Materials for Superconducting Machinery*, p. 8.1.3-6.1(11/76), (1974).

[8] *ibid*, p. 8.1.10-5(11/76).

[9] Y. S. Touloukian and C. Y. Ho eds., "Thermal Expansion of Nonmetallic Materials", *Thermophysical Properties of Matter, The TPRC Data Series*, Vol. 13, p. 1443, Plenum Pub., New York, (1975).

Material	Thermal contraction
	$\frac{\Delta L}{L \times 10^{-6}}$
G-10CR warp & fill	-2300
G-10CR normal	-7000
Lead	-5300
Aluminum	-3700
Copper	-2800
304 Stainless steel	-2500
410 Stainless steel	-1500
Teflon	-15000

Table 4: Thermal Contraction of EMLAC Construction Materials between 300 K and 88 K

G-10 spacers and between the G-10 buttons attached to the anode boards but are not physically fastened to the detector. This provides support for the sheets, maintains the proper spacing between them and the anode boards, and allows them to contract under cryogenic conditions without causing excessive stress in the sheets as might happen if they were fixed in position.

Solving this problem creates another. The coefficient of thermal expansion of lead is greater than that of G-10, and since the lead sheets are free to float inside the detector, there is nothing to keep them from shrinking and uncovering sensitive areas of the detector, leaving those areas inactive. This is a problem especially in the bottom two quadrants as the area uncovered is in the most active region of the detector, i.e. near the inner radius of the quadrant. To prevent this from happening a series of spring driven plungers were installed to support the lead. The springs were loaded into compression tubes that slide into restraining slots in the outer steel support plates of the quadrant frames. There the springs push on the plungers that were placed in holes drilled into the outer spacers. Since the plungers used to support the lead sheets necessarily had small cross sections in order to fit through the holes in the spacers, they create local regions of high stress at their points of contact. This potentially could have caused the lead to deform and become grounded to the anode boards. To prevent this, small bars of G-10 were placed

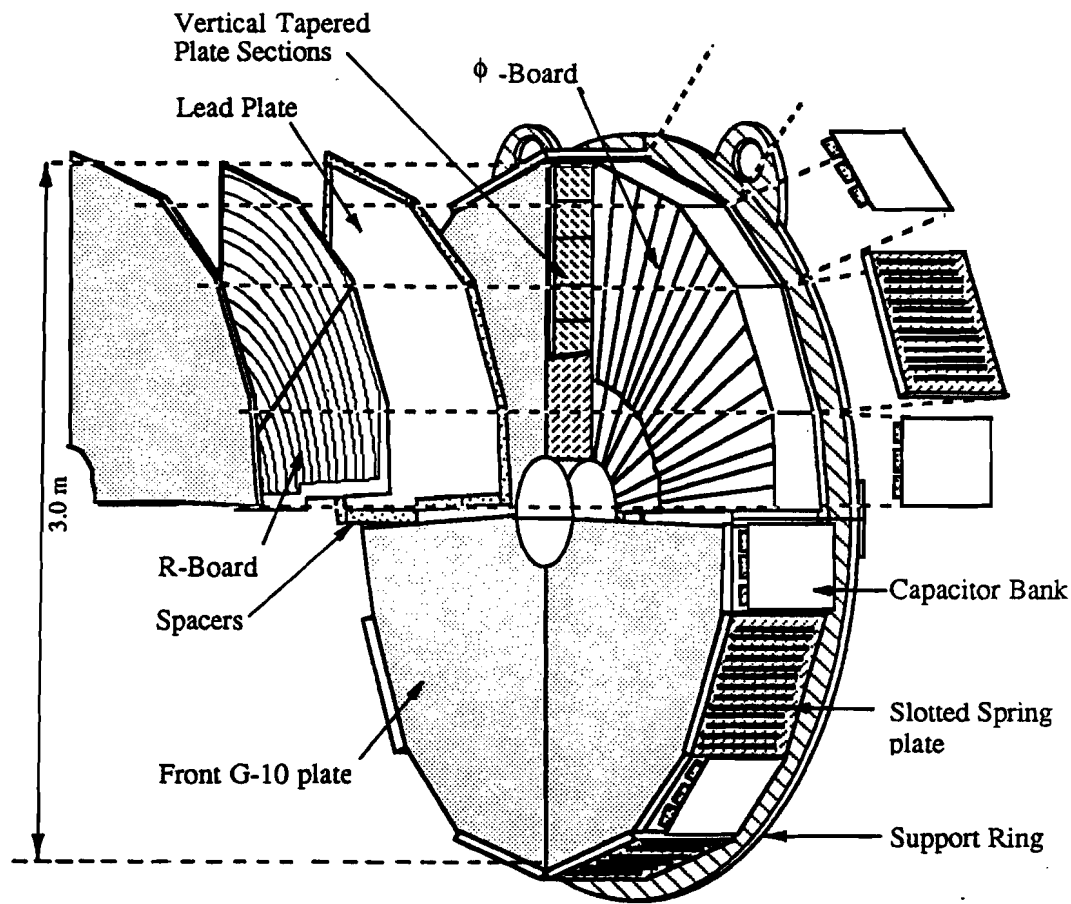


Figure 25: Isometric Drawing of the EMLAC with an Exploded View of One Quadrant

between the lead and the plungers to provide a stiff surface for the plungers to act against (See Fig.24). Runners of Teflon were placed on the edges of the lead sheets so that as the lead sheets expanded and contracted they would not snag on the rough G-10 spacers and become cocked out of position. This elaborate system allows the lead to contract and expand without undue stress yet maintains the position of the sheets so that active regions of the detector are not uncovered.

Each quadrant was assembled in a rotating jig with removable support arms (See Fig.26). The individual planes of anode boards and lead sheets were stacked one at a time into the quadrant frame which was held in the jig at an angle 5° from vertical. Assembling the quadrants

at this small incline allowed each plane to be placed in a stable free standing position and avoided the high stresses on the lead plates that would have been encountered from assembling the quadrant in a horizontal position. The width around the perimeter was checked after the assemble of each third of each quadrant and adjusted using mylar shims inserted between the spacers and the anode boards. All of the EMLAC pieces were degreased with Freon 12 in a vapor degreaser and rinsed with alcohol except for the anode boards. Each piece was assembled by hand except for the lead plates. These were positioned with a vacuum lifter that had tilt and rotational degrees of freedom. Once the stack and frame were completed, the connector strings were installed by rotating the jig and removing the support arms and the stainless steel plates one section at a time.

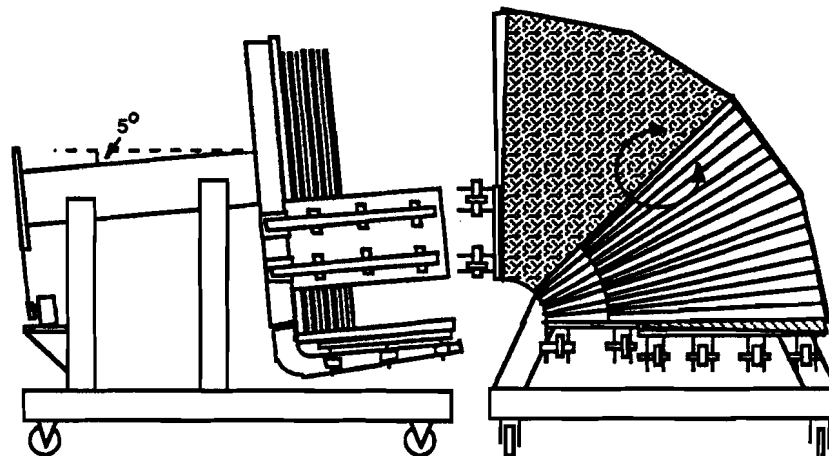


Figure 26: Drawing of the Assembly Jig Used for Assembling the EMLAC Quadrants

All four quadrants were suspended in a pair of stainless steel support rings 2.5 cm thick and 15 cm wide. Each ring was made in four sections so that one section from each ring was attached to a quadrant after its assembly. Then, as the quadrants were assembled together the sections of the rings were joined. Each ring section was attached to a quadrant by two

stainless steel bars that were bolted to the slotted stainless steel plates built into the quadrant frame. Between the bars and the slotted plates a set of bellville washers were placed at each bolt point so that when the ring contracts relative to the quadrants under cryogenic conditions the bellville washers would compress and the rings would not become overstressed. From Fig.27 one can see that the detector(A) can float relative to the support ring(B) on the bellville washers which allow for relative expansion and contraction of the two as the environment changes. The shoulder bolts screw into the detector through oversized holes in the ring. This prevents any lateral movement of the ring but not the vertical motion.

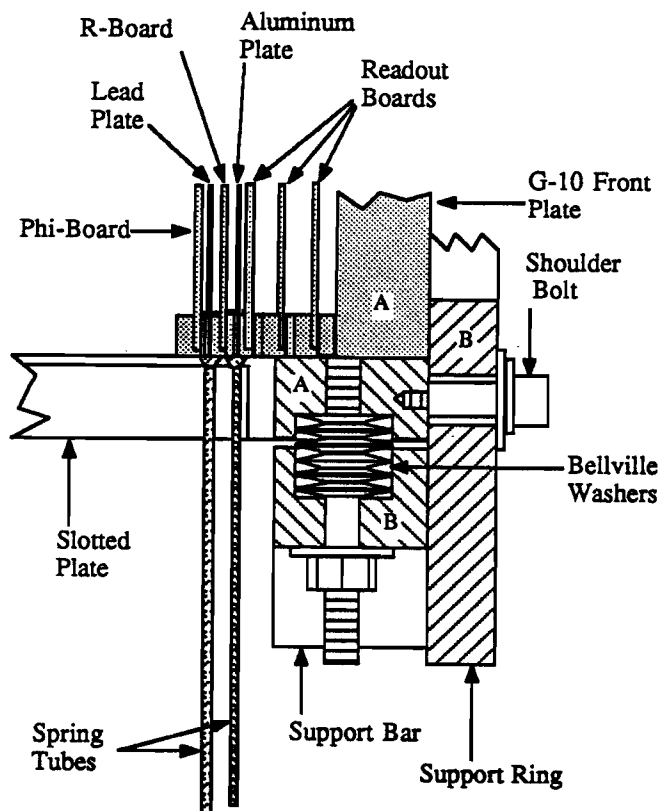


Figure 27: Cross Section Drawing of the EMLAC Quadrant Support

After the assembly of each quadrant was completed, it was lifted from the jig, the support ring sections were attached, and it was stored on a steel pallet for later transport to the experimental hall where the final detector assembly occurred.

IV.1.5 The Final Assembly of the EMLAC

The quadrants, once assembled, were joined together in pairs. The two top and two bottom quadrants were joined by the tapered steel plates that they share. The vertical tapered plates were in fact cut into five sections each. Two of these sections were installed into one quadrant and the other three sections were built into the mating quadrant. This allowed the two quadrants to be self-supporting during assembly and transport, then mated together during the final assembly. The top two quadrants were then placed on top of the bottom two but were not physically bound together. The four sections in each ring were tied together using 2.5 cm stainless steel patch plates and high strength bolts made from Inconel 718. Once assembled, the detector was jacked into position. The rings were then pinned into the clevises at the ends of the support rods which hung from the top of the gantry.

Before the dewar was raised into position, 3.2 mm copper plates were attached to the front and back of the calorimeter along with copper fins, which extended below the EMLAC. The theory was that, as argon began to condense and pool at the bottom of the dewar, the copper would conduct the latent heat of the detector away through the fins and thus shorten the time needed to cool the calorimeter. Resistive heaters were attached to the fins to provide the reverse function should it be necessary to open the dewar for repairs to the calorimeters. At this time the electronics cables, the high voltage capacitor banks and the thermocouple monitors were attached and the spring tubes and pistons for the lead plates were installed.

IV.2 The Physical Construction of the HALAC

The Hadron calorimeter is a liquid argon and steel sampling calorimeter. It has 53 cells,

each consisting of a sampling plane with dual anode planes and a 2.5 cm steel plate. The calorimeter is separated into front and back sections. The front section contains the first 14 planes and associated steel plates. The back section has the remaining 39 planes and 38 steel plates.

IV.2.1 Description and Assembly of the Cookies

The detector planes, called "cookies", are laminates of 4 layers of 0.8 mm single and double copper clad G-10 interleaved with strips of 3.2 mm G-10 (See Fig.28). Each layer is made from three to four 3.65×1.22 m G-10 sheets. The outer two layers serve as the high voltage planes. They are made from double sided copper clad G-10 so that the internal stress induced by the difference in thermal contraction between copper and G-10 is balanced. Without the support of G-10 strips on both sides they would tend to curl and peel away from the cookies if they had been made from single sided G-10. They are spaced from the inner two layers, "anode boards", by horizontal G-10 strips. The two anode planes are made from single sided G-10 and are glued together with vertical G-10 ribs between them. Only the side of the high voltage plane facing the anode pads is connected to high voltage the other side is grounded. The cookies have hexagonal central holes that increase in height from 21.6 cm to 27.3 cm. The outer perimeters are octagons 3.8 m high.

The anode boards are tessellated with equilateral triangles, which serve as charge collection pads. The charge collection pads were etched on the G-10 anode plane in rows with their readout lines between the rows, creating regions in a plane where charge is not collected. To compensate for this the two anode planes have conjugate sets of pads so that when an area in one plane has no charge collection the same area in the conjugate plane does, providing uniform coverage of the solid angle subtended by the calorimeter. The readout lines on each anode board are

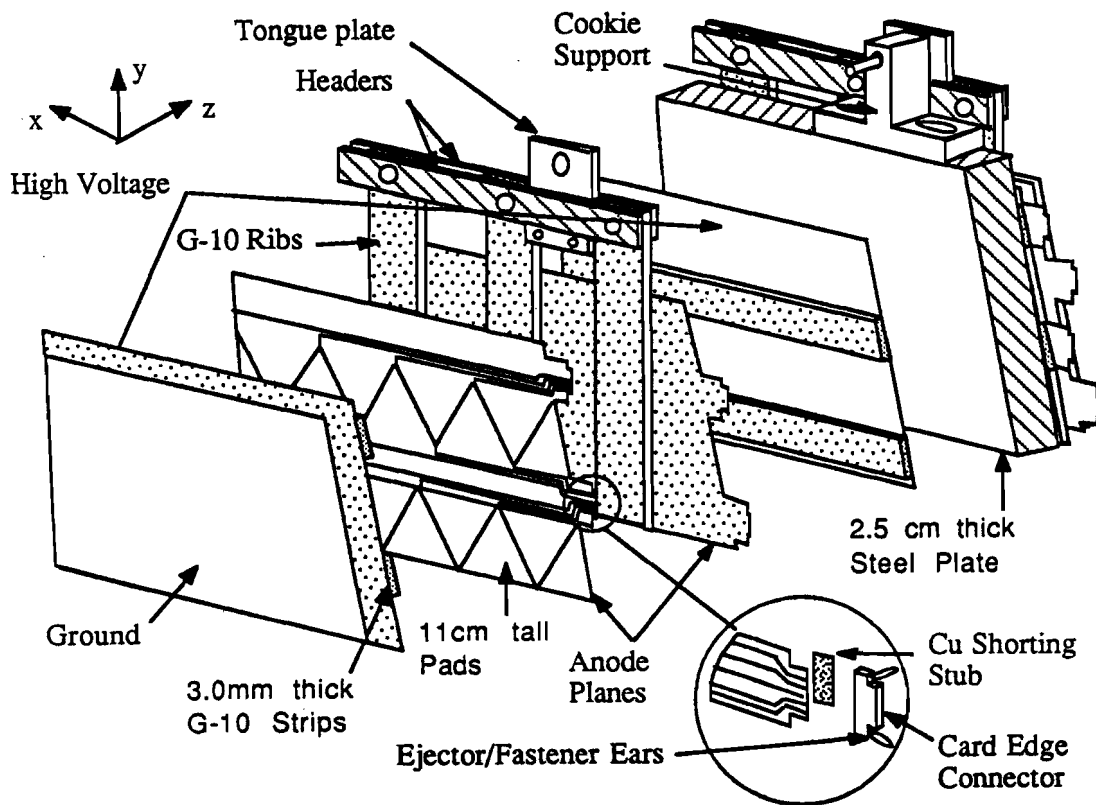


Figure 28: Exploded View of a HALAC Cell

covered by the G-10 strips when a cookie is assembled so extraneous charge is not collected by the lines causing unwanted signal communication between pads.

IV.2.2 Cookie Anode and Cathode Board Preparation

The readout and high voltage boards were prepared on a 16×5 ft GerberTM plotter. The Gerber plotter is a high speed machine normally used for the production of drawings from computer aided design programs. For the purposes of E706 the plotter head was replaced by a high speed (20-60 krpm) routing head using 3.2 mm diameter drill bits and 0.8-1.0 mm diameter router bits to produce the alignment holes and circuit patterns for each set of boards.

The boards for the high voltage layers were machined on the Gerber as follows. The first step was to rout a 12.7 mm wide strip through the copper along the contour of the board. This

gap prevents the high voltage from arcing to the ground side of the board. The second step was to drill two or four locating holes and to cut the board to shape around the outer contour of the routing.

The first step in producing an anode board was to rout a 6.4 mm gap around the contour. This produced a cleaner edge once the board was cut out. The next step was to rout the pad pattern on the board. The last step was to drill the locating holes, the holes for mounting the ejector/fastener ears, and the rivet holes for the shorting stubs.

The card edge connections that were milled into the anode boards, which are 0.8 mm thick, were too thin to be used with standard connectors that require 1.6 mm thick boards. This problem was solved by using 0.8 mm thick copper shorting stubs that were punched to size (See Fig.28). These stubs made the board thick enough to use the card edge connectors and grounded all of the unused connections on the connector together. The stubs were plated with 0.25 μm of gold over 3.8 μm of nickel and were attached to the anode boards with gold plated brass eyelets. The pad and high voltage boards were then cleaned using a pneumatic sander with a plastic scouring pad and water to remove rough edges and corosions and then rinsed was ethyl alcohol.

IV.2.3 Description of the Cookie G-10 Strips and Ribs

Sheets of G-10 3.2 mm thick were cut into one inch ribs and varying width strips by a diamond saw. The ribs were cut to 3.6 m lengths and had a 3.2 mm diameter hole drilled in them at the top. At both ends of the strips and the bottom of the ribs a V-notch was cut for locating them during the assembly of a cookie. The strips determine the argon gap thickness between the anodes and cathodes.

IV.2.4 Composition and Application of the Cookie Glue

To glue the cookies together a two component epoxy was used. The epoxy resin DER332

and catalyst V40 (equivalent to V140) were mixed in a 1:1 ratio with two additives. The first additive, glass beads with a size of 200-230 standard mesh sieve and mixed 250 grams per liter, determined the minimum gap between glued parts and enhanced control over the spread of a bead of epoxy. The second additive was Cab-O-SilTM or fused silica. This is a thixotropic agent used widely in industry in epoxies and milk shakes. It was mixed in at the ratio of 50 grams per liter.

The epoxy was dispensed on the G-10 strips and ribs by an automatic device. This machine had a linear drive track for moving a strip or rib of G-10 horizontally as it dispensed a constant volume of epoxy per unit length. The epoxy components were stored in separate pressure vessels which were fitted with agitators to mix and keep in suspension the additives to the epoxy. The vessels were agitated and evacuated for 16 hours prior to gluing to promote outgassing of the epoxy so that it would not later contaminate the argon.

IV.2.5 Assembly of a Cookie

The cookies were assembled on a massive cast iron bedplate which had an aluminum plate (Mother plate) in the shape of a cookie bolted to it. The bedplate was used to provide a stable flat surface for the assembly of the cookies. The bedplate had holes for locating pins to locate the planes relative to each other. Attached to the bedplate at the sides of the Mother plate were rules with "arrows" clamped to them. The arrows on the bedplate were set to the required position for a particular set of strips. The arrows would then fit into the V-notches at the ends of the strips and ribs to locate them. With this arrangement the cookie could be built up a layer at a time using the glue machine to apply epoxy to the strips and ribs, using the arrows to place them in their correct position.

After assembly was complete a plate similar to the Mother plate and suspended from above was brought into place. This plate, called the "Father plate", was suspended from a rolling frame that would bolt to the bedplate. Airbags between the Father plate and the rolling frame

were inflated to 7 psi while the epoxy set to press the cookie flat so that the epoxy beads spread evenly giving the cookie a uniform thickness. The reason for the bedplate being so massive was to prevent the cookie from warping while the epoxy cured. After the epoxy cured the cookies were placed in plastic storage bags and hung in a closet which was maintained with a gaseous nitrogen atmosphere to prevent corrosion of the copper.

IV.2.6 Description of the Cookie Support System

At each end of a cookie a plate (Tongue plate) is placed in a gap between two ribs. These are held in place between two 3.2×20.1 mm aluminum plates (Headers) which are fastened to the cookie by cotter pins through the holes in the ribs (See Fig.28). The Tongue plates have holes to suspend the cookies by 12.7 mm diameter steel rods. The steel rods are attached to aluminum T pieces that are designed to mount one cookie on each side of a steel plate so that every other steel plate supports two cookies. This alleviates the problems of mounting the cookies at the ends of the calorimeter and on the super plates. The T pieces are slotted to permit horizontal adjustment. Vertical adjustment is done using the mounting screws and nuts under the T piece. Adjustment in Z is done by moving the Tongue plate on the steel pins.

IV.2.7 Description of the HALAC Steel Structure

The HALAC support structure was made from type 304 stainless steel. Two absorber plates (super plates), two bottom I-beams, and two frame rails form a rigid structure around which the rest of the HALAC is built (See Fig.29). The two I-beams are 2.7 m long, 0.3 m high and are bolted to the super plates. The fifty other absorber plates (Zorba plates) sit vertically on top of the I-Beams. They are spaced 2.4 cm apart by horse shoe shaped parts which fit over the top of the I-beams. Every second Zorba plate supports a pair of cookies. Clevises join the super plates to the support rods which are suspended from the gantry. The support rods are made of two pieces joined by a coupling. The entire structure weighs 181 metric tons.

The HALAC is hung from the gantry by 11.4 cm diameter rods which thread into the top of the clevises. The rods are made in two pieces that are joined by couplings just above the baffling in the dewar top hat. The clevises were each surveyed into position based on a calculation of deflection of the gantry and thermal contraction of the calorimeter to achieve a nominal beam height. Each clevis is attached to a super plate with thirteen 2.5 cm diameter stainless steel pins.

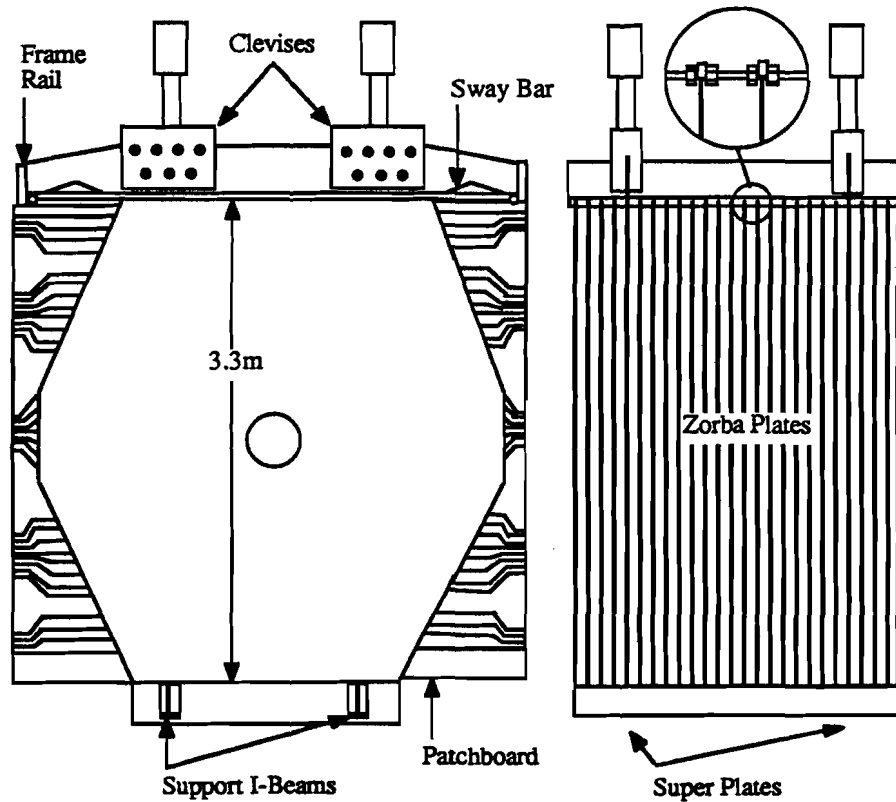


Figure 29: Drawing of the HALAC Steel Structure

IV.2.8 The HALAC Steel Absorber Plates

The fifty Zorba plates are made of 410 stainless steel. Since an Zorba plate has to support only its own weight and the weight of two cookies, a small cost savings was realized by using

type 410 stainless. The absorber plates were plasma cut in the shape of an octagon, like the cookies. The original design of the HALAC specified seventy two 1.9 cm thick steel plates with beam holes of a radius equal to twice the height of a triangle at the position in Z measured relative to the target. When the detector was redesigned to use fifty two steel plates 2.5 cm thick, the hole specifications were not changed. With the first fifty two hole diameters placed at larger values of Z, a substantial dead region between the coverage of the hadron calorimeter and the forward calorimeter was created by the smaller solid angle subtended by the holes.

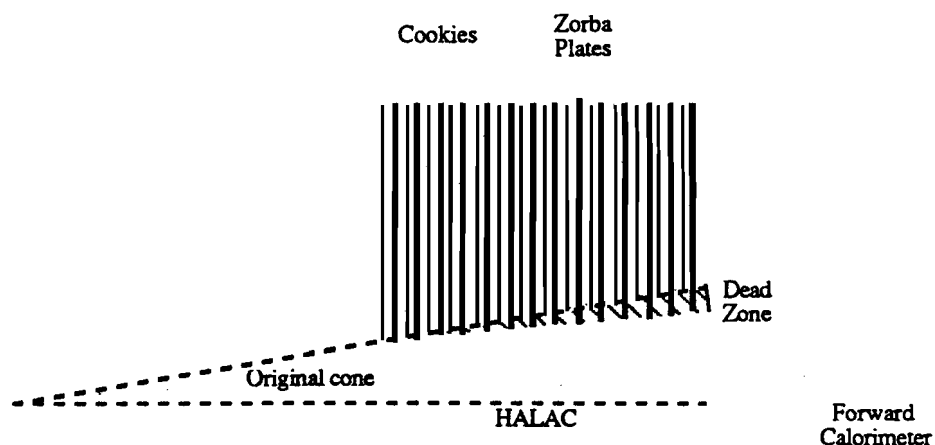


Figure 30: Illustration of the Dead Zone Created by the HALAC

Steel plate is generally accompanied by a certain amount of scale and oil that must be removed before the steel can be used in a liquid argon calorimeter. Each plate was examined for gross defects and initially cleaned with a coarse scouring pad and acetone. Sandpaper was used along the edges and around holes to remove any burrs that might damage cookies. Scale and oil were removed from each plate using a pneumatic sander with scouring pads and a soap solution. The soap, which was purchased from VWR Scientific, was selected for its ease of rinsing. After both sides of each plate were cleaned, it was put into a vertical position in a rack where a 15 Molar solution of oxalic acid was used to remove any oxides left on the plate. The plate was then

rinsed with distilled water and scrubbed with scouring pads as necessary. The final cleaning was done with 200 proof Ethyl Alcohol.

At one point both a steel absorber plate and a cookie were tested under cryogenic conditions for structural integrity and also for electrical continuity in the case of the cookie pads. They were cooled to liquid nitrogen temperatures in an insulated bath and then immersed in liquid nitrogen. Each time the process was monitored by an array of thermocouples attached to the steel plate or cookie. The results of both tests were within acceptable limits^[10].

IV.2.9 Installation of Sway Bars

The final work done on a steel plate before lifting it into place was the installation of the sway bars. They mate with the steel plates in four machined spots to ensure accurate location in the vertical direction. Threaded lifting eyes went through the sway bar, through accurately machined spacers, and into barrel nuts in the steel.

The tilting of the absorber plates is prevented by the sway bars. These bars are 2.5×5.0 cm and extend like arms to the top frame rails attached to the top of the super plates (See Fig.29). Along the inside of the frame rails are two 1.9 cm diameter threaded stainless steel rods. At each end of a sway bar there are two semicircular indentations which fit over these rods. The bars were then held in position by the two nuts on each rod. The first and major function of the sway bars was to support the Zorba plates at the top so that the stack would not topple forward or backward. The second function was to provide some stiffness and straighten the warpage of the plates.

IV.2.10 The HALAC Copper Fins

Holes were drilled in the bottom of the plates for the attachment of copper fins, whose

[10] C. Lirakis, G. Fanourakis, "Cryogenic Tests of the Hadron Calorimeter", *E-706 Internal Note 150*, (1986).

purpose is to aid in removal of heat from the steel. The steel was lifted high enough off the ground to install the fins with four nuts, bolts, and belville washers. A steel bar 0.6 cm thick by 5.0 cm high with a length equal to the spacing between the I-beams was attached to the bottom of the steel plates. These bars extended down between the I-beams to prevent the steel from walking off the sides of the I-beams. Heaters were installed on several fins to aid in outgassing during the evacuation of the dewar and in warming the detector after it has been cooled down.

IV.2.11 The Installation of the Cookies

The cookies were taken one at a time from their storage bags and placed on a specially manufactured table. This table brought the cookie from a vertical to horizontal position to prevent unnecessary stress from being applied to the glue joints of the cookies. When the cookie was in the horizontal position the ejector/fastener ears were installed at each card edge connection. These were installed to ensure the cables had good mechanical support. A last minute electrical check of high voltage wiring was done. Mylar was installed to electrically isolate the cookie from the steel/gantry. The cookie was brought again into an upright position and a 4.9 cm thick spacer was placed next to the cookie and a second cookie was placed next to it. The horizontal procedure was repeated for the second cookie and then the high voltage wires were installed. Finally the cookie support was tied to a spreader bar and the assembly was tilted to a vertical position. The cookie pair and spreader were then lifted with the overhead crane and placed in the calorimeter. There were two possible support locations on the left and right sides of a Zorba plate for the cookie supports to be mounted. The locations of the cookie supports were staggered so pairs of cookies would not interfere with each other.

IV.2.12 The Alignment of the HALAC

A proper height for the cookies was determined by surveying the tops of the sway bars. Shims were installed to bring the support system to this nominal value. After the cookies were

installed, they were surveyed using the assembly locating pin holes. Measurements were made from both sides of the cookie for the final position adjustments. The X position was adjusted by moving the support system in the X direction. These values were minimized for the pair of cookies. If the pair were skew relative to each other, little could be done to correct the situation. The position in Y was adjusted by installing shims between the Header and the support.

IV.2.13 Patchboard Installation and Cabling the HALAC

The Hadron calorimeter uses mass terminated card edge connectors on a ribbon cable to daisy chains the towers of pads together in groups. The groups correspond to the rows of the cookies. The chain is then terminated on the patch board. The patchboard configures the output to match the readout cables. This configuration ordered the signals so that "up" and "down" pads read out consecutively. At the card edge connector, the pads are read out starting from the center pin which is a dummy. All "up" pads are read out starting from the center and moving up on a board. All "down" pads are read out starting from the center and moving down (See Fig.28). The patchboards are suspended at the front and back ends of the calorimeter from the top frame rails and fixed at the bottom to the support I-beams (See Fig.29).

IV.3 The Physical Construction of LAC Gantry

The EMLAC and the HALAC are suspended by four stainless steel rods each from a gantry. These rods are equipped with strain gauges to monitor the load distribution of the detectors (See Fig.31). The gantry is a steel I-beam frame which contains the cap for the dewar that encloses calorimeters.

The gantry is mounted on a set of Hillman rollers so that it can be moved transversely to the direction of the beam by a pair of power screws mounted to the floor. This allows the entire detector to be exposed to the beam by using the calibration magnet to provide vertical motion of the beam. In this manner all of the detector channels can be calibrated. Furthermore, because

the detectors are suspended from the gantry, it is not possible to lower them into the dewar. Instead, when the building enclosing the spectrometer was constructed, a pit large enough to contain the dewar was built into the foundation next to the beamline. By moving the gantry over the pit the dewar can be raised and lowered around the calorimeters by a set of four power screws attached to the top of the gantry.

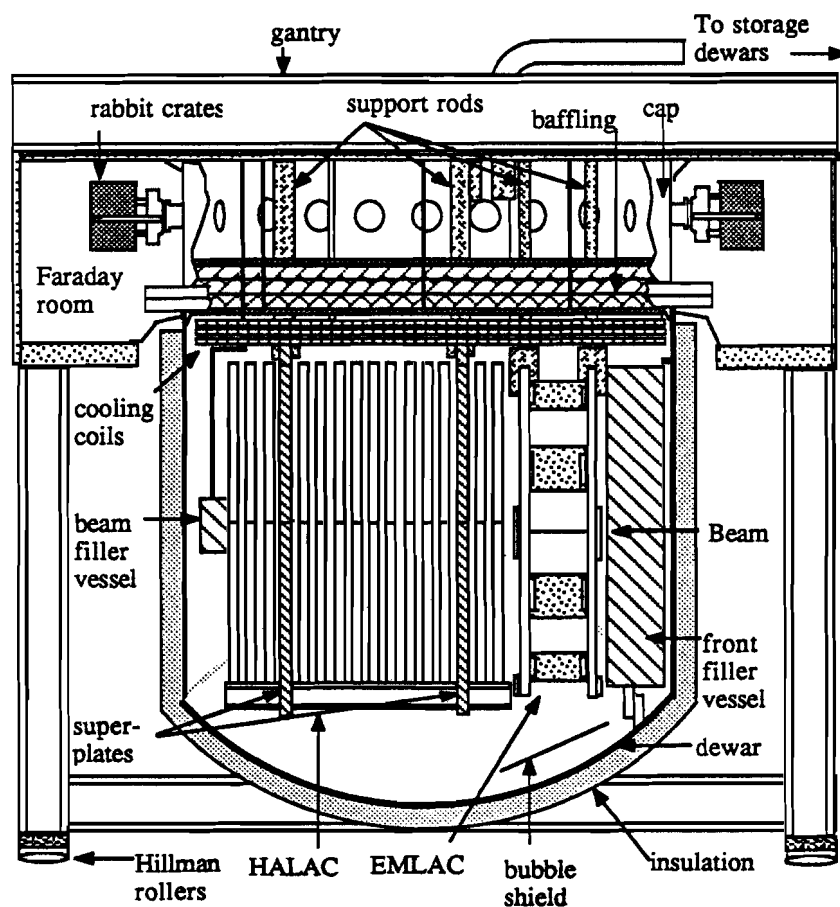


Figure 31: Cut View of the LAC Gantry.

Attached to the cap is the cryogenic piping used to supply and control the flow of liquid nitrogen to the cooling coils which are hung from the cap just above the calorimeters. Since the cap is made of carbon steel, plastic baffling was placed above the cooling coils to prevent thermal convection from cooling the cap. This was necessary because if carbon steel is cooled below a critical temperature it becomes brittle and is very likely to fracture under load. Both of the calorimeters and the cap are instrumented with copper/constantan thermocouples so that their temperature profiles could be monitored for abnormal situations. The thermocouples and the strain gauges are monitored by an IBM PC located on top of the gantry. The PC is connected to the cryogenic alarm system.

The dewar which encloses the calorimeters is made of 1.6 cm rolled stainless steel plate and is 5.2 m in diameter. It is covered with insulation instead of having a vacuum jacket. This reduced the amount of material between the detectors and the target by eliminating the second wall required by a vacuum jacket and realized a substantial cost savings. The insulation was constructed of a 4 cm thick fiberglass blanket covered by chicken wire and five layers of 4 cm thick polyurethane foam alternating with four layers of fiberglass cloth. The exterior of the foam is covered by a 0.8 mm thick sheet of butyl rubber and a 0.3 cm thick layer of StaytexTM, a fire retardant^[11]. The insulation is equipped with a system of plastic tubes that supply nitrogen gas to continuously purge the insulation of water which might condense on the dewar and destroy the insulation.

The dewar has a 5 cm diameter port on the upstream face of the dewar made with 1.6 mm stainless steel for the beam to pass through. This reduces the amount of material in the path of the beam and consequently the background noise in the calorimeters created by beam scattering. Inside the dewar along with the two calorimeters are two low density volumes to displace the liquid argon. One is attached to the wall of the dewar in front of the EMLAC to reduce the number of radiation lengths of material in front of the detectors and is referred to as the "front

^[11] Chicago Bridge and Iron Co., *Dewar Insulation Note*, Ref No.851553.

filler vessel". The other is a tapered cylindrical volume inserted into the beam holes of the calorimeters referred to as the "beam filler vessel".

The purpose of the front filler vessel is to reduce the energy smearing of incoming particles that would result from their scattering in the liquid argon. It was constructed of a cryogenic closed cell foam (RohacellTM71) produced by Cryo Industries. The foam has a density of 0.070 g/cm³. The foam was covered with a layer of epoxy/fiberglass and enclosed in a 3.2 mm stainless steel skin to give it some structural rigidity to withstand the approximately 15,000 lbs of buoyancy force created by its immersion into the liquid argon. The skin also impedes the path of any potential outgassing of the foam that might contaminate the argon.

The beam filler vessel serves the same purpose as the dewar beam window. By reducing the amount of material in the path of the beam the detector noise from beam scattering is lowered. This vessel is a hollow conical shell made of 3.2 mm stainless steel sheet. It is supported at both ends by heavy stainless steel rings that rest on two of the HALAC absorber plates. Since the vessel is hollow, it has to be pressurized by helium when there is liquid argon in the dewar to prevent it being crushed by the hydrostatic pressure generated by the argon.

All of the electronics crates containing the charge amplifiers are attached directly to the dewar cap. The signals from the calorimeter pass through a set of thirty two feed-through parts to the crates. Since these amplifiers are very sensitive to external noise, a Faraday room was built into the top of the gantry to shield them from electronic noise.

Chapter V

The LAC Electronics System

This chapter describes the LAC electronics system beginning with the LAC itself and working out through the amplifiers to the data acquisition computers.

V.1 The LAC High Voltage System

To make the LAC work it is necessary to create a high intensity electric field to force the ionized electrons to drift to the charge collection strips. To create this field in the EMLAC a negative high voltage is attached to the lead plates and the collection strips are grounded through the amplifier cards. The electrons will drift to these strips since they are at a voltage that is positive with respect to the lead plates. In the HALAC the voltage is connected to the G-10 high voltage plane and the triangular pads are grounded through the amplifiers.

With the lead plates cradled inside sets of G-10 spacers it was necessary to use a fine gauge wire with small diameter insulation. The insulation could not crack or deteriorate under cryogenic conditions. These are rather stringent demands to place on high voltage cable which is normally made of moderate gauge wire to reduce the field intensity and prevent breakdown of the insulation. The insulation is usually large in diameter and made from butyl rubber or a plastic, neither of which is useful in a cryogenic environment. A 1/32 in cable with teflon insulation manufactured by W. L. Gore Co. was found to be adequate for use in the LAC high voltage system.

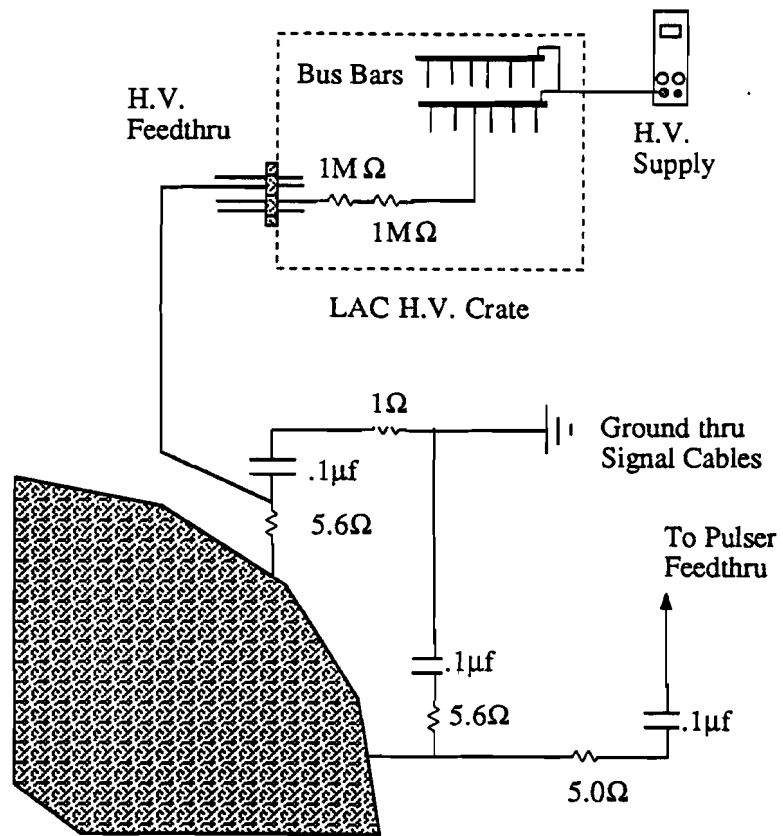
When a shower occurs within the calorimeter it can locally generate a picocoulomb of charge or more in a single argon gap. This charge produces a redistribution of the surface charge on the electrodes in order to satisfy Maxwell's equations. The redistribution of charge is also known as "image charge". The drift of electrons toward the anodes produces changes in the image charge that result in a signal with a polarity opposite that of the signal produced by the electrons. If

the cathode is forced to draw charge from a remote voltage supply then a depletion of the cathode surface charge in the area surrounding the injected electrons will occur. This enhances the image charge signal and can produce a significant signals in strips that are at a substantial distance away from where the shower occurred. This is not particularly good for the electron signal and for a trigger signal, that is the result of summing some number of adjacent strips, this can be disastrous. The result of summing a number of small negatives with a large positive can be nearly zero.

To compensate for this, a pair of $0.1 \mu\text{fd}$ capacitors have been attached to each lead plate to supply a ballast of negative charge on demand so that the image charge signal is minimized by preventing the local charge depletion of the cathode. Resistors of a few ohms were placed between the capacitors and the lead plates and between the capacitors and their ground to damp MHz oscillations that would interfere with the electronics(See Fig.32). The HALAC does not need ballast capacitors because of the way it is structured. As stated in chapter IV the very large high voltage planes are made of double sided copper clad G-10 with the side opposite to the high voltage held at ground. This in effect forms a ballast capacitor. Additional capacitors were added to one lead plate in both the front and the back sections of each quadrant of the EMLAC and to one high voltage plane in the front and back sections of the HALAC. Their ground sides were attached to a pulsed current source. This allowed the mass testing of each channel's response to injected charge.

Any leakage current in the capacitors would show up as an increase in the level of noise of the readout channels. Several types of capacitors were tested at liquid nitrogen temperatures and the ones selected for use were found to have leakage currents of the order of 0.06 nA at 8 KV ^[1].

[1] Bruce Schneier, "Results of Leakage Tests on Cryogenic Capacitors at High Voltages", E-706 Internal Note 078, (1983).



*Pulsers are attached to H.V. planes 18 and 27.

Figure 32: Schematic of EMLAC High Voltage System

V.2 The LAC Readout Cables

The readout cables were especially made for the experiment by the W. L. Gore Co.. These cables are flat, have $18 \text{ } 0.003 \times 0.062 \text{ in.}$ copper conductors and are approximately 10 m long. They have 0.002 in thick copper shields on both sides. The middle two signal lines were held at ground so that when the cables split at the dewar feed-throughs the signals are still completely shielded. Having the middle two signals at ground also avoided the problem of inadvertently grounding a signal line when the cables were split. The impedance of the cables was designed to match the 13 ohm input impedance of the amplifiers to eliminate signal reflections and maximize

the rise time. A miscalculation resulted in the impedances for the set of cables made for the EMLAC being lower than the amplifier input impedance by a factor of 2. At each end of the cables the conductors and ground shields were soldered to a G-10 connector board. Both ends of the cables insert into female connectors either at the LAC or at the dewar feed-throughs which lead to the channel amplifiers^[2]. There are carbon resistors in series with each signal line on the connector boards that connect to the LAC. These act as back terminating resistors to damp out signal reflections from the amplifiers. The value of the resistors was selected by minimizing the fall time of a signal^[3].

All of the LAC grounds, ie. signal shields, capacitor grounds, etc., were tied to one point on the detector to avoid ground loops that would act as antennae. Ground loops are notorious for introducing noise into a system. A ground loop, by providing a circuit through which current can flow, produces differences in the ground level voltages for different parts of the detector. Fluctuations in the ground loop current produce fluctuations in the ground voltages, a source of signal noise.

V.3 The RABBIT Electronics Crates

Before proceeding further up the electronics chain a brief description of the electronics crates will be useful in defining some terms to be used in the discussion of the LAC amplifiers. The LAC electronics system is based on the RABBIT system developed at Fermilab for the Central Detector Facility. RABBIT stands for Redundant Analog Bused Based Information Transfer. A RABBIT crate normally contains two crate controller cards (EWEs), 19-20 amplifier cards (LACamps), and a terminator card (BAT). The backplane of the crate contains two busses for redundant access to the LACamps and the BAT.

^[2] A. Crowley and T. Ferbel, "Signal-Cabling and Feed-Through System for LAC, *E-706 Internal Note 119*.

^[3] N. Mathur and S. Augst, "Measurements of Impedance of Gore Cable and Matching Amplifier", *E-706 Internal Note 123*.

Each EWE in a crate controls one of the two busses on the backplane of the crate and provides a communications port for the crate to the data acquisition system (DA). So two EWEs per crate provides redundant access to the amplifier cards. Each EWE has one analog to digital converter (ADC) and a set of 8 registers for transmitting data back and forth to the data acquisition system (DA). The registers are;

1	Control Register
2	Status Register
3	Channel Address Register
4	Pedestal Register
5	Threshold control Register
6	ADC Register
7	Read data Register
8	Write Data Register

Table 5: EWE Data and Control Registers

The contents of the control register determined what action the EWE would take on receipt of an execute signal (XQT) from the DA. The status register consists of 16 different bit flags for information about transaction status: busy, done, error, etc. The contents of the Channel Address register determined which module and subaddress in the crate are to be addressed by an analog multiplexer. The pedestal register is used to provide the values for the pedestal DAC for the shifting of individual channel signals to their appropriate baseline^[4]. The threshold control register determines the threshold value against which to test the selected analog signal level as well as the polarity, offset and gain of the ADC. The ADC register contains the results of the last digitization performed. The read data register contains the last byte read from the backplane and the write data register contains the byte to be written to the backplane.

The BAT has three functions. The first is to electrically terminate all of the signals generated by the EWE. The BAT also generates the “before” and “after” timing signals sent to the

^[4] Pedestals are the mean values of the noise distributions for each channel. Since these values are different for different channels the signals must be shifted to do a proper test over threshold.

amplifier cards. When it receives a trigger signal the BAT transmits the "before" signal and at a later time sends the "after" signal. The time between these signals is programmable. Finally the BAT is used to monitor the power supply voltages, the crate temperature, and the timing signals of the crate.

All of the RABBIT crates were mounted in the Faraday room built into the top of the gantry. The power to operate the electronics in these crates was supplied by a Kato Engineering Co. 400 Hz motor/generator transferred through a Teledyne Crittenden Corp. isolation transformer. Transformers which operate at 400 Hz are inherently smaller so less space is taken up in the cramped quarters of the Faraday room. Generating power at 400 Hz eliminates all of the line noise that comes with conventional power sources. The communications of the crates with the data acquisition system passes through a set of optical couplers to filter out noise in the MHz frequency range. Such noise could be induced on communication cables from sources such as SCR switching and arc welding.

V.3.1 Channel Amplifier Electronics

The LAC amplifier cards receive signals from 16 channels of the detector and were designed with the following criteria in mind^[5]:

1	Low input impedance
2	High gain
3	Low noise
4	Stability
5	Fast output for trigger
6	Timing information
7	Remote calibration

Table 6: Amplifier Design Criteria

^[5] D.D.Skow "Feed for the RABBIT E-706 Internal Note 157.

The strength of the signal produced by a shower in the LAC generally ranges from 30-250 fC/GeV. These are very small signals compared to digital signals and an amplifier with low noise and high gain is necessary to reliably amplify the signals to a level that can be digitized by an ADC. Fast rise times are desirable when one is taking data at high rates so that a trigger signal can be made quickly and the amount of dead time is kept to a minimum. An amplifiers with a low input impedance is needed for a fast rise time because of the large capacitances of the LAC, typically 1 to 7 nf. The amplifiers need to be stable so that the most of the run time is spent taking data and not calibrating the amplifiers. They need a fast output to send information to the trigger in a timely manner. Timing information is required to determine which signals are "in time" with the trigger and remote calibration is necessary because the large number of channels dictates that the calibration be computer controlled.

The output from each of the 16 amplifiers on a card goes to three different circuits. These are the fast output (FO), the time to voltage converter (TVC), and the sample and hold (S&H). These provide trigger, timing and pulse height information for signals coming from the LAC.

The sample and hold measures the voltage level of the amplifier at two times separated by the rise time of the largest pulse expected from the LAC, approximately 500 ns. The fall times of LAC pulses are on the order of 60 μ s so the difference in the two values gives an estimate of the pulse height that is free of fluctuations in the ground level. The sample and hold circuits are fed from each amplifier through an 800 ns delay line which has a tap at 180 ns. The delay line provides time for the trigger signal to be generated. If a trigger signal is received by the BAT for a crate, it generates a "before" signal and approximately 500 ns later an "after" signal. Each of these signals opens a switch to a capacitor in the S&H, allowing the capacitors to measure the amplifier output voltage level at those respective times. The EWE then digitizes the difference between the two capacitor voltages as the output signal from that channel.

Each TVC receives the sum of the outputs of four adjacent amplifiers as an input signal. If the input signal is over a programmable threshold set by the BAT then a switch is thrown

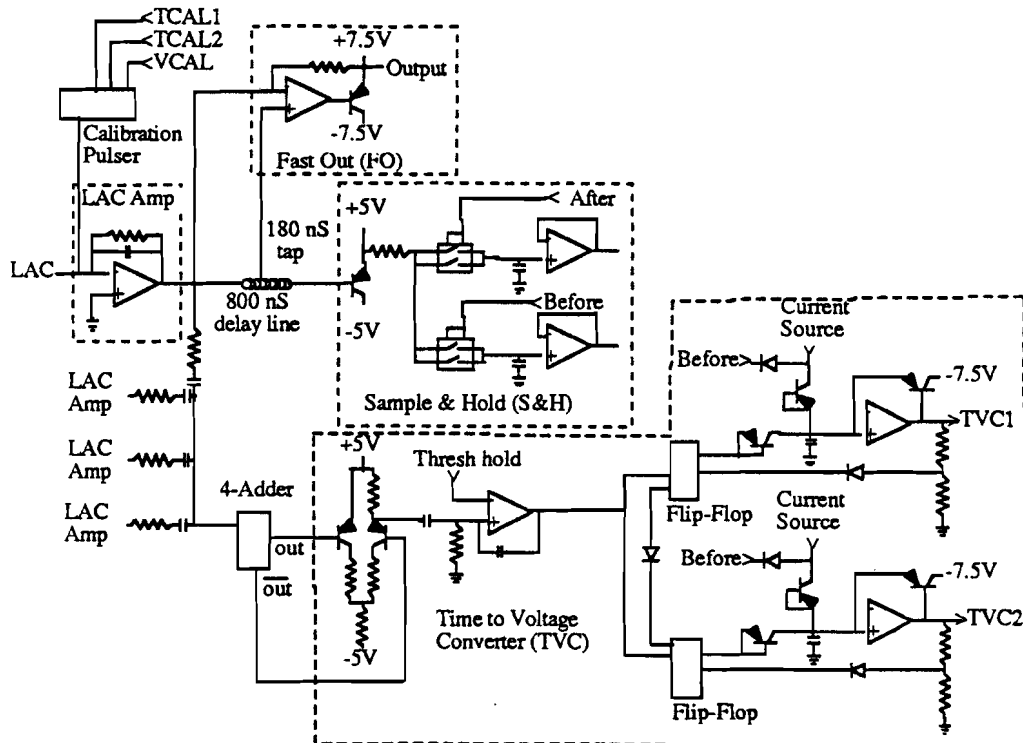


Figure 33: Schematic of LAC Amplifier Showing Sample and Hold, TVC and Fastout Circuits

that allows a capacitor in the TVC to begin charging until a “before” signal is received from the BAT. The capacitor voltage is then proportional to the time between the beginning of an input signal and the receipt of a “before” signal. Thus, the TVC provides information about the timing of a signal in relation to the trigger signal. Out of time signals such as those created by particles in the beam halo can thus be identified and eliminated from the event structure at the time of reconstruction. If a “before” signal is not received then the TVC is automatically reset after $1.5 \mu\text{s}$.

A TVC determines the arrival time of a pulse based on when the signal level rises above a certain point. The timing resolution is significantly smaller than the intrinsic rate limit of the detector because of this, provided the risetime and signal baseline of the detector channels are stable. Based on experience from E-629, the expected timing resolution is $\sigma_\tau = 6 \text{ nsec}$ ^[6].

[6] C. Nelson, op. cit., p.387.

There are in fact two TVCs for every 4 amplifier channels. Each pair of TVCs is set up in a master/slave relationship. If the input from a group of 4 channels triggers a master TVC then the input is switched to the slave TVC approximately 100 ns later. This gives a group of 4 detector channels a 2 hit capability so that the ADC information from groups of strips that receive multiple hits can be properly treated. However, since there is an inherent relaxation time for any given pulse, there is a resulting shift in the baseline depending on the separation and relative heights of two consecutive hits on a group of 4 channels. This causes a shift in the timing information and affects the detection efficiency of a second hit. Furthermore, given that the second TVC will not be active until the first pulse falls below threshold, a second pulse can go undetected.

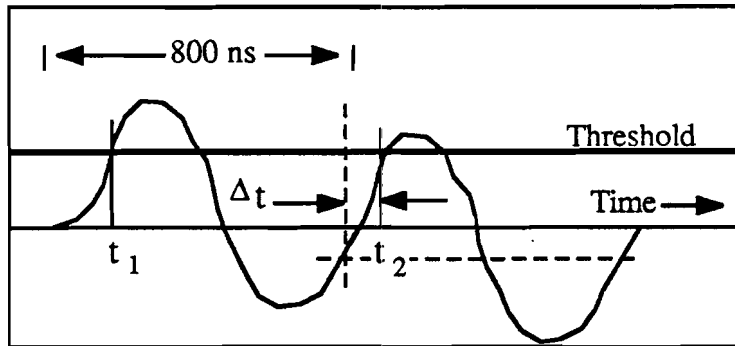


Figure 34: Drawing of Time Shift for a Second TVC Hit

The fast outputs are generated by an opamp that subtracts the amplifier output from itself 180 ns later using the tap on the delay line. This results in a unipolar pulse with a 180 ns risetime and approximately 500 ns duration that is fed to the trigger electronics.^[7]

Each amplifier card also has a calibration circuit that can inject up to two charge pulses of equal height into any of the amplifiers. The height of these pulses can be varied by the BAT so

[7] D. Skow, *Ibid.*

that the gains of the amplifiers and the charging rate of the TVCs can be tested over a range of values of interest. The timing between two pulses can be set by the BAT so that the TVC timing can also be calibrated.

V.3.2 Signal Digitization

The discussion now returns to the RABBIT crates and the next link in the digitization process. The typical cycle for digitizing the voltage from a LACAMP channel was to fill the channel address register with the module and subaddress of the channel of interest., fill the Pedestal register with the pedestal value for that channel, fill the threshold control register with the proper settings , set the control register to select a Test Over Threshold (TOT), and then issue the XQT signal.

The signals from the backplane are selected by the analog multiplexers and level is shifted by the pedestal DAC to account for pedestal differences for individual channels. This level is then multiplied by the selected gain and presented to the ADC for digitization. The level before the programmable gain stage is also sent to the Test Over Threshold section of the EWE. This section has a fixed gain stage of 65 at the input and then a programmable attenuation. The resultant level is compared against a fixed window of ± 50 mV. If the command register is set for a convert without TOT then the ADC digitizes the level. If however, TOT is selected then the results of the TOT determine whether or not the ADC digitizes the signal. If the scaled signal in the TOT is outside the window, then the ADC digitizes the signal. Otherwise, the ADC does not digitize the signal and the status register is set to show that the signal did not exceed the minimal TOT level. This feature is known as zero suppression and was used to cut down on the amount of data that was read out of the detector and to speed up readout time for an event^[8]. The same basic procedure occurs when the TVC signals are digitized.

^[8] The TOT decision takes 3 μ s and the digitization takes 18 μ s, so the average digitization time per channel for 10% occupancy is 4.8 μ s rather than 18 μ s.

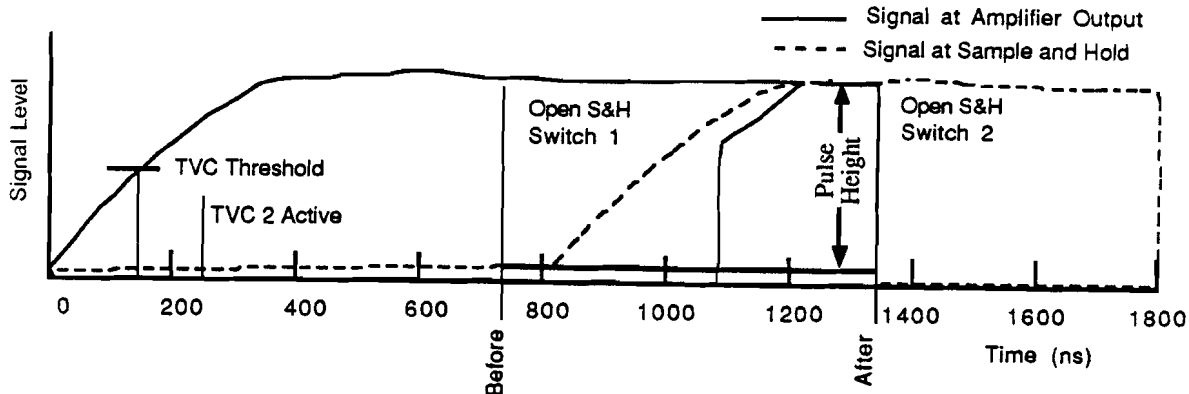


Figure 35: Sample and Hold Time line

V.4 Description of Data Acquisition System

The LAC data acquisition system is part of an integrated computer controlled electronics system. Because of the large number of data channels involved in the E706 spectrometer almost every function from electronics testing and debugging to calibration and data acquisition has fallen under computer control. This is especially true of the LAC electronics.

The data acquisition system for E-706 uses a Digital Equipment Corp. μ VAX 2000 for the data acquisition control master. This machine ran a program called VAXonline that was provided by the Fermilab computing department. Through VAXonline begin and end of run commands are sent to the different spectrometer subsystems. The data from each detector system are collected on the μ VAX, concatenated and dumped to a space in memory called the event pool. From the event pool all events are then logged to tape and submitted to requests by consumer processes that monitor the operational performance of the various detectors. The consumer processes are run on a VAX-11/780 computer which is used to do offline analysis.

Three DEC PDP-11/34s and a PDP-11/45 are used to control the electronics of the different spectrometer subsystems. One handles the tracking system electronics, including the silicon strip detectors and the proportional wire chambers, the trigger system and the Cerenkov detector,

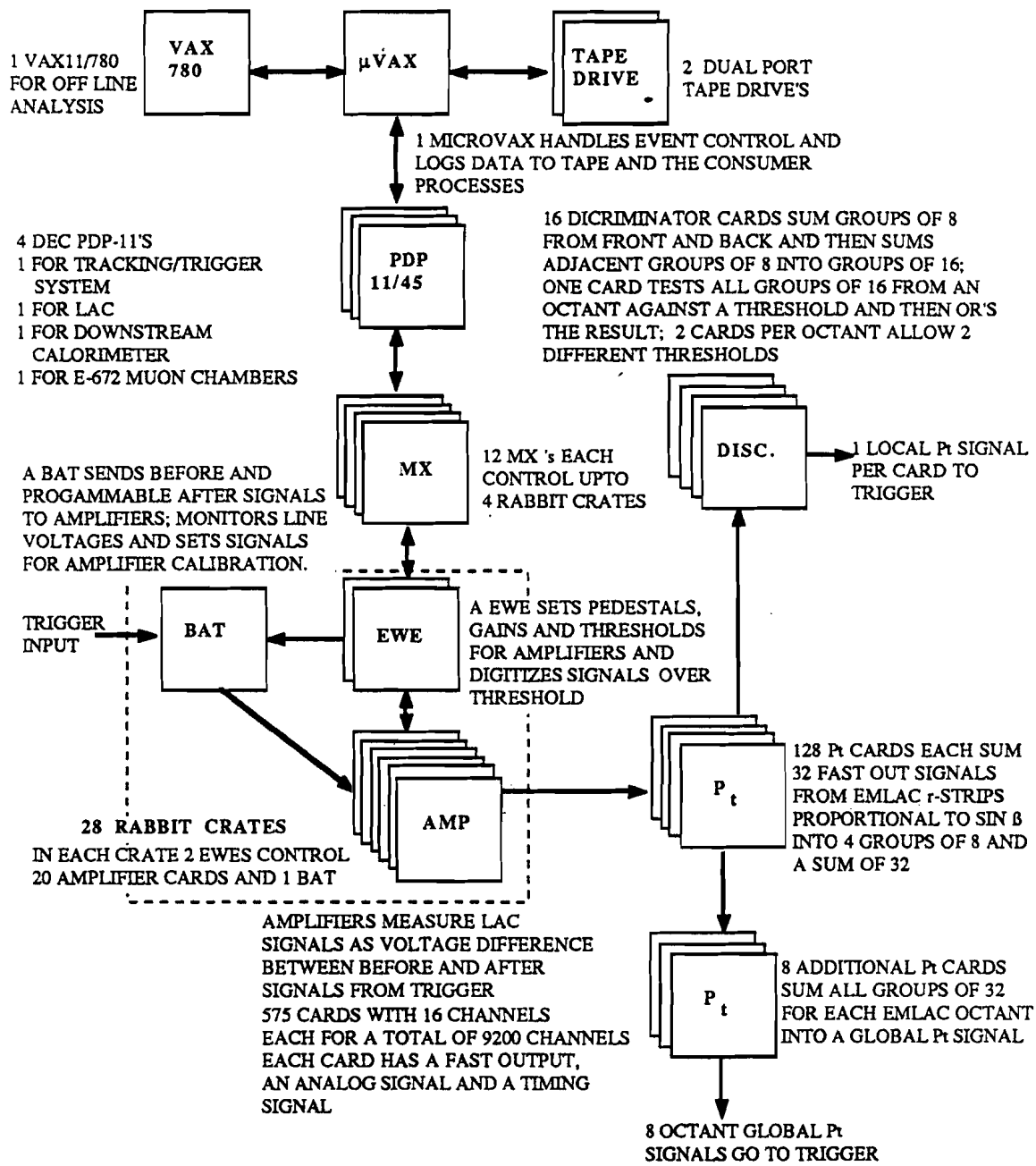


Figure 36: Flowchart of LAC Data Acquisition System

another handles the forward calorimeter. The third handles the LAC electronics, and the fourth controls the E-672 muon system. Upon receiving an event signal from the trigger the PDPs collect and transmit the event data to the μ VAX and then signal the trigger that they are ready for the next event.

The PDP-11/45 is dedicated to controlling the 12 MXs used in the LAC data acquisition system to control the RABBIT electronics crates. During a data run it collects and transmits event data to the μ VAX and at the beginning of selected runs the PDP collects pedestal and gain reference data for each amplifier.

The MX is a dedicated computer developed at Fermilab for use in the RABBIT electronics system. Each MX can handle up to eight data communication busses in a RABBIT type system. Since each crate has two busses, this typically limits the MX to controlling up to four crates at a time. However, given crates that have only one EWE and therefore access to only one bus, the MX can control up to eight crates at the cost of losing redundant access to each crate.

V.5 Description of the LAC Trigger Electronics

To avoid sifting through millions of events to find the relatively few high p_T direct photon events it is necessary to have the electronics decide at the time the data is taken whether or not an event could be a direct photon candidate. A signal from a highly localized shower with high transverse momentum would be indicative of direct photon event. The r/ϕ geometry of the EMLAC allows one to form a signal based on the p_T content of the event and how localized it is. A p_T signal can be generated by breaking the r -strips into small groups that roughly cover the width of an electromagnetic shower and weighting the integrated signal from the fast outputs of those groups by the sine of their angle with the beamline. The logical "or" of signals from adjacent groups tells how localized the p_T signals are.

The fast out signals from the r -strips only are fed into a RABBIT crate containing trigger electronics cards (p_T cards) developed for E-706. A p_T card takes 32 input signals and sums

adjacent pairs of channels and then attenuates the sum in proportion to the sine of the angle the corresponding strips are displaced from the beam line relative to the target. The outputs are then summed into 4 groups of 8 channels and a sum of 32. The signals from the sums of 32 are in turn fed into a p_T card where the resulting sum of 32 output is a uniformly weighted sum of all the r-strip signals from both front and back for an octant. This provides a global estimate of the transverse momentum involved in an event for that octant^[9].

The signals for the sums of 8 are fed into a set of cards called discriminator cards. Inside these cards signals from corresponding sets of strips in front and back are added together and the result is then fed into a test over threshold and that result goes to a logical "or" with the neighboring sums of 8. Each discriminator card does this for all sums of 8 for a given octant. The result is a signal indicative of any localized shower with a high transverse momentum content.

[9] P.Gutierrez and D. Skow, "Test of Trigger Electronics", *E-706 Internal Note 099*.

Chapter VI

Adjustment of the LAC Parameters

Once the LAC was filled with argon and ready to take beam, there were many parameters that needed to be adjusted for it to realize meaningful data. At the most elementary level this amounts to measuring the amplifier signal levels and adjusting parameters such as the "before/after" timing gate and the threshold level so that the signals are optimal. Once this has been accomplished, one can proceed to study the calorimeters response to energy and its basic uncertainties in measuring that energy.

The conversion of raw data from the amplifiers into a measure of the energy deposited in the LAC is done using the formula.

$$E = C_{EM}(e/h) \times \sum_{i=1}^n g_i \times (s_i - p_i) + C_H(e/h) \times \sum_{i=1}^m g_i \times (s_i - p_i), \quad (31)$$

where g_i , p_i , and s_i are the gain, pedestal and signal for channel i . $C_{EM}(e/h)$ and $C_H(e/h)$ are the conversion constants for the EMLAC and HALAC respectively, they take on different values depending on whether the particle is electromagnetic or hadronic. After a brief discussion of various tests done to check the integrity of the LAC the rest of this chapter will be spent examining topics which contribute to the uncertainty of the energy that results from Eq. 31.

VI.1 High Voltage Testing of the LAC

Both the EMLAC and HALAC were tested for shorts from the high voltage planes to their anode planes prior to being sealed inside the dewar. One at a time, the high voltage planes were connected to a 0-10 KV voltage supply with all of the strips or pads grounded together. The EMLAC lead plates were tested for holding voltage up to 3.4 KV. The maximum voltage applied to a cookie high voltage plane was 4.0 KV. The minimum Voltage required for passing

this test was 2.5 KV. High voltage problems were usually caused by dust in the argon gaps and was generally rectified by passing a strong flow of dry nitrogen gas through the gap. However, sometimes it was necessary to connect the plane to a high current supply and burn the short out.

High voltage testing was also done after the cryostat had been filled with liquid argon and before the amplifiers were connected so that the operating voltage could be determined. Since the electron drift velocity in argon begins to plateau for electric fields near 10 KV/cm it was desirable to operate the EMLAC and HALAC cells at 2.5 KV and 3.2 KV respectively. Some sections of the LAC could not operate at fields this high without the high voltage arcing to ground, despite the previous testing, so the affected high voltage planes were operated at reduced voltages. Ultimately two quadrants ran with only 1.8 KV on their back sections and one quadrant had four plates in the front section with reduced voltage. Three of these plate were held at 900 V and one plate was at 350 V.

VI.2 Capacitance and Isolation Testing of Strips and Pads

Each detector channel underwent a series of tests to measure its capacitance and check if it was shorted to neighboring channels. These tests were computer logged and driven by a RABBIT crate interfaced to an IBM PC. The RABBIT test card used for the HALAC was designed and built by the Particle Instrumentation Group at FNAL. A similar card was made for the EMLAC by the University of Rochester. These cards had two abilities, they could measure the Resistance between two points and the capacitance between a point and ground. To determine if a channel was properly isolated from its neighboring channels the resistance between it and its neighbors was measured. The resistance was determined in the usual manner by measuring the voltage drop of a current across a known resistor. By measuring the capacitance one was able to determine if all of the strips and pads of a tower were connected together. The capacitance measurement was a triggered process. The channel address was loaded and a trigger pulse fired.

This would charge up the channel and then it was drained through a known resistor. A sample voltage was taken at two points in time, using a timer circuit and two sample hold circuits. The output of each sample hold circuit was fed into an opamp and the difference was converted by the ADC in the EWE. The time rate of change of the voltage indicates the size of the channel capacitance.

These tests are in some sense redundant so that some problems could be caught in one test where they might have been missed in another. Cleaning of the card edge connections or blowing out the channel with nitrogen usually solved any problems. Ultimately, there were 13 strips in the EMLAC and 38 pads in the HALAC discovered by this testing that could not be repaired.

VI.3 Monitoring of the Liquid Argon Purity

The purity of the argon in the LAC was monitored in three different ways. A connection to the top of the cryostat allowed the extraction of warm argon gas for analysis. The gas could be condensed into a ionization test cell (Rahm Cell). Here the charged produced by a β -source (Ru^{106}) could be monitored as a function of the voltage applied to the ionization cell. A reduction in the height of the curve over time is an indication of contamination of the argon by an electrophilic substance. The curve for the collected charge versus voltage is parametrized by the following equation;^[1]

$$\frac{Q}{Q_0} = \frac{2\lambda}{d} \left(1 - \frac{\lambda}{d} \left(1 - \exp \frac{-d}{\lambda}\right)\right); \lambda = \frac{\alpha|E|}{p}, \quad (32)$$

where Q_0 is the deposited charge, d is the width of the argon gap, and λ is the mean free path of the electrons defined in terms of the electric field E , the equivalent oxygen impurity concentration p , and a parameter $\alpha \approx 0.12 - 0.15 \text{ cm}^2 \text{ ppm O}_2/\text{KV}$.

^[1] E. Prebys and F. Lobkowicz, "High Voltage Dependence of Signals in LAC", *E-706 Internal Note 163..*

The argon for the LAC arrived at the lab in transport trucks. Each load of argon was tested in the Rahm cell for its purity. If the impurity level was below 0.8 ppm the argon was accepted for delivery. After the data acquisition was over two voltage curves were taken using the Rahm cell, one using argon from the LAC and one with argon from the storage dewar which had argon left from the initial fill of the LAC. The two curves indicate an O_{2eq} contamination increase of 1.4 ppm for the argon in the LAC relative to the argon from the storage dewar (See Fig.37).

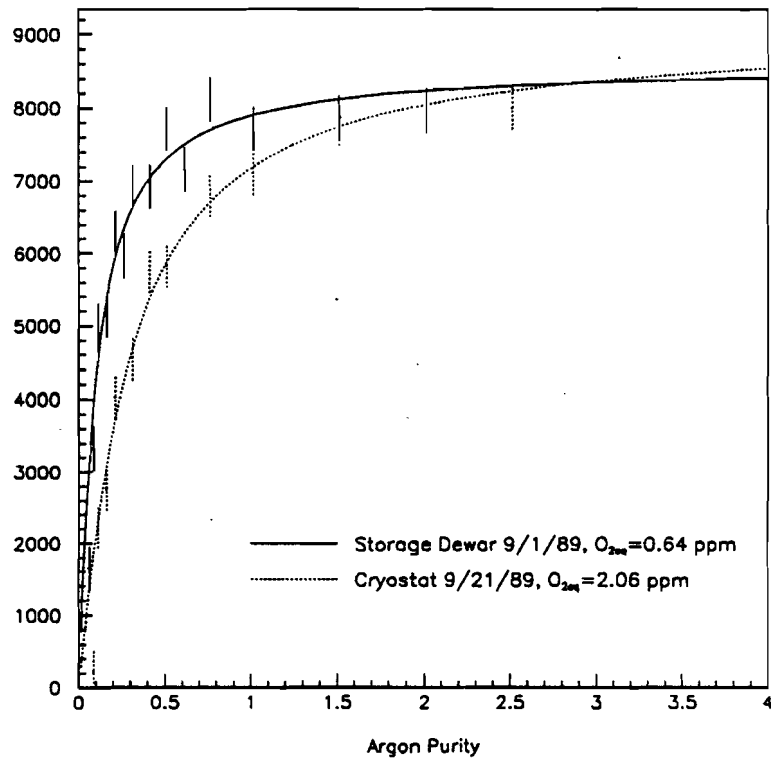


Figure 37: Voltage Curves of Argon Indicating Level of Contamination

Voltage curves were also measured with the detectors themselves by monitoring the charge collected from a beam of electrons of constant energy. A decrease in the amount of charge collected was seen with time (See Table 7). Alternatively a sample of the argon gas could be

made to flow through an oxygen analyzer. Measurements made with the analyzer several months after the dewar was filled indicate a contaminant level of the order of 1 ppm.

Date	EMLAC	HALAC
10/26/87	50.3	43.5
12/9/87	45.0	44.0
2/15/88	45.0	40.0

Table 7: Percent Charge Collection Efficiency of the LAC with the EMLAC at 2.5 KV and the HALAC at 3.0 KV

All of these methods can only indicate the degree of contamination. They can not identify specific substances as culprits. To identify the source of the reduction in the height of the voltage curve, several samples of gas were sent to independent laboratories for mass spectrometer analysis. The results from these test so far indicate less than 1 ppm O₂ equivalent contamination for the following compounds; N₂, O₂, CO₂, H₂, He, CO, CH₄, Cl, Br, NO₂, ClO₂, and Organics. Most of these results are upper limits imposed by the sensitivity of the testing apparatus and so a main culprit in the contamination of the argon has yet to be identified.

The charge collection efficiency calculations were based on the amount of energy a minimum ionizing particle (MIP) would deposit in the active layers of the calorimeter. This over estimates the energy actually deposited by about a factor of two. Electromagnetic showers produce lots of low energy photons. The energy attenuation of these photons deviates significantly from that for MIPs and is much more material dependent. At these energies the photoelectric effect, which has a Z⁵ dependence, becomes important. This material dependence results in much more of the energy for these photons being absorbed in the lead absorbers than is the case for MIPs^[2]. The result is that a 60% charge collection efficiency is the best that the LAC is capable of, as long as the calculation is based on the energy deposition of MIPs.

[2] R. Wigmans, op. cit., pp. 393-395.

VI.4 History of the Electron Beam Calibration for the LAC

The first data acquisition period for the E-706 spectrometer was from July 1987 to March 1988 with most of the data acquired during the time from the beginning of January to the end of February 1988. The three months prior to this time were spent leak checking the dewar and filling it with liquid argon. The time from July 1987 to early December 1987 was used to debug the various detectors and the data acquisition system. This included setting the various parameters for the LAC such as the pedestals, gains, and threshold settings for properly measuring the deposited energy of the particle showers. The remaining time was spent accumulating data. There were two calibration sessions for the LAC during this period of time. The first was in December 1987, the second at the end of February 1988.

During the first calibration session the hadron shield blades and the final quadrupole of the beamline were left in place. This limited the vertical movement of the beam to $Y = \pm 5.5$ cm at the face of the EMLAC. With the LAC moved to a position of $X = 52.85$ cm the dead region along the X-axis extends from -3.06 to +3.06 cm in Y. This does not leave quite enough space to fully contain the lateral spread of electron showers. It was thought, however, to be sufficient for a ballpark determination of the constants for converting the ADC counts of the electronics to energy and to determine the width of the "before" and "after" timing gate. A full calibration study requires dismantling part of the spectrometer.

For the second session the final beamline quadrupoles, the analysis magnet and the silicon strip detector were rolled out of the beam line and the vertical blades were removed from the hadron shield. Using the vertical dipole in the beam line to pitch the magnet vertically the test beam could be scanned over the entire face of the LAC by moving the gantry horizontally. These data will be discussed in the next chapter.

VI.5 Selection of the Before/After Timing Gate

To read the signal heights from the LAC the before/after timing gate must be properly

selected. As discussed in the previous chapter the “before” and “after” signals trip switches in the sample and hold so that the signal height is measured at those times. The “before” is timed to measure the baseline height of the LACamp before the signal arrives the timing of the “after” is then set so that the signal maximum is measured. While the decay time of a pulse is significantly longer than the rise time, making the gate much longer than the rise time of the signal only adds noise to the signal and decreases the energy resolution of the detector.

The timing between the “before” and “after” signals was determined using the calibration beam. Measuring the sum of the channel signals near the beam as a function of the width of the timing gate between the “before” and “after” provides a means for selecting the appropriate timing. With the “before” signal always issued 70 ns before the arrival of the LACamp signals the gate width which maximized the signal output from the channels was found to be 570 ns. The rise time of the signals is then 500 ns (See Fig.38). This timing gate implies a limiting data rate for the calorimeter of 1.75 MHz. If the gate were to be narrowed as much as possible the rate would only climb to 2.0 MHz and the reliability of the measured signal heights would be compromised. Once the timing was set the conversion constants were determined to be, $C_{EM}(e) = 3.1 \text{ MeV/ADC count}$, $C_H(h) = 48 \text{ MeV/ADC count}$

VI.6 Electronic Sources of Energy Fluctuations

The two primary sources of energy fluctuations for the LAC are the capacitance noise from the strips and pads and the fluctuations in the values of the gains for each channel. It is crucial to assess the magnitude of these sources so that their affect on the energy resolution of the LAC can be gauged. The fluctuation of gains is potentially the most important factor in the energy resolution of the calorimeter. Since it is a multiplicative factor it affects the entire energy scale. Pedestal fluctuations are nearly as important. While the pedestal fluctuations represent for the most part changes in the offsets for individual channels that become less important at higher energies they can have more insidious effects. Significant differences between the r and ϕ

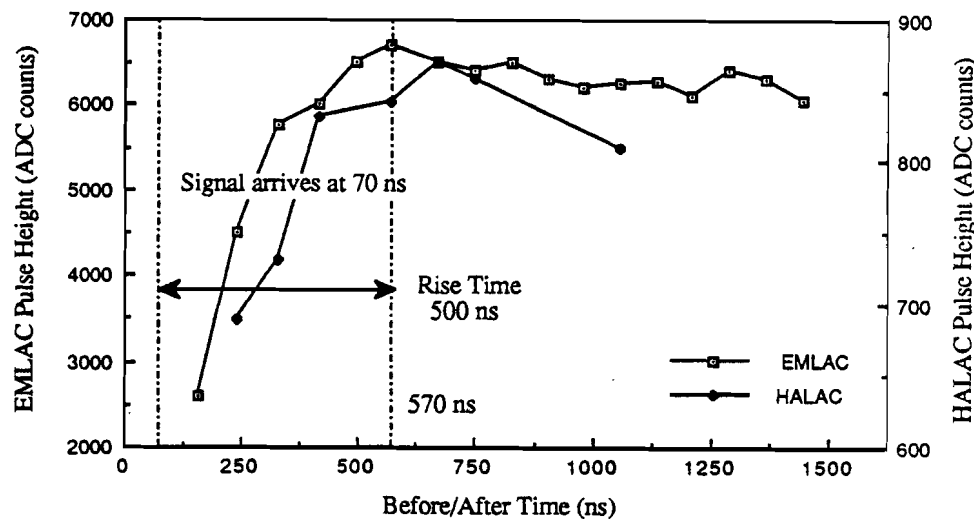


Figure 38: LAC Signal Height Dependence on Width of Before/After Timing Gate

pedestals of the EMLAC can play havoc when the reconstruction program attempts to correlate energies between them. A lesser source of noise comes from the variation of threshold for zero suppression. While this does not directly modify the channel signals it does introduce effects through the variation of the number of channels that are used to reconstruct the showers.

VI.7 Zero Suppression Window

It is desirable to reduce the number of channels that are actually read out for each event because the LAC has nearly 10,000 data channels and only about 10% of them are occupied at a time. Reducing the number of channels to be read out decreases the time to store an event and thus the amount of dead time for taking data. This is the reason for the test over threshold

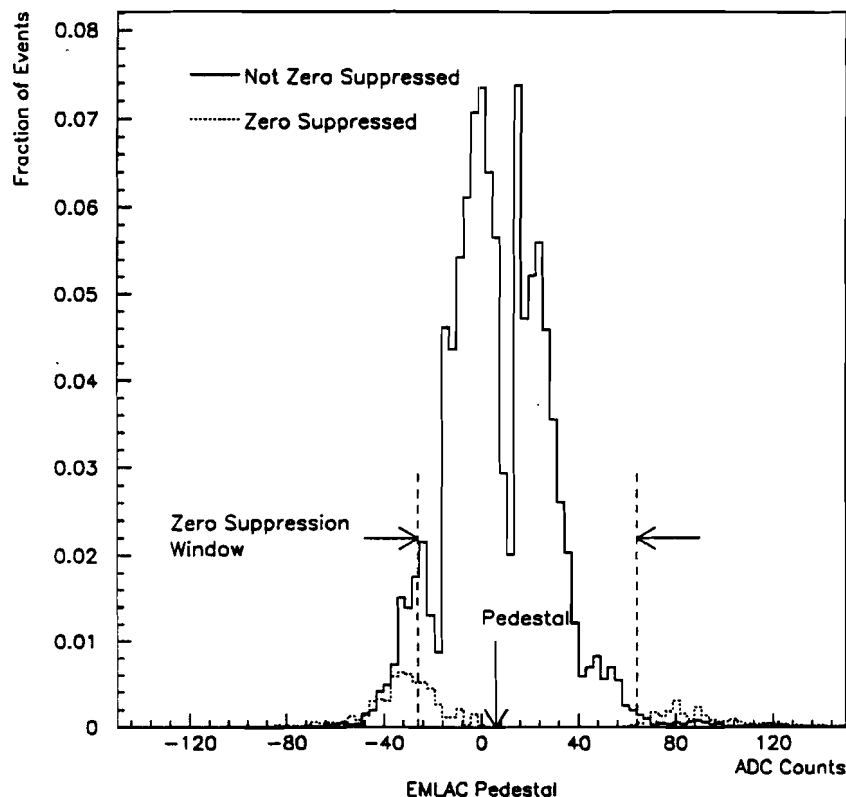


Figure 39: Distribution of EMLAC Channel Noise with and without Zero Suppression

when the signals are digitized (see chapter V). This procedure is also known as zero suppression (See Fig.39).

As noted previously the threshold values are fixed. The value for the test over threshold was chosen by adjusting its value until the number of channels read out did not limit the speed of the data acquisition system. What matters then, for the stability of the TOT, are changes in the settings for the pedestal DAC. These settings shift the LAC signals so that their pedestals should be centered in the threshold window. The pedestal settings were determined approximately every four hours during the run with the beam off. Analysis of this data for a

two week period of time show the settings to be stable to within three DAC counts. For the LACamps four pedestal DAC counts are equivalent to one ADC count. So the settings are stable to about 2 MeV per channel in the EMLAC. Fluctuations in the pedestal DAC setting can have more drastic effects on the resolution of hadronic energy because of the much larger fluctuations of hadronic showers.

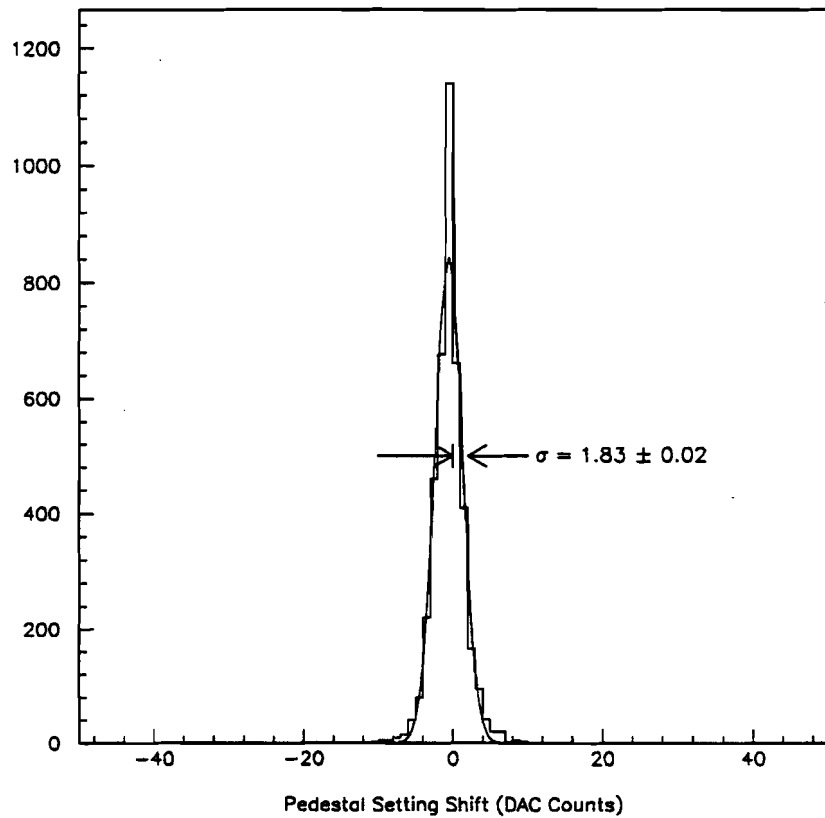


Figure 40: Distribution of Pedestal Settings for a Crate of Amplifiers from Cold Start Data over a Two Week Period

To determine the pedestal DAC settings the channel address line and its return for a Ewe are tied together at the multiplexer. The pedestal DAC is then set at 8000 hex, which should ideally be the ground setting. This setting is then increased until the test over threshold was triggered. The DAC is then reset at 8000 hex and then lowered until the lower test over threshold was triggered. The pedestal DAC initial setting for all channels is taken as the average of these two values. The settings for individual channels are determined by loading the DAC setting, determining where the pedestal is in the zero suppression window, and then adjusting the DAC setting accordingly. The pedestals determined from this procedure are stored as part of the run constants for later use in the reconstruction procedure. New pedestal settings to be used for each channel were determining roughly every four to six hours so that any drift of the pedestals with time would have a limited effect on the data.

VI.7.1 Pedestal Stability

An alternative way to find the pedestals from the threshold method is to collect data without the zero suppression threshold and with the beam off. If one were to randomly sample data from a LAC channel, without particles depositing energy in the detector, the resulting distribution should be approximately gaussian. This distribution is the intrinsic noise of the channel and the mean of the distribution is referred to as the pedestal (See Fig.41). Typical EMLAC channel pedestals have a value near 6500 ADC counts and the sigma of the distributions (σ_{pd}) is 26 ADC counts or about 80 MeV. Since it was impractical to determine the pedestals in this manner due to the amount of time required, this was only done occasionally to check the validity of the first procedure. For the HALAC the width of the noise peaks for the front and back sections were found to be 19 and 29 ADC counts respectively.

To examine the stability of the pedestals during the run one has to estimate the pedestal from the tails of the noise distribution. If the zero suppression window is properly centered this amounts to about 3% of the distribution. If the window and the pedestal are not centered

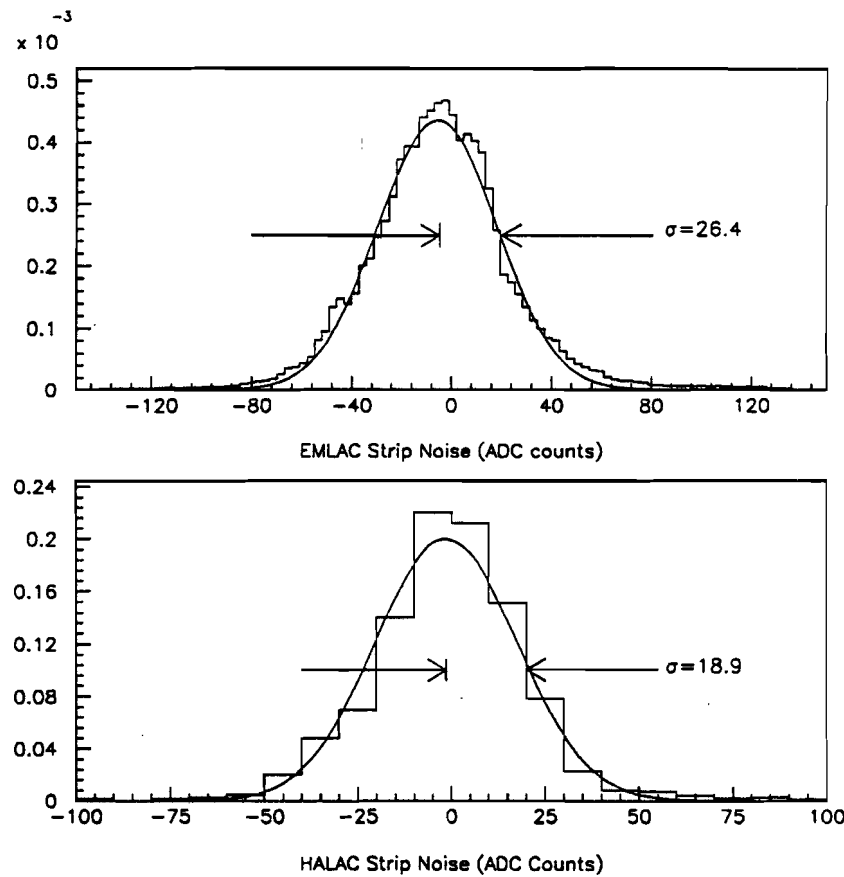


Figure 41: LAC Channel Noise Distributions with Pedestal Subtracted

then more of the noise distribution is available to estimate what the relative shift is. Results of the analysis clearly indicate significant systematic shifts of the pedestals from their cold start values. There is a periodic structure of the shifts on a 16 channel level which corresponds to the number channels per card. Even more pronounced are the negative 10 to 80 count shifts of the pedestals in the first amplifier card of the first ewe in each crate (See Fig.42). This shift does not occur for the first card of the second ewe of the crate. These shifts may be the result of some digitization effect. A comparison of the pedestal shifts from runs 5 hrs apart indicated a general drift of the pedestals by about 13 ADC counts.

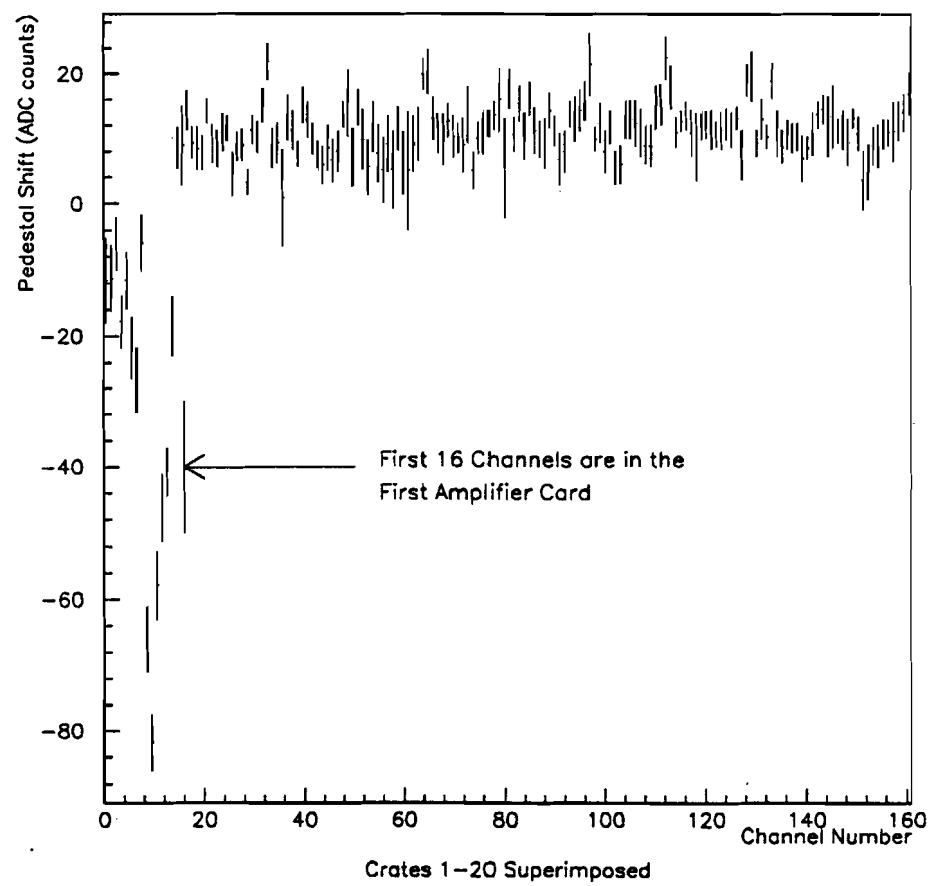


Figure 42: Channel Pedestal Shifts for the First Ewe of a Crate

VI.7.2 Measurement of the Amplifier Gains

The values of the gain for each electronic channel were determined at each cold start by measuring the amplifier outputs associated with pulses from the on board calibrators of several different pulse heights. The cold start gains task took eight readings at each of five values over the full range of the ADC.

After the gains are measured it is important to normalize them with respect to one another in order to remove any systematic effects introduced by the measurement procedure. Since each card has its own charge injector on board, it is possible to normalize the gains of the sixteen amplifiers on each card relative to one another. Normalization between cards is not possible because the cards have not been calibrated against a single charge source. Even if this were possible with a testing station the normalization would not be absolute because the amplifiers would not be connected to the LAC. Variations in the detector and cable capacitances result in changes of the individual amplifier gains.

The time fluctuations of the gains were tested by repeatedly measuring them for the amplifiers on a LACamp card over a period of several days. From this variations of the individual amplifier gains with time are estimated to be less than 0.3%. Detector wide variations in the gains are less than 2.5% based on the distribution of the gains taken from the run constants (See Fig.43). The smaller second peak in this figure corresponds to the strips in the back outer- ϕ section of the EMLAC and is a result of their much larger capacitances. The gains of these strips can be renormalized so that they lie within the main distribution.

VI.8 LAC Data Transfer Reliability

Occasional problems with large negative channel energies are presumably due to inaccurate data transfers. The 16 bit ADC were guaranteed to only 14 bits and tests done on reading channel addresses showed occasional problems with higher order bits. These problems are concentrated in particular crates and affect approximately 6% of the data transfers. This was determined by

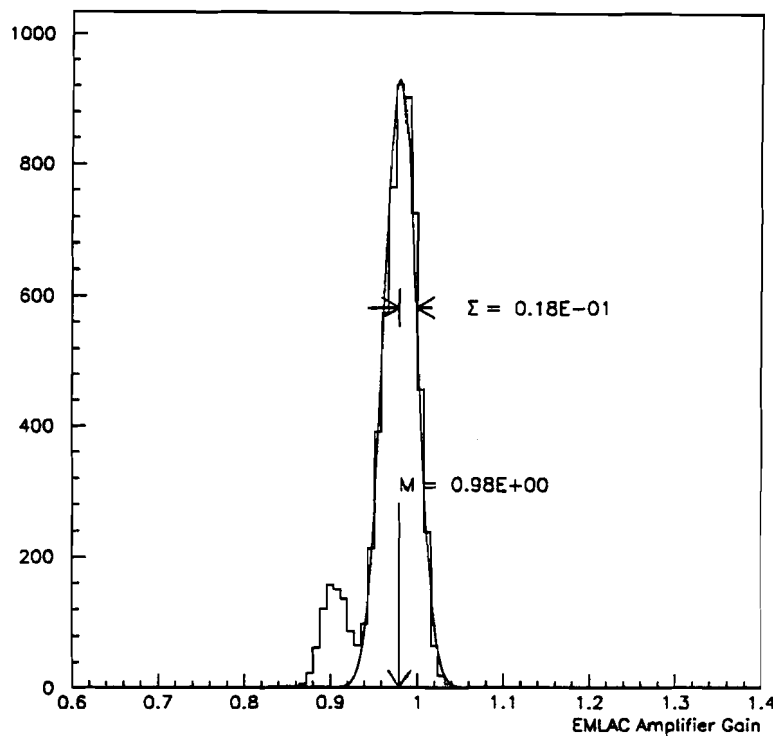


Figure 43: Distribution of the Amplifier Gains for the LAC

altering the data acquisition program to read the prom address of the amplifier card rather than the amplifier output.

VI.9 Determination of the TVC Pedestals

The basic goal in calibrating the TVCs is to establish a proper "zero-time" or pedestal for each TVC. Two methods are employed to accomplish this, the "cold-start" method and the "data" method. During the beginning of each run a "cold start" was executed at which time several calibration tasks were run to initialize the calorimeter and measure various quantities such as pedestals and gains. As part of the cold-start "gains" task a timing curve was taken for each TVC. Two pulses, approximately 300 ns apart, were injected into each channel to trigger

both TVCs. The position of the "before" gate was then varied relative to this signal and the resultant TVC readings were stored. These points are then fit to a line to extract the zero time.

For reasons which are not well understood, the linearity curves that result from this method often have missing points. This makes fitting some of them difficult or impossible. Also it appears that the second TVC was occasionally fired by the first pulse, creating a double peak in the pedestal. Unfortunately the two peaks are too close to be unambiguously resolved in all cases.

In the "data" method, data for each TVC is accumulated over the course of several runs. If the TVC and the trigger are functioning properly, there will be a peak at the zero time. The distributions are fit to extract this peak which is the pedestal. The problem with using the data method of forming pedestals is that in areas of low occupancy it takes many runs to accumulate enough statistics for a good pedestal, particularly for the second hit TVC.

VI.10 Image Charge Effects

When a shower occurs in the calorimeter it deposits electric charge in the argon of the sampling cells. This deposited charged induces an image charge, of the opposite sign, on the anodes of the calorimeter. This has a deleterious affect on the trigger. In fact, the trigger signal can be effectively nullified in some instances. The trigger sums signals from groups of channels. This means that the signal from the strips which contain the shower and the signal of opposite polarity from the strips which have only image charge are summed together. Add enough negatives to the positive and the result is zero signal. For the local p_T signal, which is only a sum of eight r-strips, the effect is minimal. For the global p_T signal, which is a sum of all the r-strips in an octant, the effect is severe. The size of this effect obviously depends on the size of the shower involved. What is worse is that the effect is position dependent because of the varying size of the r-strips and the $\sin(\theta)$ weighting of the strip signals.

In an attempt to deal with this problem, diodes were installed in the signal lines going to the p_T modules (See Fig.44). This clips any positive signal coming from the detector. The

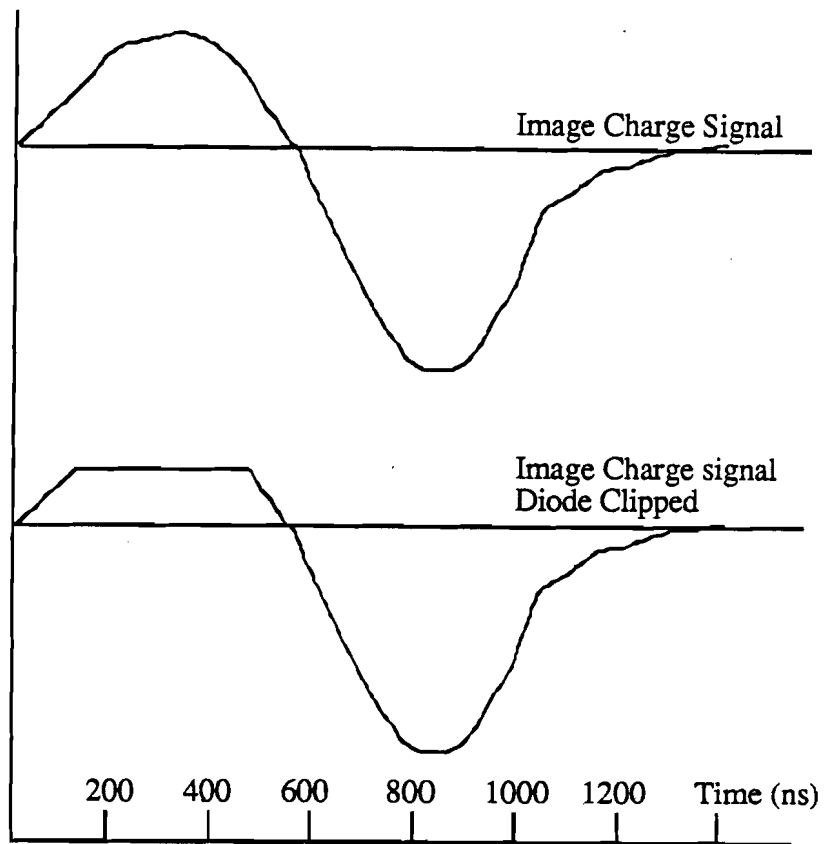


Figure 44: Drawing of Image Charge signal with and without Diode Clipping

effect is not completely eliminated because the diodes have a turn on voltage that allows for a small positive signal. The image charge signals are also shifted in time relative to the charge signal. This shift has some dependence on the distance from the shower and also on the shower's position. The net result of summing all the out of time signals with the real signal can be a reduction in the signal height with an accompanying shift in the timing of the global trigger. The result can wreak havoc on the efficiency of the global p_T trigger (See Fig.45).

This is a serious effect because any cross section measurement depends on how efficient the trigger used to collect the data was. If the trigger efficiency is position dependent then it becomes a very difficult task to measure the efficiency. If the problem is severe enough then the

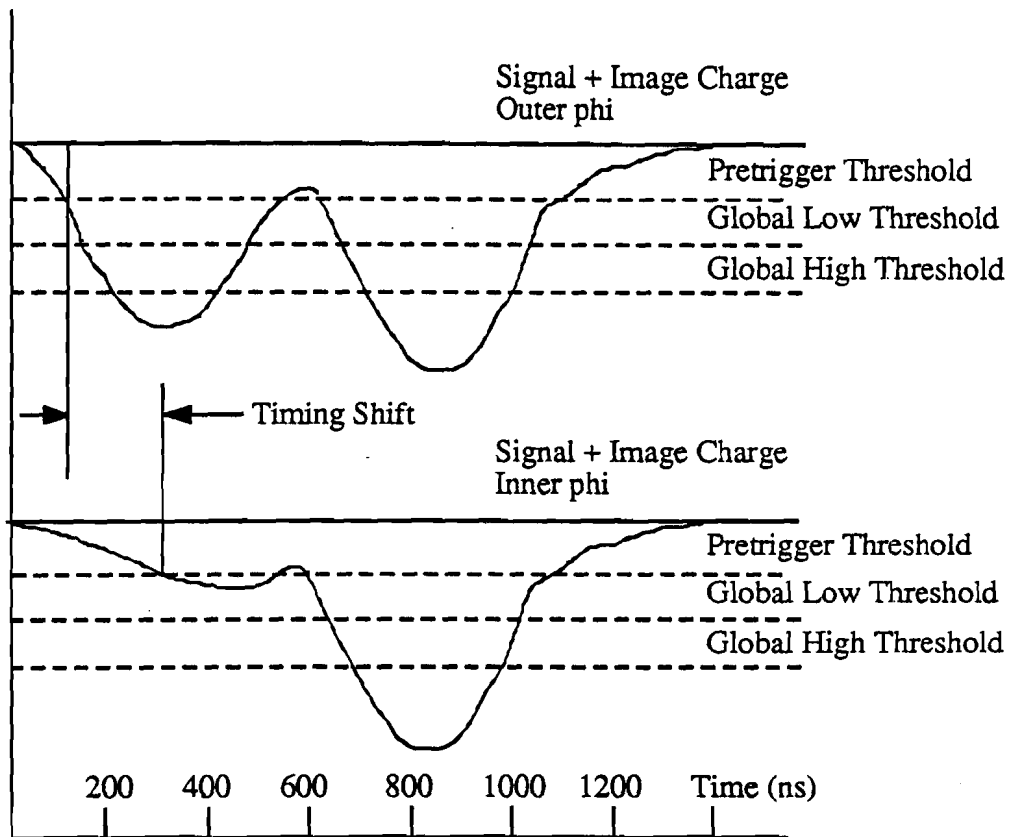


Figure 45: Drawing of Signal with Image Charge for Inner and Outer ϕ sections of the EMLAC

uncertainty in the trigger efficiency becomes the dominant term in the uncertainty of a cross section or the measurement of a cross section may be rendered meaningless.

Chapter VII

Reconstruction of LAC showers into Photons and Hadrons

In order to make use of the data from the LAC, the signals collected from the strips and pads must be converted and correlated with one another to reconstruct the particles that caused the showers. This can be a very difficult problem when several showers form in the same region of the detector. This chapter will discuss the reconstruction programs used for the EMLAC and HALAC data after a brief description of the conversion of the raw data. A discussion of the TVC reconstruction will follow.

VII.1 Conversion of Raw ADC Data to Energy

The ADC pulse height data of the strips and pads are converted to energies in the following manner. First, a pedestal is subtracted from the ADC count for a channel. Then it is multiplied by the relative gain of the channel amplifier. Corrections due to the effects of the detector RC risetime on the pulses are also applied. This has practically no effect for detector capacitances less than 3 nf (EMLAC channels) but is about 10% at 10 nf (HALAC channels). The ADC count is finally converted to the energy by a conversion constant for each detector. These constants are 3.1 MeV/count for the EMLAC and 49 MeV/count for the HALAC.

VII.2 EMLAC Reconstruction

The reconstruction code for the electromagnetic section of the LAC is called EMREC. Its functions can be broken down into three main parts. The first part deals with finding groups of strips with energy deposited in them and the peaks in those groups in each of the four views (left r , right r , inner ϕ , and outer ϕ) of the calorimeter quadrant. In the second part, the code reconstructs "gammas" in each view from the detected peaks. The gammas are an intermediate

step in the final photon reconstruction. The last part correlates the gammas in the r and ϕ views to form the reconstructed photons^[1].

As previously mentioned, the EMLAC is physically split into a front and back section which are read out independently. For reconstruction purposes, corresponding strips in the front and back are added together to form software signals. This is done to minimize the dependence of the shower shape on the Z position of the shower origin. All final reconstruction is performed on these summed energies. As will be seen, however, front and back sections contain additional valuable information on radial positions as well as on the ratio of energy deposited in the front and back sections of the EMLAC (E_{front}/E_{back}).

VII.2.1 Correction for Dead Strips

Dead strips produce severe local effects on the energy resolution. These strips can split a large shower and make it appear as two smaller ones. This effect was quite noticeable in the calibration data where the beam center was frequently targeted on one of these strips. The eighty two known dead strips in the EMLAC and the thirteen known dead pads in the HALAC are flagged at the time the data is unpacked. At this time the gain associated with each channel is examined. If a gain was found to be anomalous then that channel is also flagged. A partial energy correction is made for these strips. If, during reconstruction, a strip adjacent to one of the flagged strips is found to contain energy. The energy equivalent to the average of the two adjacent strips is added to the affected strip. This procedure was found to be effective in improving the resolution for isolated electromagnetic showers.

VII.2.2 Group and Peak Finding

For any particular view a group is defined by the presence of consecutive strips with energy

[1] J. P. Mansour, " π^0 Production from π^- and P Beams at 530 Gev/c on Be and Cu", *University of Rochester Thesis*, Chapter IV, (1989).

above a predefined threshold. In order that a sequence of strips be called a group they must pass the following criteria:

- (1) For left and right r -views and the inner ϕ -view there must be at least 3 strips. For the outer ϕ -view this requirement is reduced to 2 strips due to the larger width of these strips.
- (2) The total group energy must be above 750 MeV.
- (3) The average energy per strip must be above 150 MeV.
- (4) The maximum energy strip must be above 300 MeV. Once all these conditions are met the group is stored in a designated data bank and the code starts the search for peaks.

Peaks are found when the slope of the energy distribution in the group changes from a positive to a negative value. Associated with each peak are two valleys located to either side of it. A valley is defined as the low point between two peaks or the end strip in the group. Peaks are searched for in the front section since adding energy between the front and the back tends to obscure low energy peaks. Two quality factors are next calculated as the energy difference between the peak strip and its left and right neighbors divided by the sigma.

For each peak the energy is summed in the strips between the peak's front valleys. If the view that the peak was found in is a radial view its "r" position is calculated and a search is implemented for a corresponding peak in the back section that would yield a back radial position. One can then calculate the directionality of the incident photon with the "r" positions of a shower from the front and back sections of the calorimeter. This is not done for the ϕ views.

VII.2.3 Gamma Construction

The reconstruction of a gamma depends on the group that it comes from. A one peak group is easily handled in that the position and energy calculations can be immediately executed. The reconstruction of gammas from a multiple peak group is not as clear cut. The group first must be split to equivalent one peak groups before the positions and energies can be calculated (See Fig.47).

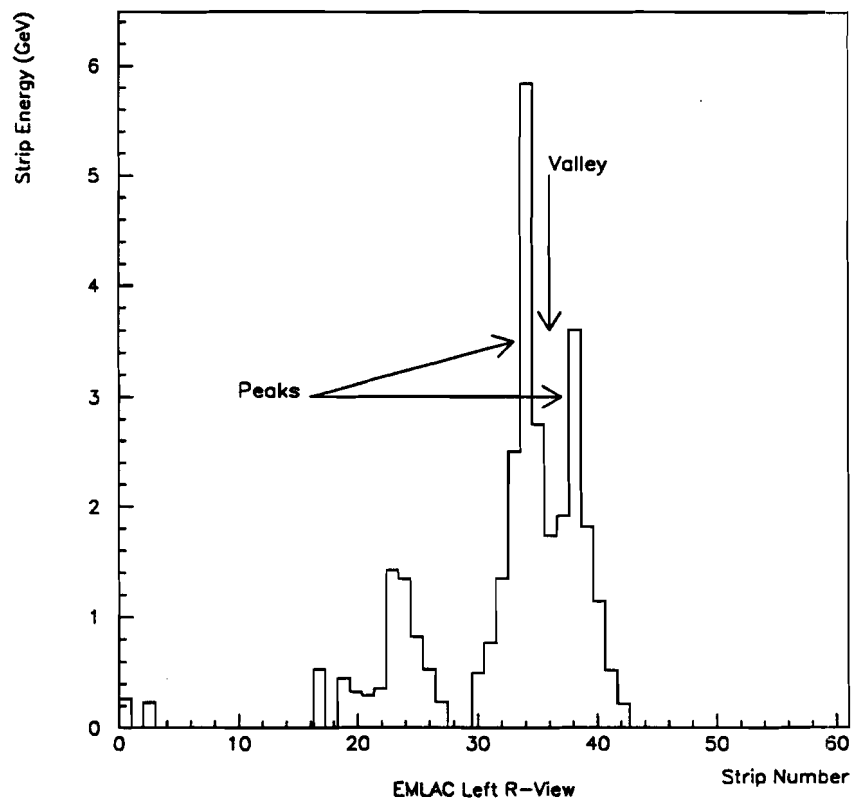


Figure 46: Distribution of Overlapping EMLAC Showers

The gamma position calculation is done in two parts. The first part is the trivial calculation of the center position of the peak strip. The second part is accomplished by a weighting of the position of the gamma within the peak strip based on pulse height values of the strips on either side of the peak strip.

The energy of the gamma is found by minimizing the χ^2 of the fit of the shower shape to the pulse distribution of the group. The number of strips used in the fit depends on the energy in the strips. The energy in the tails of a shower is lost because of the zero suppression employed in the electronics (see Chapter V.3.2 and Chapter VI.7). By fitting the shower shape to the distribution one can estimate what the original energy of the shower was. The amount of energy

in the tails of the shower is computed to be $E_{tail} = E_{fit} (1 - E)$. If the χ^2 is less than 5 the fit is assumed to be reasonable and the fit results are stored, otherwise the summed energy results are stored.

For multiple peak groups the situation is somewhat more complicated. The procedure used is first to split the group into separate showers and then perform the position and energy calculations on a new corrected pulse distribution. In order to split the group a rough position and energy estimate is made for each peak. These estimates are used in finding an energy for the gammas by minimizing the χ^2

$$\chi^2 = \sum_i \left(e_i - \sum_k E_k f_k^i \right)^2 \quad (33)$$

where e_i is the energy in the i^{th} strip, E_k is the true energy of the gamma, and f_k^i is the contribution from the k^{th} shower to the i^{th} strip. Once the energies of the individual gammas are known they are used to calculate the corrected pulse height distributions. After the new strip energies are found the positions of the peaks are recalculated. The energies are then calculated using the same algorithm as the one used one peak group case. At this point it pays to do one more fit to the shower shape using these fitted energies to obtain the gamma position.

VII.2.4 Gamma Correlation and Photon Reconstruction

Once all the gammas are constructed, they are correlated to form the final photons. The correlation procedure, though very complicated in practice, is straightforward in conception. Remember that the G-10 readout boards alternate between radial (r views) and azimuthal (phi views) boards. Therefore a photon will deposit roughly half its energy in each view. Since the shower development is identical for each view the E_{front}/E_{tot} ratios will be the same. The idea is to match a gamma from one view with a gamma in another view that has approximately the same energy and E_{front}/E_{tot} ratio. There are some requirements that make things easier.

Requiring that inner phi gammas only correlate with r gammas that have a radius less than 40 cm and outer phi gammas correlating with r gammas with radius greater than 40 cm is such a requirement. Problems arise, however, when a gamma happens to fall near the inner/outer phi boundary, the octant boundary, or a combination of these boundaries.

The first step in the correlation procedure is to identify which gammas lie near the boundaries. The boundary gamma correlations proceed first since they put the most stringent requirements on the positions of the gammas. For boundary cases the minimum possible correlation would be the boundary gamma with two gammas from the other views. The other possibility would be a two and two correlation in which the view has two gammas near the boundary that can be correlated with two gammas from the other views. If the gammas correlate they are flagged and the reconstructed photons are stored.

After all the boundary correlations are completed the code proceeds with the gammas located away from the boundaries. The three types of correlations attempted are one r to one phi, one r to two phi and one phi to two r . The one to one correlation is simple matching of one r gamma to one inner or outer phi gamma, depending on the radius of the r gamma. Figure 47 shows the correlation between gammas for four photons, two in the inner ϕ and two in the outer ϕ . For the one r to two phi correlation each r gamma is matched with pairs of phi gammas. Once a correlation is found an attempt is made to split the one gamma to the energies of the two correlated gammas. The one phi to two r correlation is essentially the same but with the views reversed (See Fig.48). Whenever a correlation is made the photon information is stored in the photon data banks.

Once all the gammas are correlated, the phi gammas are reconstructed using the information obtained through correlation. This is only done for the phi gammas because there is now a better estimate of the radius of the gamma. Since the fit depends on the width of the phi strips which in turn depend on the radius of the gamma a better fit is obtained using the correlated value

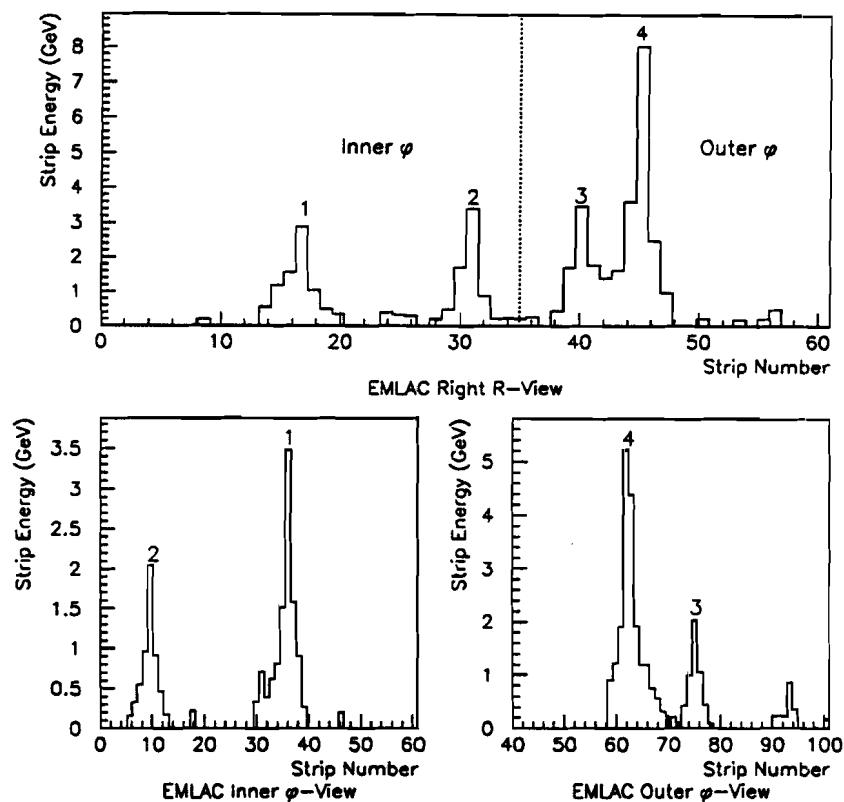


Figure 47: Examples of the Correlation of One r Gamma to One ϕ Gamma

of the radius. After the phi gammas are refitted they are correlated again with the new energy values.

VII.3 Hadron Reconstruction

The purpose of the hadron reconstruction program (HCREC) is to reconstruct the energies, positions, and directionalities of the hadrons coming from an interaction. The program can be divided into five logical steps.

- (1) Group the pads into energy clusters.

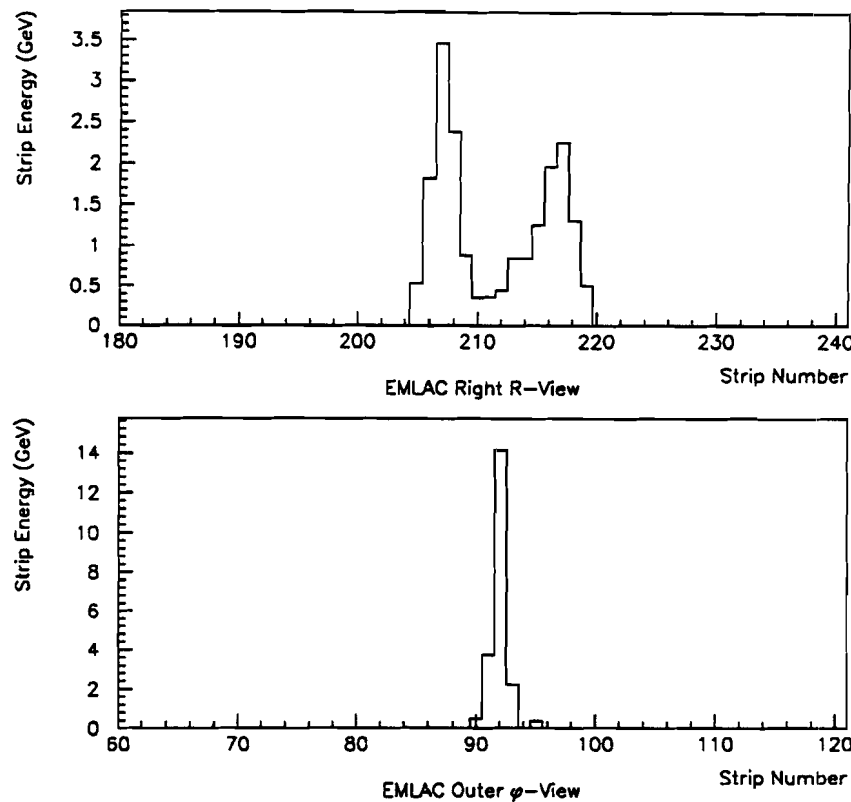


Figure 48: Example of the Correlation of One ϕ Gamma to Two r Gammas

- (2) Subdivide the clusters into hadrons.
- (3) Calculate energy and position of hadrons.
- (4) Correct the energy for shower tail losses.
- (5) Correct the energy for the $\frac{e}{h}$ effect.

Even though the lateral fluctuations of a hadronic shower are quite large there are two shower characteristics that are applicable to the great majority of the showers. One is that about 90% of the shower energy is contained in an area covered by three overlapping hexagons area with the peak pad at the center (See Fig.49). The other is that about 50% of the shower

energy is contained in one or two pads. The three hexagon area contains thirteen pads which are broken down into a central pad with the maximum energy and three classes of neighbors. The Hadron reconstruction package is used to identify hadron showers according to their energy distributions on the HALAC pads^[2].

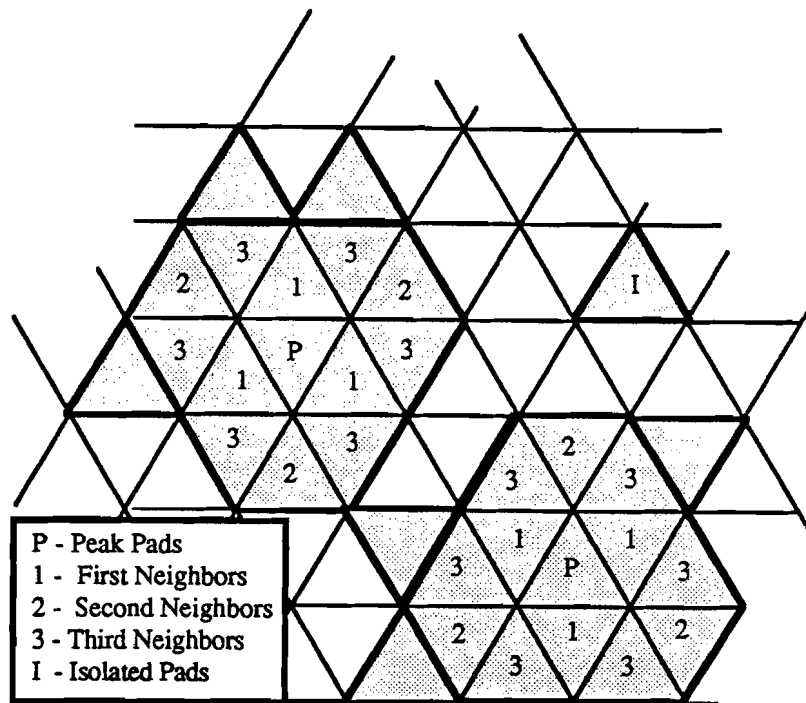


Figure 49: Examples of the Three Hexagon Area Used for Reconstructing Hadrons

VII.3.1 Grouping Pads into Energy Clusters

The pads from the front and back sections of the HALAC are first summed together. A cluster is then defined as a group of two or more contiguous pads with non-zero energy, (energy above threshold). Two pads are considered to be contiguous if they share a side. All the pads

^[2] A. Sinanidas, "A Study of Particles Produced with High Transverse Momentum Single Photons and π^0 's in Hadronic Collisions", *Northeastern University Thesis*, Chapter 5.9, (1989).

that do not satisfy this requirement are called "isolated pads". The reconstruction program uses an energy threshold of 2 GeV for each pad and 5 GeV for the pad with the maximum energy for each cluster.

VII.3.2 Reconstruction of Individual Hadrons from the Clusters

The topology of the majority of the hadrons in the HALAC is relatively simple in the sense that a cluster generally corresponds to one hadron only. A typical single hadron energy distribution consists of a well defined energy maximum close to the shower centroid and an exponentially decreasing energy distribution around the energy peak. With this in mind the requirements used to reconstruct single hadron from the cluster are as follows:

- (1) A cluster have less than twelve pads where three or fewer of these pads have less than 40% of the energy of the maximum pad.
- (2) The energy deposited in the pads surrounding the maximum pad strictly decreases with relative distance.

If these requirements are satisfied and if the number of pads in the cluster is less than eight, an attempt is made to add isolated pads to the cluster that are nearby. Once this is done the calculation of the hadron's properties can proceed. If a cluster fails the criteria for a single hadron then an attempt is made to split the cluster into multiple hadrons. The following procedure was established for searching for additional hadrons:

- (1) The three overlapping hexagon area around a peak pad is searched for any 2nd or 3rd neighbor pad that has energy greater than the average energy of the 1st neighbors. If such a pad is found then the energy of the common neighbors of such a pad and the maximum pad is split.
- (2) The three hexagon area around each secondary peak is searched for any additional hadrons and then the search returns to the neighbors of the primary peak.

(3) Each search assigns only the pads in a peak's three hexagon area to the hadron. Any additional pads are relegated to be isolated pads.

The splitting of the energy contained in the common pads between two peaks is accomplished using a parametrization of the lateral shower shape of a hadronic shower. The splitting is done only if the two peak pads occur in the same three hexagon area. The reason is that the lateral shower distribution indicates that the energy correction is otherwise quite small. The fraction of energy "a_j(i)" from a pad *i*, between two peaks *j* and *k* that is contributed to hadron *j* is calculated as follows;

$$a_j(i) = \frac{Q_j(r_{ij})}{Q_j(r_{ij}) + Q_k(r_{ij})}, \quad (34)$$

$$Q(r_{ij}) = \exp(-5.0) \times \exp\left(\frac{-r_{ij}}{0.4 + 0.25Z/\sqrt{E_j}}\right) + \exp\left(\frac{-r_{ij}}{7(0.4 + 0.25Z/\sqrt{E_j})}\right) \quad (35)$$

where $Q_j(r_{ij})$ is the lateral shower distribution for hadron *j* and r_{ij} is the distance from the center of mass of the common pad *i* to the peak pad of hadron *j*. E_j is the incident energy of hadron *j* in GeV and Z is the Z-axis coordinate, $Z = 0$ is at the front face of HALAC. The Z value selected was that which minimizes the position resolution ($Z_{min} = 10.25$). For hadronic showers in a uniform calorimeter, Monte Carlo analysis indicates that the resolution becomes a minimum at a Z of 15 cm. For the HALAC a Z value of less than 15 makes sense, since showers in general start in the EMLAC. Once the clusters are split into hadrons the energy and the position of each hadron are calculated according to the following formulas;

$$E = \sum_i (E_i^f + E_i^b), \quad (36)$$

$$X = \frac{\sum_i X_i (E_i^f + E_i^b)}{\sum_i (E_i^f + E_i^b)}, \quad (37)$$

$$Y = \frac{\sum_i Y_i (E_i^f + E_i^b)}{\sum_i (E_i^f + E_i^b)}, \quad (38)$$

where X_i , Y_i , E_i^f , E_i^b , are the X and Y position of the pad center and the front and back energies of pad i .

All the remaining pads in the isolated pad bank are reconstructed if their energies are above 5 GeV. The energy of the reconstructed hadron is the same as the pad energy and the reconstructed position is the same as the center of the pad.

VII.3.3 Correct Energy for Shower Tail Losses

The reconstructed energy of a hadron is affected by changes in the readout threshold. Not only is there energy lost because signals in the tails of a shower fail to test over threshold, but the energy resolution varies significantly. The energy of each reconstructed hadron is corrected according to the function:

$$E = E_{had} \cdot \left(\frac{100}{115.74S_0^{-0.283}} \right), \quad (39)$$

where S_0 is the value of the zero suppression threshold in GeV.

This equation was determined from studying the effect of the threshold setting on the reconstructed energy of a 100 GeV calibration beam.

VII.3.4 Energy Correlation between the EMLAC and the HALAC

In the LAC some fraction of the hadronic showers starts in the electromagnetic sector. The incident energy is thus shared between the two different types of calorimeter. The correlation of energy between the calorimeters serves two purposes. It improves the energy and position resolution of hadrons and it also provides additional information about the directionality of hadrons, especially the neutrals.

It is assumed that all of a hadron's energy is contained within a radius of 9.0 cm of its centroid. To combine the output data of the two reconstructors the position of an energy cluster

found in HALAC is projected on the front face of EMLAC, taking into account the focusing. The energy of all the photons that lie within the 9.0 cm radius of the projected position is then added to the hadron energy. This is provided the fraction of the energy deposited in the front section of the EMLAC to the total energy deposited in the EMLAC for a photon is less than 0.6, since a higher ratio is indicative of an electromagnetic shower.

$$E_{Hadron} = C \times (E'_{hc}(f) + E'_{hc}(b) + C_{e/h} \times (E'_{em}(f) + E'_{em}(b))), \quad (40)$$

$$E'_{em}(f/b) = E_{em}(f/b) \times (1 - \frac{C_{em} \times E_{em}(f/b)}{\sqrt{E_{sum}}}), \quad (41)$$

where $E_{em}(f/b)$ is the energy deposited in EMLAC's front/back section, and $E_{sum} = E_{hc}(f) + E_{hc}(b) + E_{em}(f) + E_{em}(b)$. A formula similar to Eq.(41) holds for $E_{hc}(f/b)$.

Using the position information from the front and back sections of EMLAC, along with the position information from the two sections of HALAC, the x-view slope and y-view slope of the hadron track are found.

VII.3.5 Correct Energy for the $\frac{e}{h}$ Effect

The Hadron Calorimeter has a different response to the electromagnetic and hadronic showers. The consequence is that the measurement of the energy of a hadronic shower depends on the relative fraction of the electromagnetic and hadronic components of a the shower. On an event by event basis this fraction can have large fluctuations. To correct for this effect an algorithm developed by the CDHS collaboration is used^[3]:

$$E'_i = E_i \times \frac{1 - CE_i}{\sqrt{E}}, \quad (42)$$

^[3] H. Abramowicz, et. al., "The Response and Resolution of an Iron-Scintillator Calorimeter for Hadronic and Electromagnetic Showers between 10 GeV and 140 GeV", *Nuclear Instruments and Methods*, V180, pp. 429-439, (1981).

where E_i is the uncorrected energy in each front/back section of the LAC and C is a correction factor that is optimized according to the calibration data.

VII.4 TVC Reconstruction

Since a shower spans many strips that may involve several different sections of the EMLAC the algorithm that calculates the TVC time is somewhat involved. TVCs with associated energy less than 4 GeV are discarded. The rest are corrected for slewing based on the energy content of the four channels that supply a TVC. The TVCs for which pedestals exist are corrected; all others have a nominal pedestal subtracted and are flagged. After EMREC has formed its groups, a "group time" is calculated, based on the remaining TVCs associated with the group. The algorithm then proceeds as follows:

- (1) Form clusters for TVC values within a 3σ window of each other. [4].
- (2) Perform an energy weighted average of the TVCs within these clusters.
- (3) Save the two "best" times based on a rating scheme that balances (in order of importance);
 - 1 TVC clusters where then TVCs are pedestal corrected.
 - 2 TVC clusters with the largest number of TVC values.
 - 3 TVC clusters with the most energy.
 - 4 TVC clusters with a time nearest the event time.

A quality word for the two best TVCs is then formed as follows;

$$1000 * (\text{number of TVCs in group}) + (\text{total energy associated with group}) \quad (43)$$

This number is set to be negative if the TVCs are not pedestal corrected. When EMREC forms gammas, the two best times are calculated for each gamma from the contributing groups using a similar algorithm. Finally, in the same manner, the two best times for each photon are calculated from the contributing gammas^[5].

[4] TVCs with and without pedestals are never mixed within a single TVC group, as it confuses error calculation.

[5] E. Prebys, *Private Communication*.

Chapter VIII

Operational Performance of the LAC

There are several quantities which determine the performance characteristics of a liquid argon calorimeter calorimeter.

- (1) The directionality resolution.
- (2) The timing resolution.
- (3) The differences in longitudinal energy deposition by hadronic and electromagnetic particles.
- (4) The position resolution.
- (5) The uniformity of the energy response as a function of position.
- (6) The linearity of the calorimeter response with respect to the amount of deposited energy.
- (7) The energy resolution.
- (8) The detection efficiency for electromagnetic and hadronic showers.

These are all affected by the uncertainties discussed previously. Each item also depends to a large extent on the effectiveness of the software use to reconstruct the showers. Two sets of data were used to study the performance of the LAC. One is the electron beam data acquired during the calibration studies. The other is a subset of events where a photon converted to an electron/positron pair somewhere in the upstream tracking system. A description of these data sets follows after which discussions of the items listed above will commence.

VIII.1 The Calibration Beam

To measure the energy resolution of the LAC, beams of negatively charged particles of known energies were directed at selected areas of the LAC during the second calibration session. As described in chapter IV, the LAC can be moved horizontally by a set of power screws and the central blades of the hadron shield can be removed to allow a vertical dipole in the beamline to change the pitch of the beam. In this manner the beam can be deposited anywhere in the

LAC. The nominal beam energies for this session were chosen to be 25 GeV/c, 50 GeV/c, and 100 GeV/c. The beam momenta were measured by taking a pressure curve with the Cerenkov detector. These momenta along with the values used for the ADC test over threshold are listed in table 8. Data at an energy of 50 GeV/c were taken at 54 points over the face of the detector, most of them in a single quadrant (See Fig.50). There were eight points at 100 GeV/c and two at 25 GeV/c. The beam was constituted of approximately 40% e^- and 60% π^- at a beam energy of 50 GeV/c. The beam intensity was reduced to approximately 1×10^4 sec $^{-1}$ to prevent the pileup of signals. There were also two runs dedicated to the calibration of the HALAC where the beam was almost exclusively pions.

The nominal beam energies for the first calibration session were 200 GeV and 400 GeV. The beam for the first calibration run was made predominantly of pions and protons. While this type of beam is useful for setting the electronics timings and calibrating the HALAC, it is not of much use for calibrating the EMLAC.

Nominal Beam Energy (GeV)	Measured Energy (GeV)	Threshold EMLAC (GeV)	Threshold HALAC(GeV)
25	-	0.168	2.70
50	56.4 ± 0.6	0.168	2.70
100	102.8 ± 0.8	0.168	2.70
200	189 ± 1	0.250	4.02
400	380 ± 3	0.250	4.02

Table 8: Calibration Beam Parameters

VIII.2 Electron Sample from the Run Data

Certain types of events from the data are useful in studying the EMLAC. These are events in which an electron/positron pair are found to originate from the conversion of a photon which quite often comes from the decay of a π^0 . The square of the four-momentum of the track

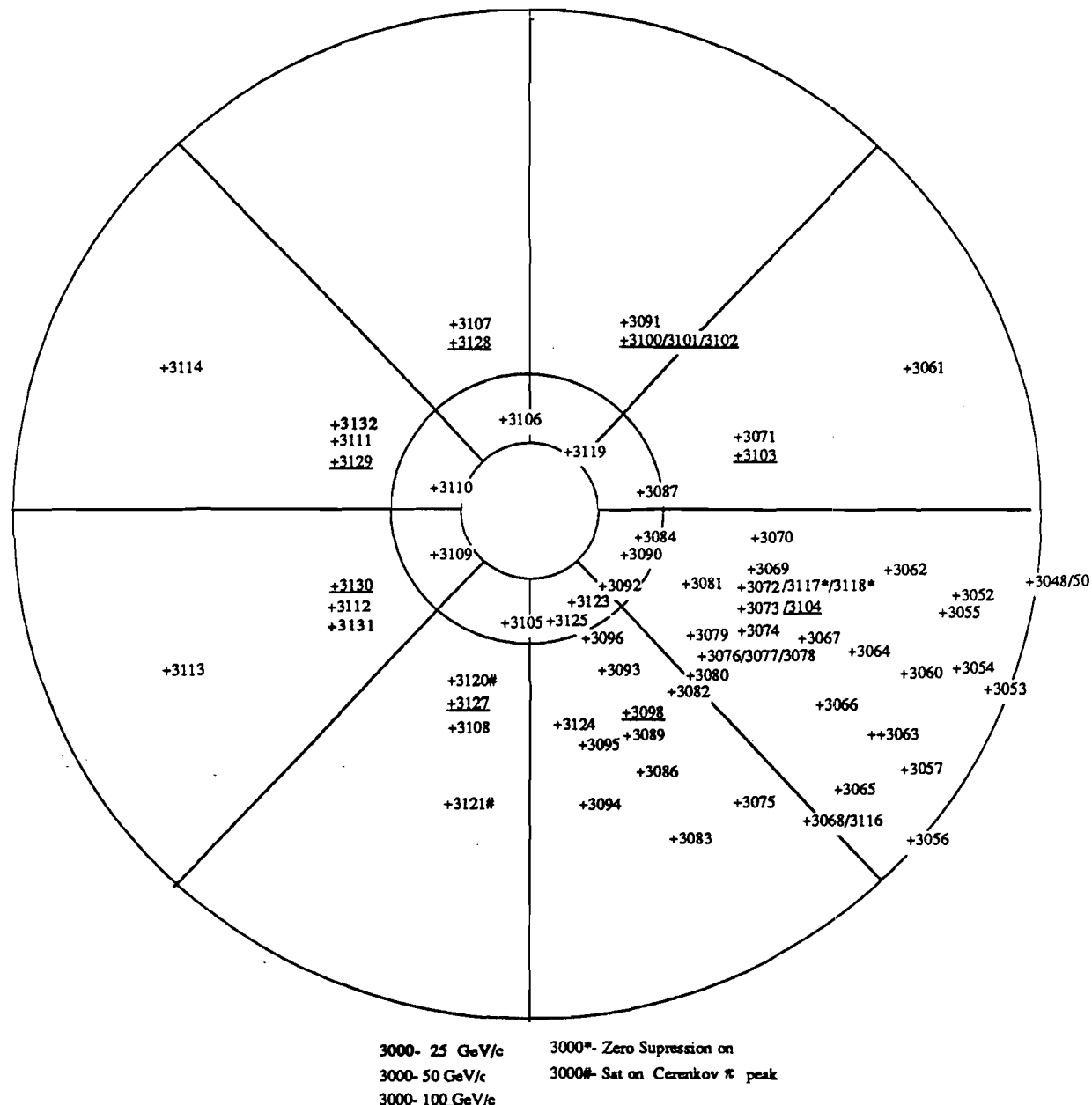


Figure 50: Location of Calibration Points for 25, 50, and 100 GeV/c Electron Beams

pair should be near zero at these energy scales, ie. approximately equal to $2m_e$. The electrons/positrons produced in this manner will be referred to as ZMP electrons. ZMP stands for Zero Mass Pair. For symmetric conversions the opening angle between the tracks downstream of the analysis magnet is proportional to the momentum kick of the magnet and inversely proportional to the momentum of the photon. Without a magnetic field, the opening angle would be of the order of the ratio of the electron mass to the electron momentum and there would be no visible separation of the electron/positron pair. This is evident in single upstream track produced by the pair after the photon converts in the target.

The event signature for a ZMP requires only that a pair of downstream tracks with opposing curvatures have the same slope in the Y view of the PWCs and intersect in the XZ plane near the magnet center (See Fig.51). The ZMPs tend to lie in a band along the X-axis because the analysis magnet deflects charged particles in the XZ plane.

VIII.3 Directionality Resolution

As mentioned in Chapter I, muons from the production target that accompany the beam particles are a major source of background to direct photon production. One way to eliminate events that are triggered by a muon from the beam halo is to make a cut based on the directionality of the shower that produced the trigger. For the EMLAC directionality (D) is defined as;

$$D = r_{front} - \frac{Z_{front}}{Z_{back}} r_{back} \text{ (cm)} \quad (44)$$

where $r_{front/back}$ are the radial positions of the showers in the front and back sections of the EMLAC and $Z_{front/back}$ are the Z positions of the front and back sections of the EMLAC. Tracks coming from the target have directionalities near 0 cm while muons in the halo move essentially parallel to the beamline and have directionalities of 0.7 cm or larger, depending on the "r" position of the showers. The directionality can not be calculated if there is not sufficient energy

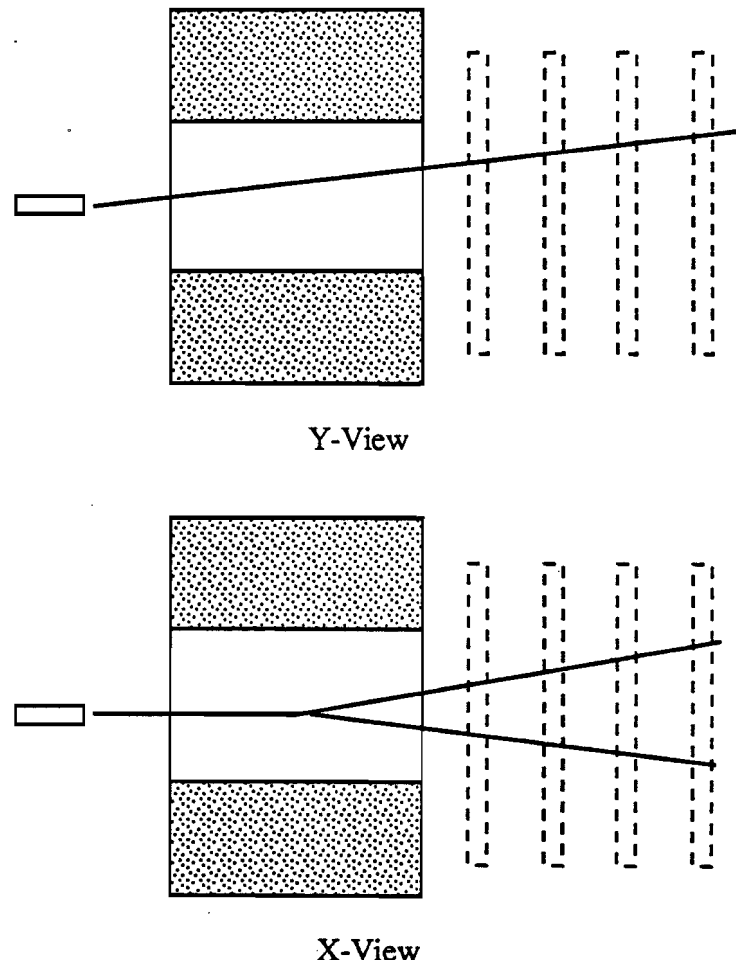


Figure 51: Reconstructed Tracks of a Zero Mass Pair

deposited in the back section of the EMLAC to form a group. In this case the directionality is taken to be 0 cm.

The EMLAC has a directionality resolution sufficient to distinguish between these two values. There is a distance between them of at least 3σ of the distribution in Fig.52. The directionality is calculated in units of centimeters but can be translated into an angular measurement. When done so, the resolution is approximately 10 mr. The actual resolution of the EMLAC is better than indicated here. The distribution in fig.52 was formed by projecting a ZMP track to the Z positions of the front and back sections of the EMLAC, calculating D , and then subtracting D as found by the EMLAC. Thus, the distribution contains uncertainties from both

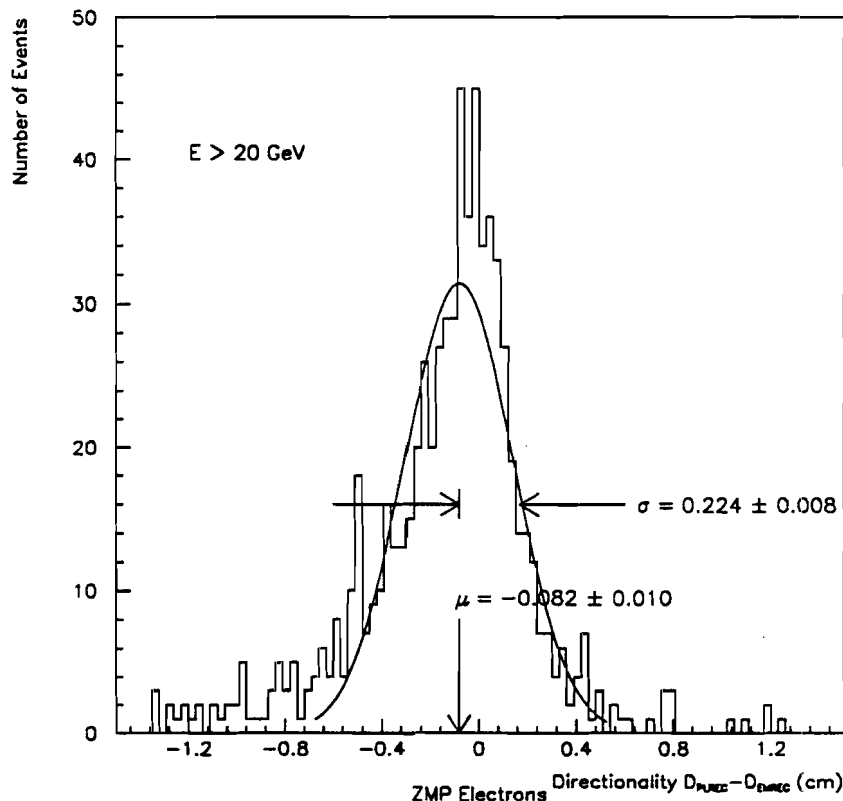


Figure 52: Distribution of EMREC Directionality for ZMP Electron showers Subtracted from the PWC Track Directionality

the PWC track projection and the EMLAC position. As will be seen in a later section, it is the uncertainty in the PWC projection that dominates at the energies of interest.

VIII.4 Timing Resolution

In order to eliminate events that are triggered by muons, but for which the directionality can not be calculated, a timing cut can come to the rescue. Only the EMLAC TVCs are used because the interest is in eliminating false triggers produced by muons. The HALAC is not part of the trigger, therefore its TVCs are not used. In order to determine how effective such a cut is

likely to be one needs to know the width of the timing distribution for showers that are known to be "in time" with their events. In this instance, an "in time" shower was defined by two cuts. One was that the veto wall had not been triggered and the other was that the directionality of the shower be less than 0.4 cm (see section 4). The width of the distribution for showers in time with the event is slightly more than 9 ns (See Fig.53). This is less than half the time interval between beam buckets which is 19.9 ns. This indicates that ones is fairly secure in separating showers that result from particles in different beam buckets.

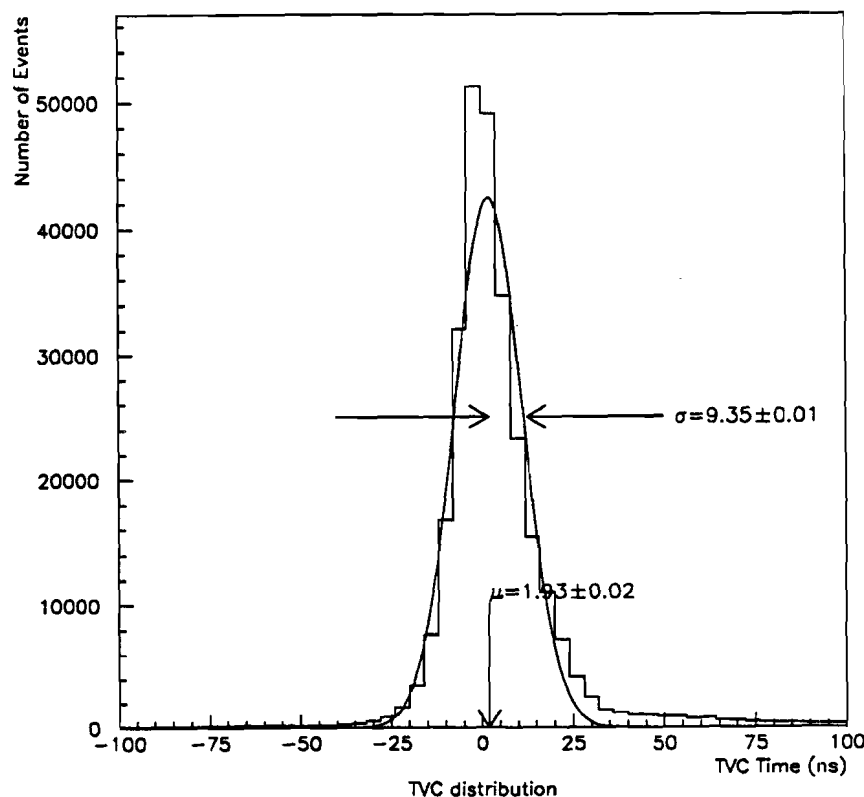


Figure 53: Distribution of TVC Timings for Photon Showers with a Directionality Cut

In a given event most of the first TVC hits tended to be caused by noise. This means that, even at low rates, the second TVC hit is still important (see Chapter V.3.1). With such a high noise level it is vital to know what the efficiency of the two hit TVC system is. Unfortunately, the efficiency of the TVCs is surprisingly low. With a turn on of about 3 GeV, the TVCs attained a maximum efficiency of only about 90%.

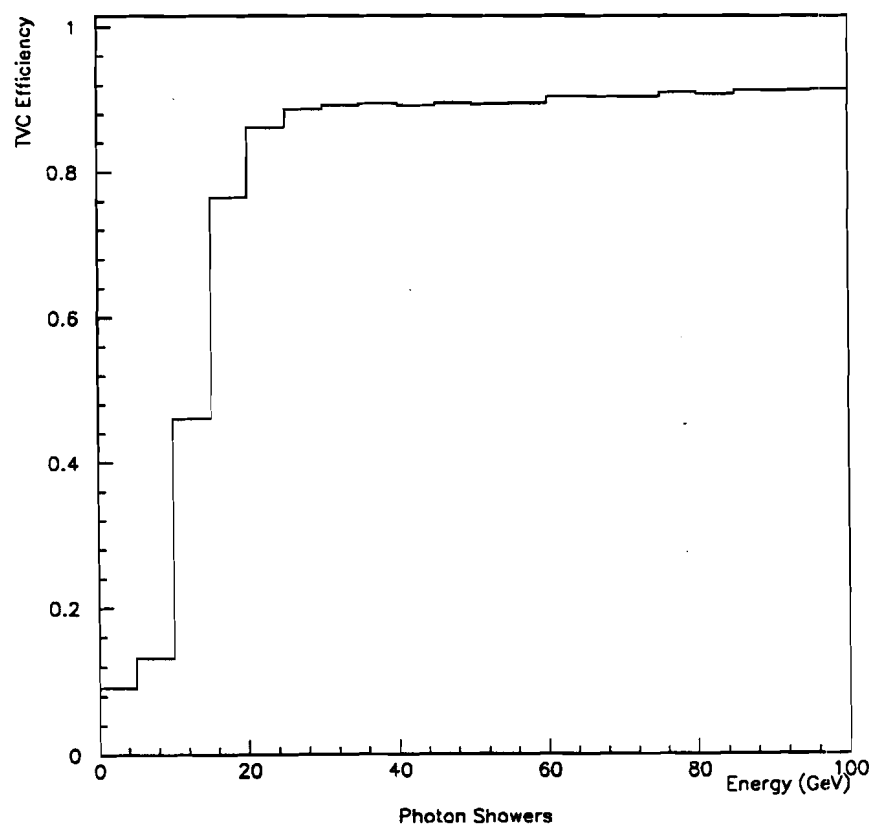


Figure 54: TVC Efficiency for Photon Showers as a Function of Energy

Now that the timing and directionality resolutions are defined, it is of interest to see how effective any related cut would be in eliminating events that are triggered by muons. Each cut taken by itself would not be completely effective in removing the muon contamination. Muons which showered only in the front section of the EMLAC would have a directionality of zero and would pass the directionality cut. The TVCs are only 90% efficient so that 10% of the muon triggers would not be eliminated by the timing cut. Taken together, the two cuts are most effective in removing muon triggered events.

The following plot displays the directionality versus time of the leading p_T particle of an event. The plot has been limited to particles with a p_T value greater than 4.0 GeV, the main region of interest in direct photon physics. The plot clearly shows two distinct populations of particles. The photon population is centered at about 5 ns in time and 0 cm directionality. The muon population is well removed to negative times and positive directionalities. The nominal analysis cuts have been superimposed on the plot. These cuts are placed at distance of nearly 2σ in directionality and 3σ in time from the center of the photon population. As can be seen these cuts should effectively eliminate the muon triggered events with little effect on the photon triggered event statistics.

VIII.5 Particle Identification Using the EMLAC E_{front}/E_{total} Ratio

It is expected that hadronic and electromagnetic types of particles can be distinguished from one another by virtue of their different shower patterns. In the EMLAC, electromagnetic showers will tend to start early and deposit most of their energy in the front section of the calorimeter. A distribution of E_{front}/E_{total} for electromagnetic showers should peak at relatively large value near one. Hadronic showers, on the other hand, will start in the EMLAC only 65% of the time, since the EMLAC is only one interaction length thick. One would then expect that the distribution of E_{front}/E_{total} for hadronic showers would have a large peak near zero and a relatively flat distribution from zero to one.

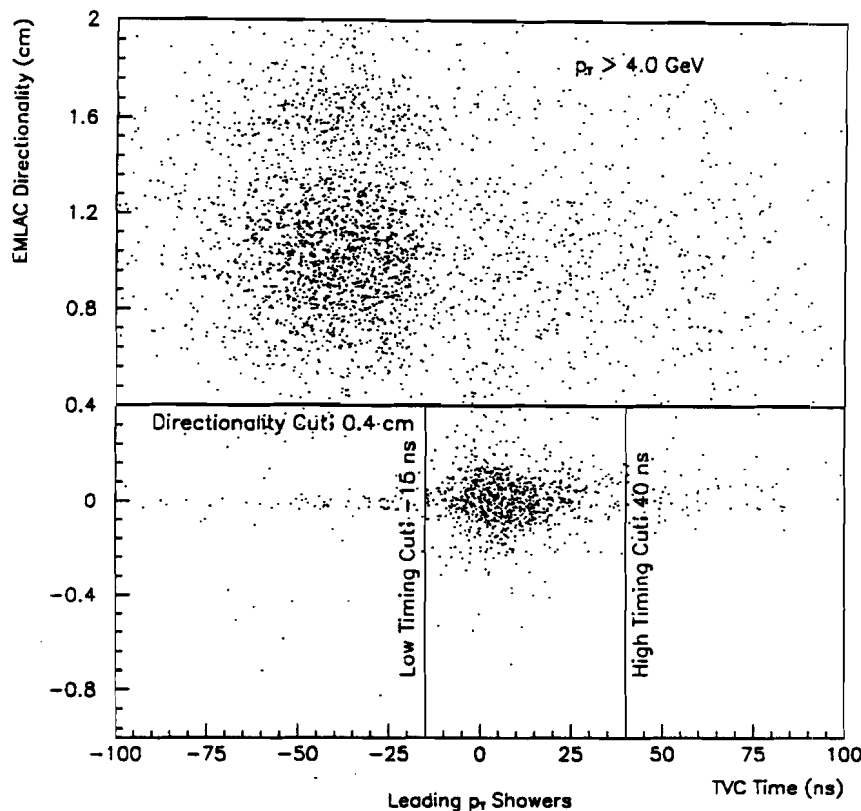


Figure 55: Plot of Directionality versus TVC Time for the Leading p_T Shower of an Event with a p_T Greater than 4 GeV

Two clean sets of data are needed to check this supposition. ZMP electrons provide a clean set of electromagnetic showers. A clean set of hadronic showers can be obtained by selecting those that match tracks from the decay of a particle such as the K_S^0 . The reconstruction of these tracks is accomplished by selecting a pair of tracks with a vertex inside the analysis magnet. The momentum for these tracks is recalculated because they only see part of the magnetic field. Cuts are then made on acceptance and the p_T asymmetry of the pair and the tracks are required to be of opposite charge.

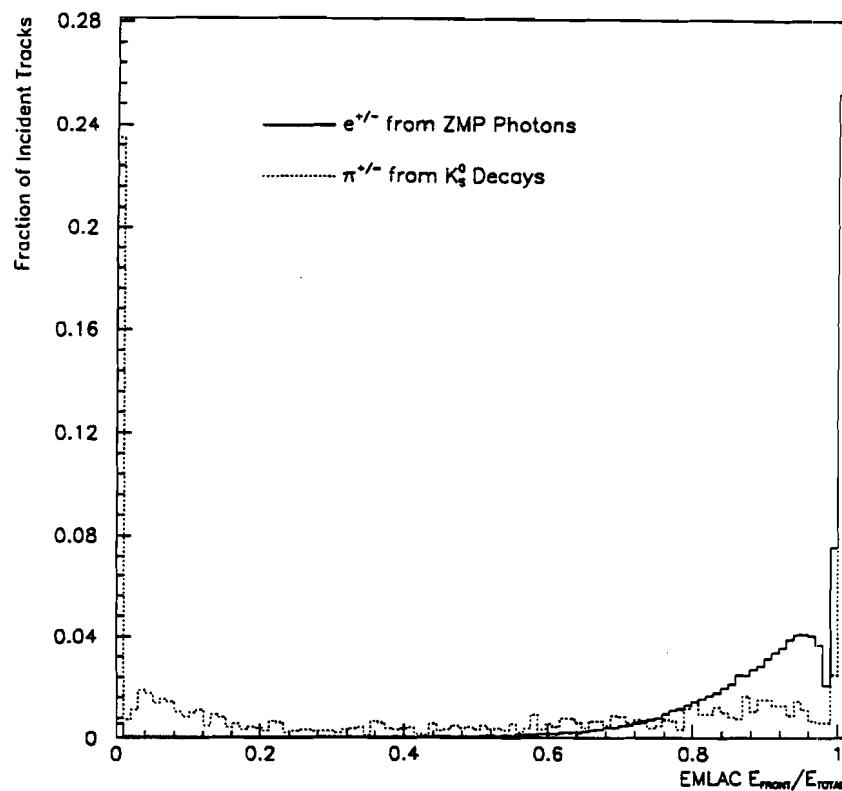


Figure 56: Comparison of E_{front}/E_{total} Distributions for ZMP Electrons and Pions from K_s^0 Decays

Fig.56 is a superposition of the E_{front}/E_{total} distributions for these two sets of data. The distribution for the ZMP data increases as E_{front}/E_{total} increases and has a large peak at one. The dip in this distribution at 0.98 is a result of zero suppression. Zero suppression is artificially shifting E_{front}/E_{total} , for showers that barely penetrate in to the in the back section of the calorimeter, up to one. The pion data has a large peak at zero and a flat distribution over the rest of the range. There is a smaller peak at one that may be due to a small electron contamination of the sample. For analyzing data a cut on E_{front}/E_{total} at a value of 0.4 should

be most effective. Virtually all of the electromagnetic showers have a value that is larger than this and more than 60% of the hadronic showers have a value which is lower.

VIII.6 XY Position Resolution

Position resolution is important for three reasons. One is that it affects the determination of the p_T of neutral particles where large uncertainties can dramatically affect the determination of production cross sections which fall steeply with increasing p_T . It also has a role in determining the mass width of particles such as the π^0 where the reconstructed mass depends on the relative separation of the π^0 's decay photons. The mass width of the π^0 is a key indicator of the energy resolution of the EMLAC. The third reason is that it is a limiting factor in the ability to match reconstructed tracks with showers, which is important for particle identification. The results presented here are for isolated shower position resolutions and while they are indicative of the ability to separate overlapping showers they are not a direct measure of this ability. Separating overlapping showers is a much more difficult subject and is not treated here.

VIII.6.1 EMLAC XY Position Resolution

The method used to extract the X and Y position resolutions of the EMLAC was to subtract the projected position of a ZMP track from the calculated position of the nearest shower in the EMLAC. The width of the resulting distribution is a measure of the resolution of the PWCs and the resolution of the EMLAC added in quadrature (See Fig.57).

Monte Carlo methods can provide lower limits on the resolutions of both the track position from the EMLAC and the track projected position from the PWCs. For the EMLAC the position resolution lower limit was found to be $\sigma_{x,y} = 0.07$ cm. The Monte Carlo PWC resolution of the track projection was found to be $\sigma_{x,y} = 0.16$ cm. By properly subtracting the PWC resolution from the combined resolution the position resolution of the EMLAC can be established. These are $\sigma_x(EMLAC) = 0.06$ cm and $\sigma_y(EMLAC) = 0.08$ cm. This is in reasonable agreement with

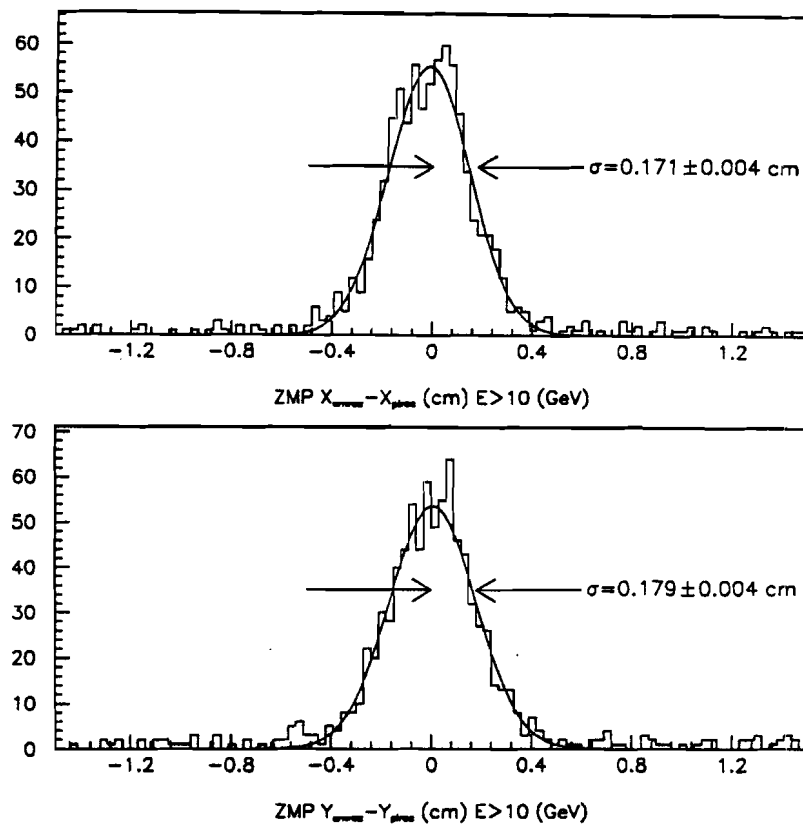


Figure 57: Plots of EMREC Shower Position Minus the PWC Projected Track Position for ZMP Electrons with Energy Greater than 10 GeV/c

Monte Carlo predictions. The discrepancy between the X and Y resolutions is probably due to the fact that the ZMPs range in Y is limited compared to X because they lie in a band along the X-axis.

In fact, the position resolution of the EMLAC is energy dependent. This is a result of the various energy thresholds of the detectors and the multiple scattering of a charged particle from material in the path of the particle. At lower energies the reconstructors have a harder time accomplishing fits of the data and the changes in the particle's path as a result of scattering are more dramatic (See Fig.58). From Monte Carlo results one sees that above 10 GeV the EMLAC

position resolution is comparable to or better than that for tracking. The difference between data and Monte Carlo below 10 GeV is due to an insufficient amount of material between the target and the LAC in the Monte Carlo. The discrepancy in the Y resolution is probably from the fact that the Monte Carlo events were generated along a single radius close to the X-axis. This resulted in a very narrow range of Y values over which to evaluate the position, which artificially narrows the position difference distribution.

From the above discussion one can conclude that the X and Y resolution for the EMLAC are the same and that the Monte Carlo can reproduce the position resolution of the data. The EMLAC position resolution as a function of energy is then best parametrized as:

$$\sigma_{x,y} = 0.024 + \frac{1.53}{E} \text{ (cm); } E \text{ in GeV.} \quad (45)$$

The uncertainties in p_T and rest masses also depend on the uncertainty in the Z position of the LAC to a limited extent. The uncertainty in Z arises from accuracy limits in the measurement of its position and also from cryogenic effects. The contraction of the calorimeter under cryogenic conditions causes a change in the focal length of the strips and pads. This produces changes in the effective Z position at which showers are reconstructed. Here again ZMP tracks are useful. By projecting them to several different planes in Z and finding the distance between the projected position and the reconstructed EMLAC position then the plot of the width of these distributions versus Z position can be fit by parabolic curve whose minimum occurs at the effective Z position of the EMLAC. This position is found to be 900.66 ± 0.26 cm (See Fig.59).

VIII.6.2 HALAC XY Position Resolution

The position resolution for the HALAC is expected to be substantially worse than the EMLAC because of the much larger lateral fluctuations of hadronic showers and because the hadrons have to pass through the EMLAC where they can be scattered. As a consequence the positions of showers in the HALAC are generally only used to match showers in the EMLAC.

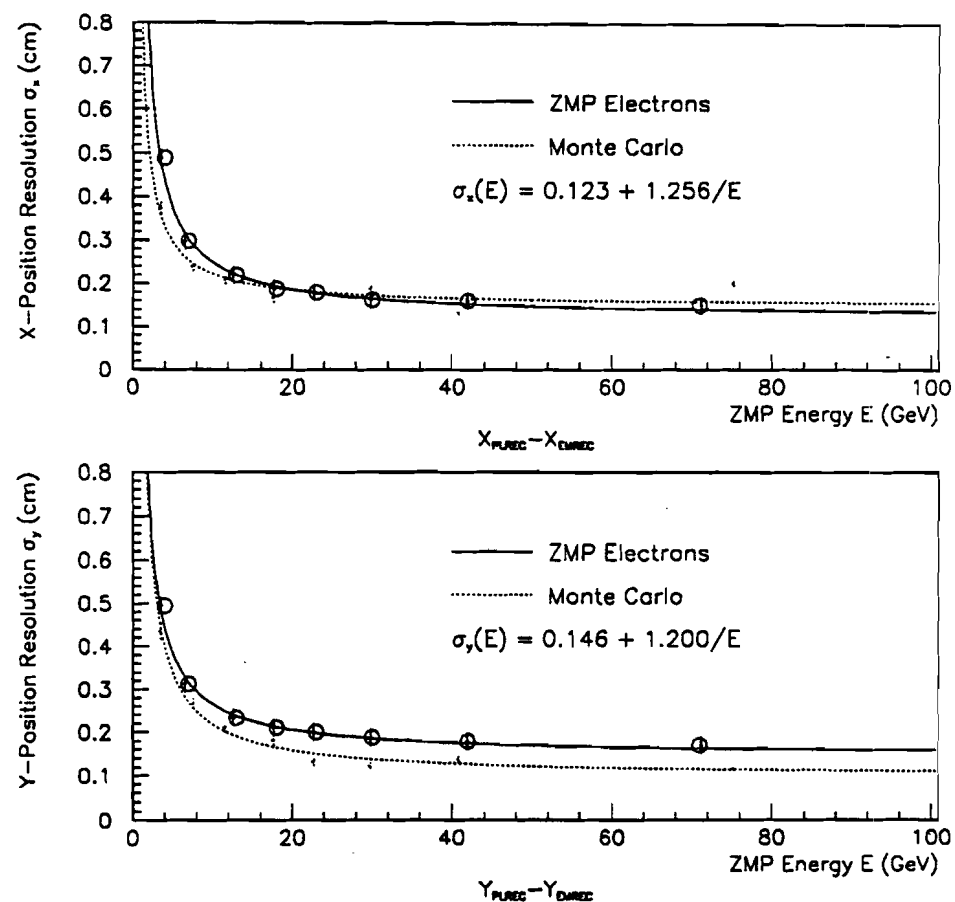


Figure 58: Plot of the X,Y Position Resolutions for ZMP Electrons as a Function of Energy

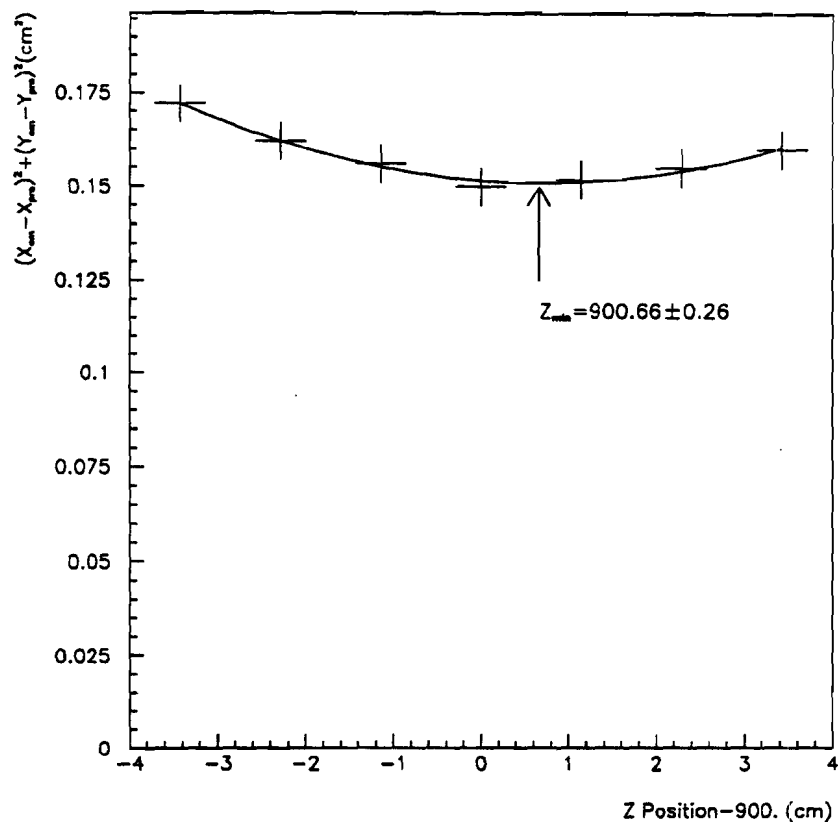


Figure 59: Plot of the Distribution Width for the Square of the Distance Between the Projected ZMP Track Position and the EMLAC Shower Position versus the Z Position of the Projection Plane

To find the position resolution of the HALAC, the position of a shower in the HALAC was projected to the front of the EMLAC and the result subtracted from the position of the shower in the EMLAC (See Fig. 60). The resolution of the HALAC was found to be about 3 cm.

VIII.7 Uniformness of the Calorimeter's Energy Response

If a calorimeter does not respond uniformly to showers with the same energy but with different positions, then the global energy resolution will markedly deteriorate from what the

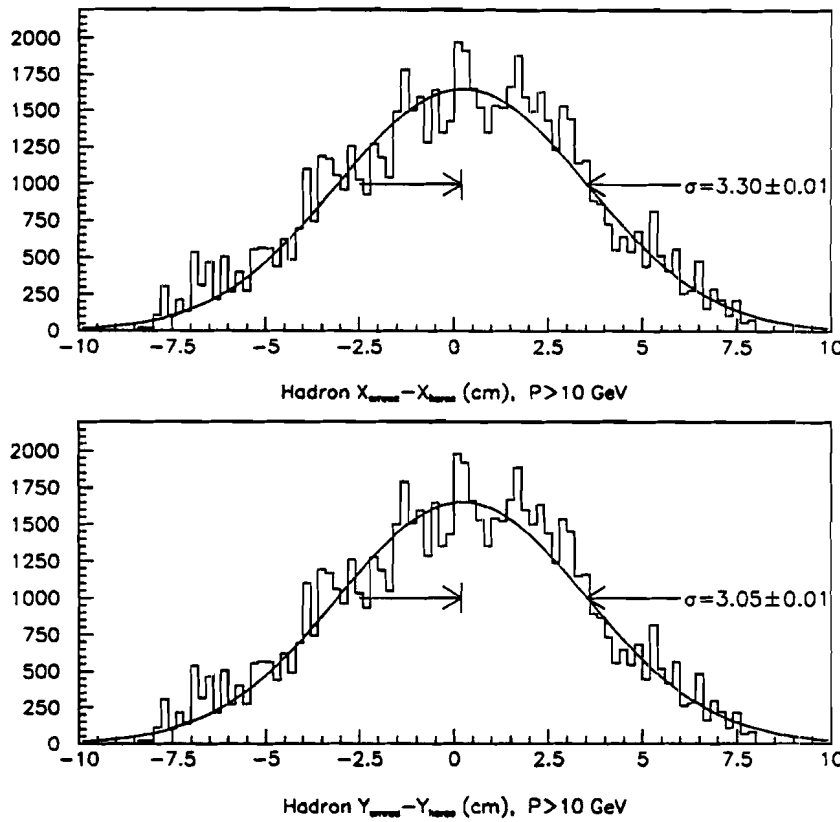


Figure 60: Plots of the Projected HCREC Shower Position
Subtracted from the EMREC Shower Position for
Hadrons with Energy Greater than 10 GeV/c

local energy resolution is found to be. The calibration data provides a means for examining the uniformity of the response of the calorimeter. This data has fifty nine runs with a 56 GeV/c beam at different points in the detector. The width (σ) of the distribution of the mean values (μ) of the reconstructed energies at these points is a measure of the response uniformity. For the EMLAC the value of σ/μ is 1.5% (See Fig.61). For the HALAC this number is closer to 4%.

VIII.8 Linearity of Measured Energy

It is important that the energy measured by a calorimeter vary linearly with the energy of

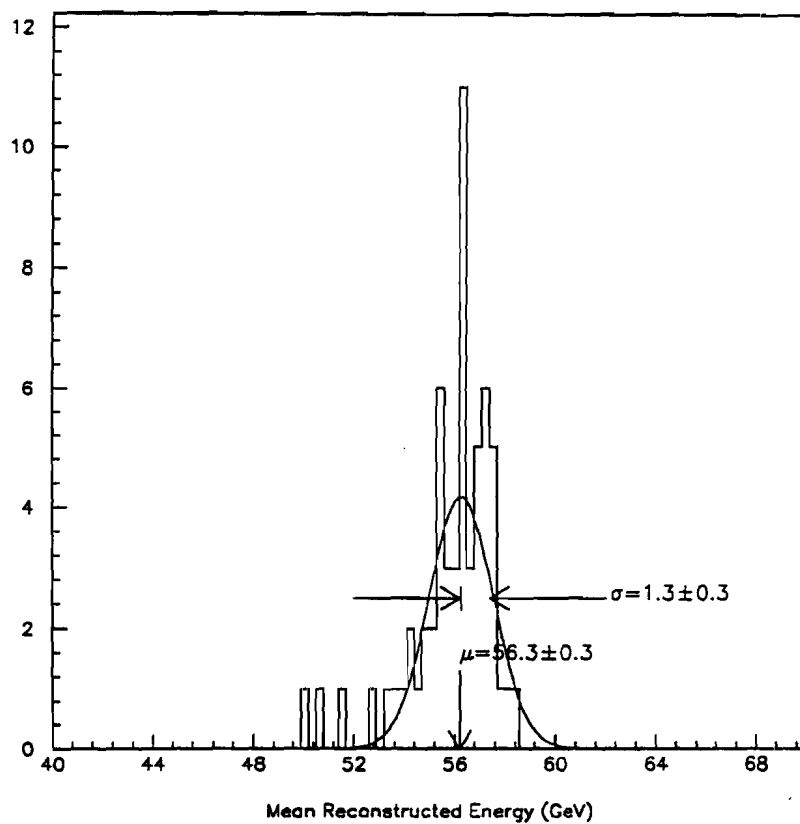


Figure 61: Distribution of the Mean Reconstructed Energies for the LAC Calibration Points

the incident particles. If it did not, then determination of cross sections would be much more difficult, especially if the calorimeter output was not some monotonic function of deposited energy. For example, given a γ and a π^0 of the same incident energy and p_T , the reconstructed energies would be different because the π^0 decays into two lower momentum photons. This would result in a systematic shift in the p_T scale between π^0 's and γ 's. Even small shifts in p_T will produce a large uncertainty in the absolute normalization of the cross sections because of their steep fall with increasing p_T . Figure 62 shows the linearity of the EMLAC in response to

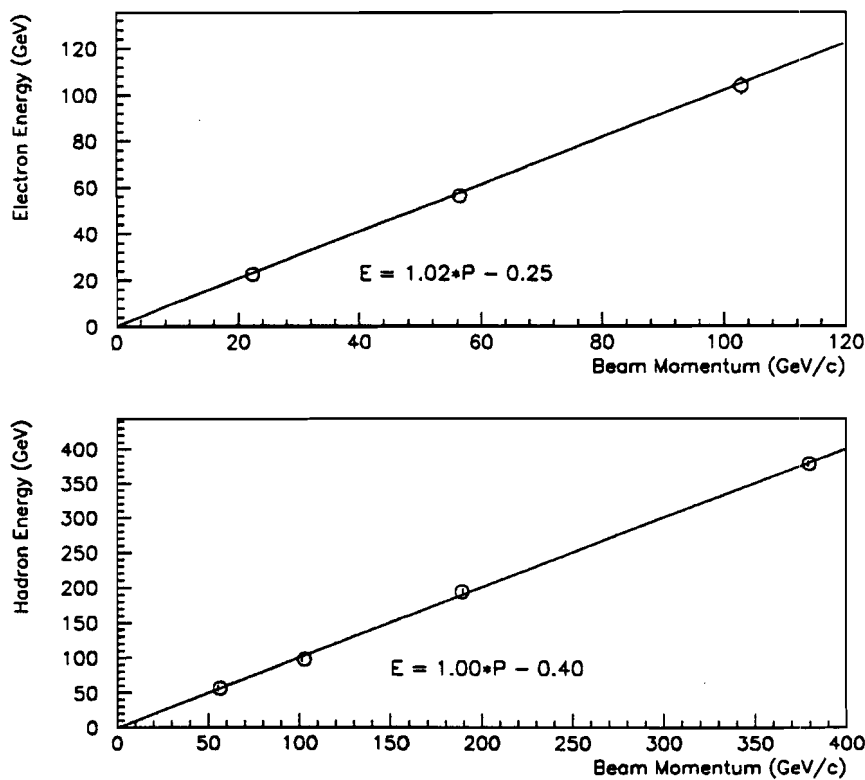


Figure 62: Plot of LAC Energy versus Calibration Beam Momentum

the electron calibration beam. As can be seen from the fit the response deviates from $E = P$ by about 2%. A similar analysis shows no measurable deviation for the HALAC.

The calibration data agrees with the ZMP data for energies less than 75 GeV in the EM-LAC(See Fig.63). The deviation from $E = P$ for energies higher than this may be due to combination of poor statistics contaminated by hadrons, but the E/P and E_{front}/E_{total} distributions for this energy range do not seem to support this hypothesis. What may be more likely is that one is seeing a significant breakup of high energy electrons into multiple showers due to bremsstrahlung, Compton scattering, or some other process occurring in the dewar wall. The

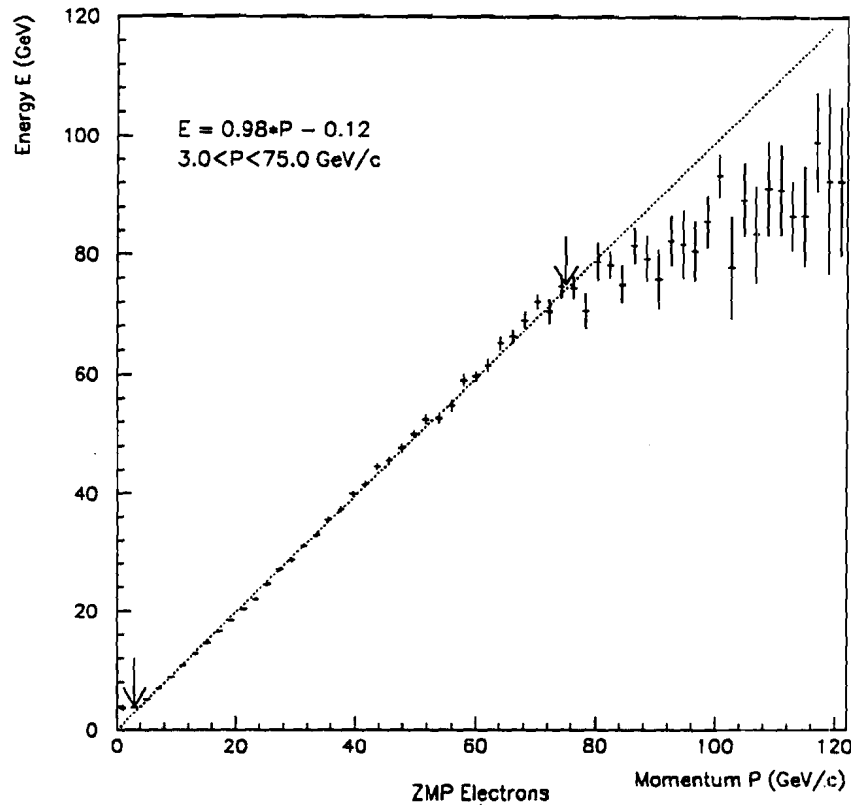


Figure 63: Plot of Energy versus Momentum for ZMP Electrons

electron would then be reconstructed as multiple particles with a fraction of the initial energy of the electron.

VIII.9 Results of E/P Analysis

The ratio of the energy of a charged particle as measured by the calorimeter to its momentum as measured by the tracking system (E/P) is a useful quantity. It can be of use in electron/hadron discrimination, when one only considers the energy deposited in the EMLAC. It also provides a consistency check between the LAC and the tracking system since E/P should

equal one for charged particles within the combined resolution of the tracking system and the calorimeter.

ZMP electrons are a convenient source of tracks to study E/P for the EMLAC. At low energies a significant portion of an electron's energy is deposited before the EMLAC and so E/P is less than one. Additionally, some of the energy deposited in the back of the EMLAC is lost as a result of strips in falling below the zero suppression threshold. This is not corrected for in the reconstruction program because it depends sensitively on the starting position of the shower, which is largely unknown. The loss of energy before the LAC can be simulated by using electrons in the E-706 Monte Carlo and keeping track of where the energy is deposited by a number of electron showers at different energies. A fit to these results has been superimposed on Fig. 64, which is a plot of E/P for ZMP electrons.

The Monte Carlo results agree with the ZMP data in the energy range below 5 GeV and from 30-75 GeV. The sharp upward turn of the curve below 4 GeV is due to the misreconstruction of showers. For particles with energies in this range the tail fluctuations become extremely important. These fluctuations will determine whether or not the shower will be reconstructed. These particles either deposit all of their energy in a very few strips or conspire with amplifier fluctuations to pass the 3 GeV threshold in EMREC. Once over threshold the reconstructed energy is nearly always higher than the incident energy because of tail corrections.

In the 5-30 GeV range the separation between Monte Carlo and ZMP data is an artifact of zero suppression in the back. If one plots E/P only for electrons with a minimum energy of 1 GeV in the back section then the Monte Carlo data agrees with the ZMP data in this region. Clearly zero suppression is playing some role here but there may be several interconnected effects at work. At present the reconstructor does not compensate for energy lost before the calorimeter. Every shower is treated as a photon. This can lead to a further reduction in energy because the tail correction will be done as if the electron were a photon of lower energy. By selecting electrons in this manner one is preferentially taking those that start showering late.

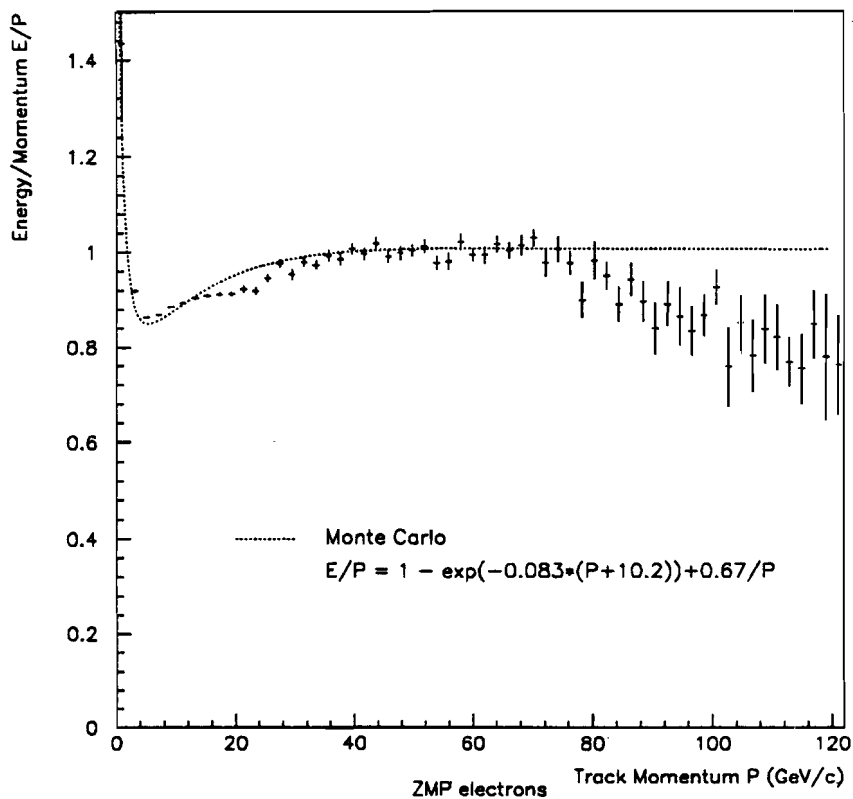


Figure 64: Plot of Shower Energy Divided by Track Momentum versus Track Momentum for ZMP Electrons

This means that less energy is lost both in the back section due to zero suppression and in the material in front of the calorimeter and consequently the tail correction is improved. Exactly how much of the lost energy each of these effects accounts for has yet to be determined.

The deviation of E/P from one at energies above 75 GeV has already been seen in the linearity plots. Preliminary attempts to see if the effect is reproduced by the Monte Carlo show only an $E = P$ trend which would indicate that this is not a calorimeter effect. This effect may be due to a $1/p$ error in the tracking system. The track reconstruction software uses only a thin lens approximation to calculate the track momentum. It may be that this algorithm is

not adequate for high momentum tracks where the resolution of the tracking system starts to become significant. To test this hypothesis, additional Monte Carlo analysis that includes charge particle tracking needs to be done. Alternatively an improved momentum algorithm could be implemented and E/P plotted using the new momentum estimate.

VIII.10 Energy Resolution of the LAC

The square of the energy resolution for a calorimeter ($\sigma^2(E)$) can, in general, be written as the sum of four terms:

$$\sigma^2(E) = \sigma_{it}^2(E) + \sigma_{in}^2(E) + \sigma_{gn}^2(E) + \sigma_{cn}^2(E). \quad (46)$$

In Eq.46, $\sigma_{it}^2(E)$ represents the intrinsic resolution of the device discussed in Chapter III. The remaining three terms are due to various sources of electronics fluctuations. There is a term due to the summed incoherent noise of the detector channels ($\sigma_{in}^2(E)$), which has its source in the signal fluctuations caused by the channel capacitances. There is a term due to the summed fluctuations of the gains ($\sigma_{gn}^2(E)$) for the channel amplifiers. The last term is from the coherent noise ($\sigma_{cn}^2(E)$) of the calorimeter.

The $\sigma_{it}^2(E)$ term varies linearly with E . The $\sigma_{in}^2(E)$ term depends on E in the sense that the number of strips or pads that comprise a shower varies with energy. The same is true of $\sigma_{cn}^2(E)$, except that, if the coherent noise source is from crosstalk between channels, this term may vary as E^2 . The $\sigma_{gn}^2(E)$ term varies as E^2 because the gains are a multiplicative factor in the conversion of energy rather than an additive one like $\sigma_{in}^2(E)$.

VIII.10.1 The Contribution of Incoherent Noise to the Energy Resolution

To determine the amount of incoherent noise in a shower it is useful to know the number of strips or pads in a shower as a function of energy. In the EMLAC the number of strips in a Electromagnetic shower of a given energy differs depending on whether it is in the inner or

outer ϕ region of the EMLAC (See Fig.65). Parametrizations of ZMP data for the number of strips per shower (N) versus energy (E) have yielded for inner ϕ :

$$N_S \approx 72(1 - \exp(-0.014(E + 9.6))), \quad (47)$$

and for outer ϕ ,

$$N_S \approx 77(1 - \exp(-0.011(E + 6.6))). \quad (48)$$

The incoherent noise, which is proportional to the number of channels spanned by the shower and the signal fluctuations for an individual channels, can then be written as:

$$\sigma_{in}^2 = N_S(E) \times \sigma_{pd}^2. \quad (49)$$

Knowing the strip noise (see Chapter VI) makes the extrapolation for the total noise in a shower of a given energy straight forward and indicates a maximum of 728 MeV for a shower. One might have expected a radial dependence in the parametrization of N_S in the outer ϕ region. It was not possible to see this because the statistics diminish rapidly with increasing radius.

Incoherent noise has greater importance in hadronic showers because of the larger channel capacitance of the HALAC pads and lower sampling ratio of the HALAC. As can be seen in Fig.66, the number of pads in a shower follows an exponential curve as a function of energy up to an energy of 50 GeV. After this point the large lateral fluctuations of hadronic showers combine with low statistics to give erratic results. Parametrization of hadronic data yields the equation,

$$N_P = 4.2(1 - \exp(-0.057(E - 4.4))). \quad (50)$$

This equation is the same for the front and back sections. To find the total pedestal noise in a shower the front and back sections must be added together in quadrature because of their different pedestal widths. The maximum amount of noise predicted by the parametrization is 3.5 GeV.

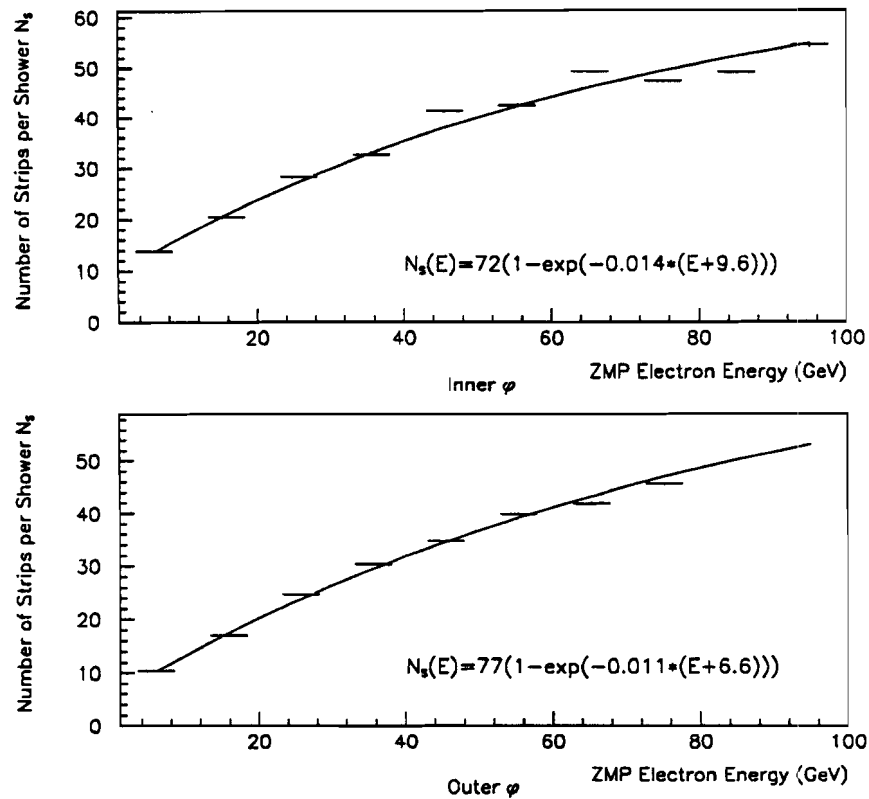


Figure 65: Plots of the Number of Strips in a ZMP Shower versus Energy for the Inner and Outer ϕ regions of the EMLAC

VIII.10.2 Intrinsic Resolution of the EMLAC

Because the EMLAC has interleaved r and ϕ charge collection cells there are in effect two measurements of the energy deposited by a particle. By plotting the value of the energy deposited in the r -view (E_r) minus the energy deposited in the ϕ -view (E_ϕ) for several ranges of energy one can get a handle on the intrinsic resolution of the EMLAC. The width of the resulting distributions are dependent only on the intrinsic resolution, the noise in the gains, and the incoherent noise of the calorimeter. Any external coherent effect, such as the momentum spread of the calibration beam, is subtracted out in $E_r - E_\phi$. Furthermore, given that $\sigma_{in}(E)$

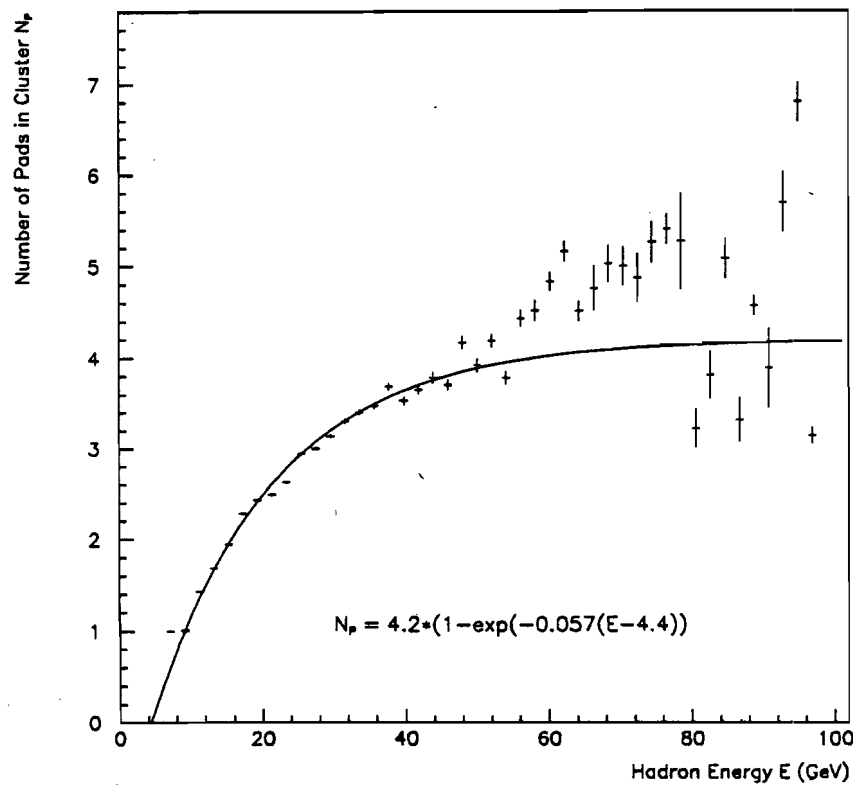


Figure 66: Plots of the Number of Pads in a Hadron Shower versus Energy the HALAC

is relatively constant over the energy range of interest, it is not unreasonable to assume it to be constant and the equation for the square of the energy resolution can be written as:

$$\sigma^2(E_r - E_\phi) = \sigma_{in}^2 + \sigma_{it}^2 + \sigma_{gn}^2 = a + bE + cE^2. \quad (51)$$

A quadratic function can then be fit to a plot of $\sigma^2(E_r - E_\phi)$ versus energy.

A preliminary estimate of the intrinsic resolution can be had by fitting the results from the calibration data. With only three points to fit a curve, it is not practical to try fitting anything other than a linear equation. From this the overall energy resolution is indicated to

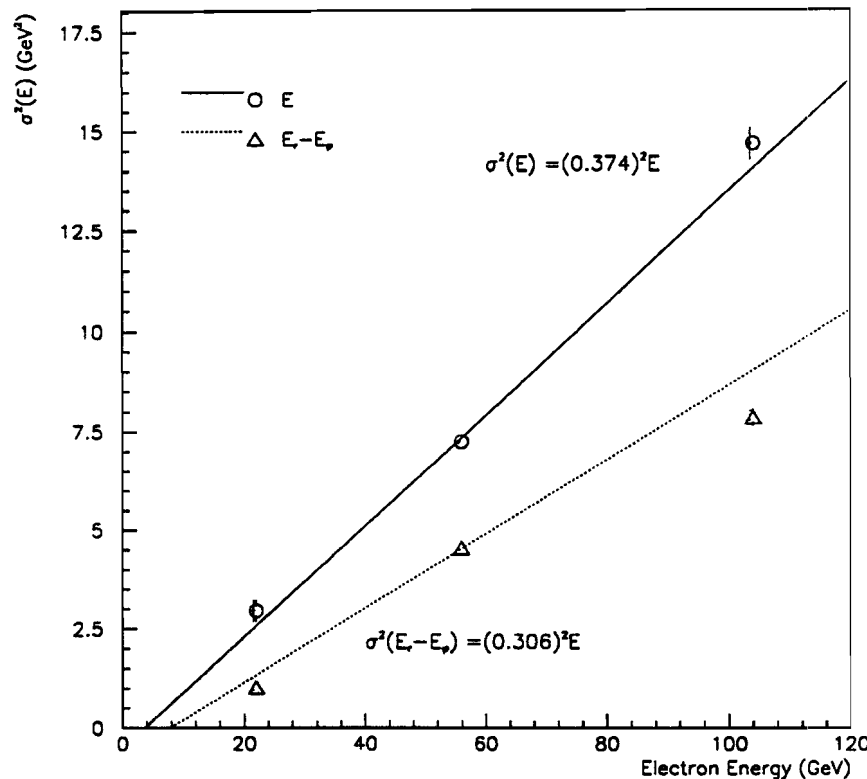


Figure 67: Plot of $\sigma^2(E_r - E_\phi)$ vs Energy for Calibration Beam Electron Showers in the EMLAC

be $37\%/\sqrt{E}$ with an intrinsic resolution of $31\%/\sqrt{E}$ (See Fig.67). Besides the abnormally high intrinsic resolution, these fits have unphysical negative Y-intercepts.

If this analysis is carried over to the run data a different picture emerges. Showers from reconstructed π^0 's and ZMPs are good candidates with which to study the energy resolution of the EMLAC. Fig.68 shows $\sigma^2(E_r - E_\phi)$ versus energy for these two sets of data. Quadratic fits to the data result in an intrinsic resolution of $14\%/\sqrt{E}$ for photons and $21\%/\sqrt{E}$ for electrons. The gains terms in each fit is of the order of 2-3% which is consistent with expectations. The

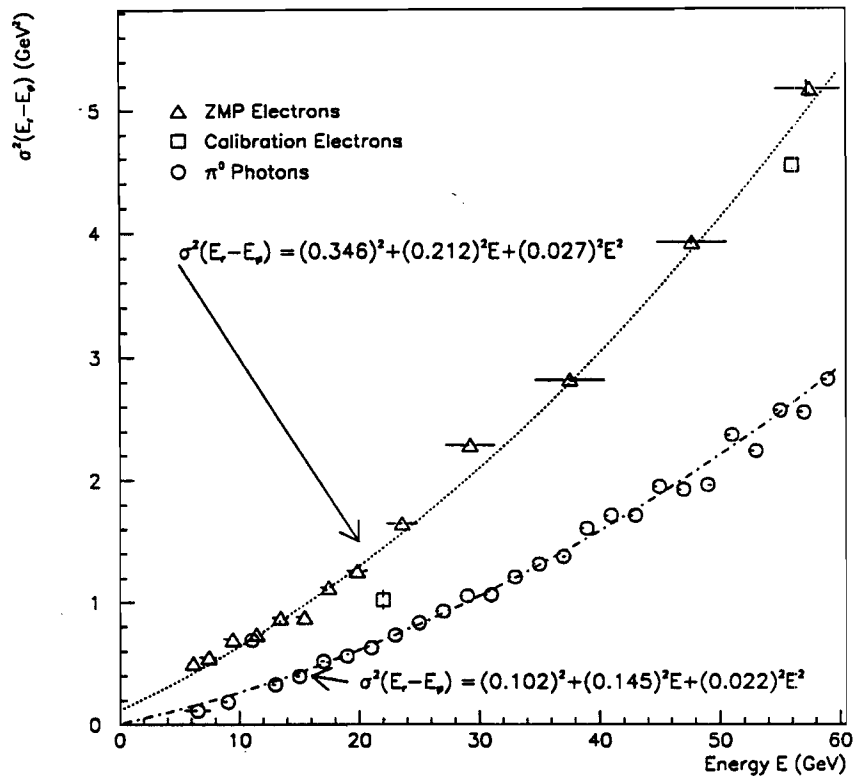


Figure 68: Plot of $\sigma^2(E_r - E_\phi)$ vs Energy for ZMP Electron and π^0 Photon Showers in the EMLAC

incoherent noise term is different for the two cases but the fits are not extraordinarily sensitive variations of a factor of two in this term.

The difference in resolution between photons and electrons may be from the fact that the shower shape used for reconstruction was optimized for π^0 photons and not ZMP electrons. The fact that electrons start showering earlier than photons may also play a role. On average, electrons deposit more of their energy before the LAC than photons because of this. EMREC will reconstruct an electron shower as it would a photon, but the resulting energy is then lower

than it should be. This shifts the energy scale down resulting in higher $\sigma^2(E_r - E_\phi)$ for electrons than photons with the same incident energy.

As can be seen, $\sigma^2(E_r - E_\phi)$ for electrons from the calibration is not very different from what was found for the ZMP data. The calibration data had an additional cut that allowed only single peak groups to be used. This was included in an attempt to eliminate electrons that might have undergone bremsstrahlung. The result may have been to artificially narrow the distribution.

VIII.10.3 HALAC Energy Resolution

The Monte Carlo estimate of HALAC resolution using charged pions of incident momenta of 50 to 200 GeV/c was found to be;

$$\frac{\sigma}{E} = (0.017 \pm 0.019) + \frac{(0.95 \pm 0.41)}{\sqrt{E}} \quad (52)$$

Analysis of the calibration data indicates that the energy resolution of the LAC for hadronic particles is $183\%/\sqrt{E}$ (See Fig.69)^[1].

VIII.11 Analysis of the Rest Masses for the π^0 and η

One of the crucial ways to pin down the energy resolution and scale of a calorimeter is to measure the rest mass of a known particle. In the case of the EMLAC, the π^0 mass is an ideal candidate for such a plot since it is produced in copious amounts. The π^0 rest mass is given by the formula;

$$m_{\pi^0}^2 = 2E_{\gamma 1}E_{\gamma 2}(1 - \cos \theta), \quad (53)$$

where m_{π^0} is the π^0 rest mass, $E_{\gamma 1}$ and $E_{\gamma 2}$ are the energies of the two photons from the pizero decay, and θ is the opening angle between the two photons. It can be clearly seen that good

[1] A. Sinanidas, op. cit., pp.108-138.

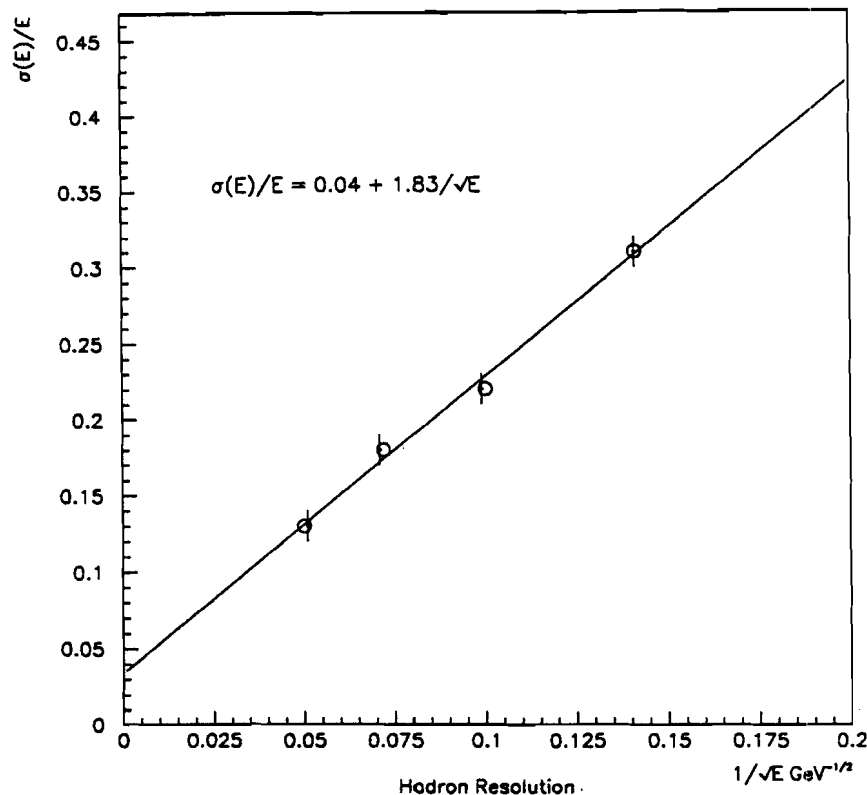


Figure 69: Plot of HALAC Energy Resolution from π^- Beam Calibration Studies

position and energy resolution are very important in measuring the rest mass. By turning the analysis around it is the measurement of the π^0 rest mass and its width that ultimately sets the energy scale and indicates what the resolution of the calorimeter is.

Figure 70 is a plot of the invariant two photon mass for combinations with a transverse momentum greater than 4.0 GeV. The energy scale has been set so that the π^0 peak lies near 135 GeV. In order to reproduce the observed width of the π^0 , the Monte Carlo needs intrinsic energy resolution of $20\%/\sqrt{E}$ without a gains term.

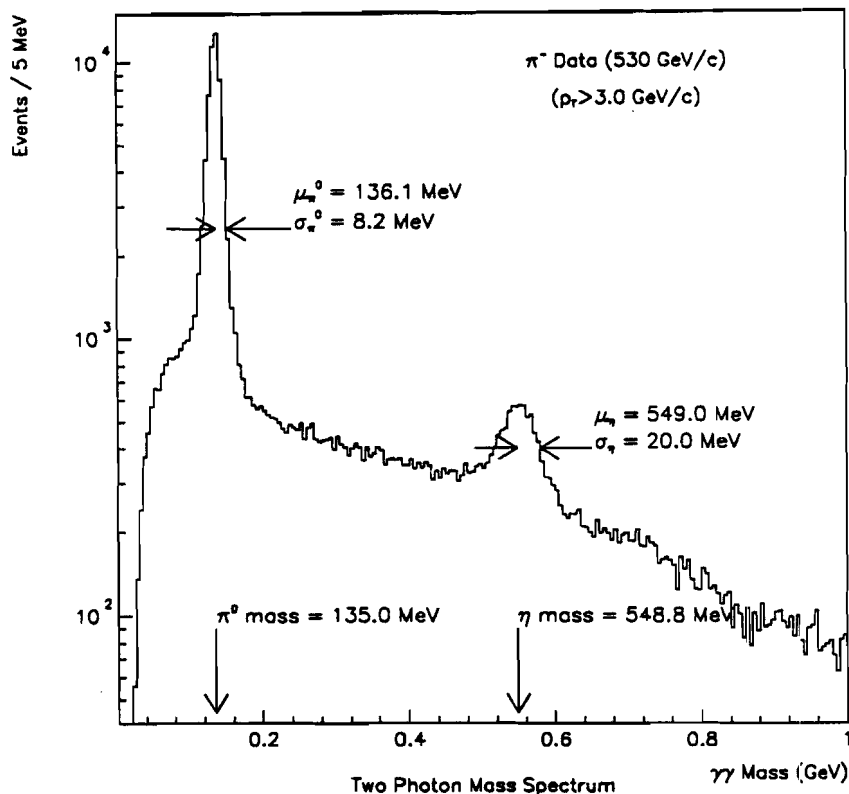


Figure 70: Plot of the Two Photon Invariant Mass for Photons with no Matching Tracks

The second peak in this plot occurs at the mass of the η . As can be seen the agreement between the measured mass and the accepted value is quite good. This is important since it indicates that there is only one energy scale for the calorimeter.

VIII.12 Particle Detection Efficiency

In order to have confidence that the LAC is capable of measuring the energy of an event, one needs to know how efficient it is in detecting incident particles. A plot of the matching efficiency between the tracks found in the PWCs and showers found in the LAC is useful for this purpose.

A track and a shower are said to match if the radial distance between a LAC shower and the projected position of the track at the face of the LAC is less than some maximum. Having previously found the spatial resolutions of the tracking system the EMLAC and the HALAC, the matching distances can be defined. For the EMLAC it is 1.5 cm and for the HALAC it is 12.0 cm.

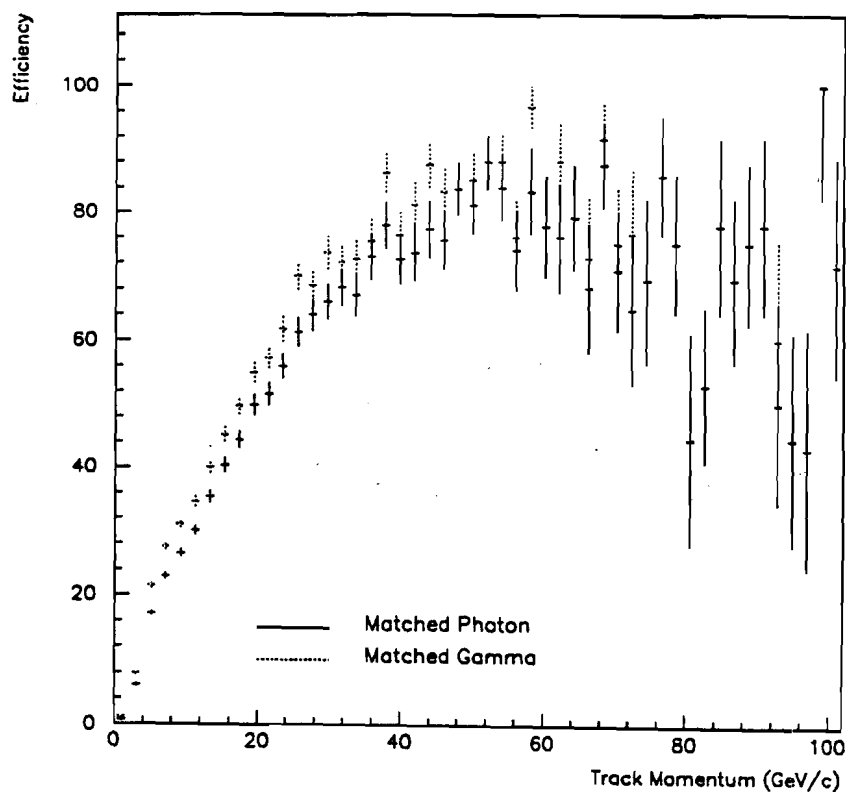


Figure 71: Plot of Detection Efficiency of the LAC for all Linked Tracks

Some care must be taken in selecting the tracks for which a match will be attempted. First of all their projected positions must lie within the active fiducial region of the LAC. Now since the track reconstruction program is capable of reconstructing a large number of fake PWC tracks for an event it is also prudent to require that the PWC track link with an SSD track. This reduces the likelihood that the track is a fake. Requiring that each PWC track have more than fifteen hits also helps to eliminate many of the fake tracks. A number of fake tracks may still remain, however, because the absolute percentage of fake tracks which remain after these cuts is not known at this time. As can be seen from Fig.71, the matching efficiency reaches only about 90% for all tracks which pass the fiducial and tracking cuts. This poor result could be due to a number of residual fake tracks or muons which have not interacted in the LAC. Muons can quite easily pass through the calorimeter without interacting and there has been no effort to remove them from the sample yet.

The discussion of efficiency up to this point has not distinguished between types of tracks. The data sample includes tracks from hadronic particles such as pions as well as from electromagnetic particles. The matching of hadronic tracks is of importance for studies of jets. Of greater interest, for direct photon studies, is the efficiency of the LAC in detecting electromagnetic particles, such as the photon or electron. Here again ZMPs can play an important role. A sample of high quality tracks can be garnered if the electron pair can be reconstructed together with a photon into a π^0 . Furthermore, if one ZMP track from each reconstructed π^0 matches a shower that is distinctly electromagnetic in character then the remaining ZMP tracks are most assuredly electrons. Figure 72 shows the matching efficiency for these ZMP electrons. The efficiency rises quickly but does not reach 100% until about 40 GeV. If the matching is extended to gamma pairs, that failed to be reconstructed because of correlation problems, then there is a significant improvement at energies below 40 GeV. Zero suppression may have a hand in this. The energy range over which this problem extends is similar to that for the zero suppression problem found in the E/P analysis. If either the r or ϕ strips in the back section of the calorimeter is

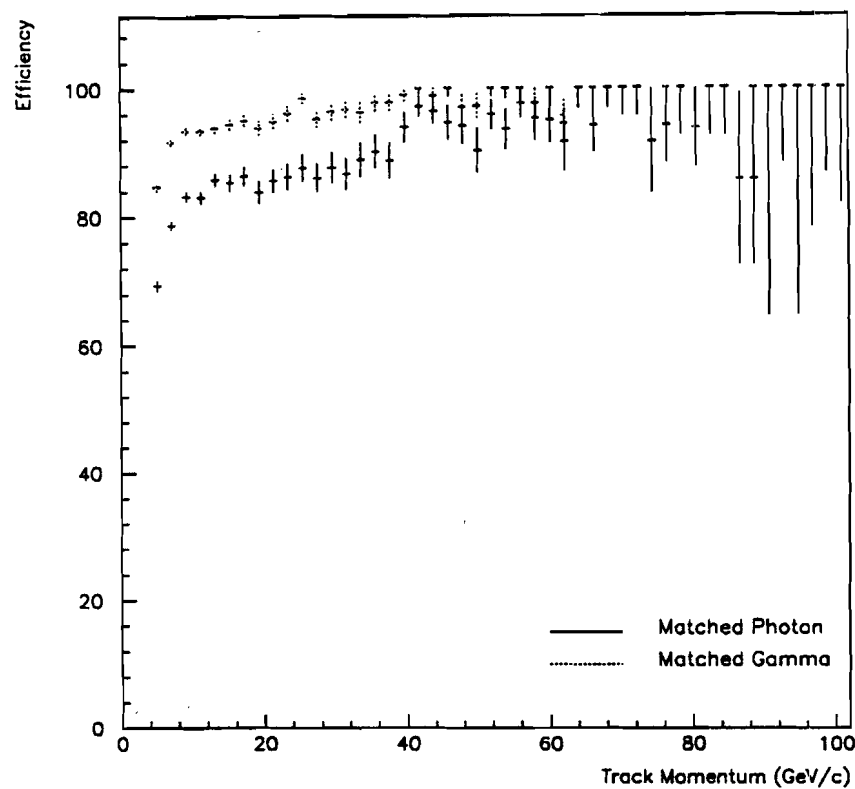


Figure 72: Plot of EMLAC ZMP Electron Detection Efficiency

experiencing a relatively larger amount of zero suppression, then the software may be having difficulties in correlating two gammas because of the disparities in their energies created by zero suppression.

Chapter IX

Conclusions

It is now time to summarize the performance characteristics of the LAC and compare them to the characteristics of calorimeters of similar design. A brief discussion of the remaining avenues of investigation will follow this. Finally a short section on, "If it were to be done all over again", will bring the discussion to an end.

IX.1 Summary of the Performance Characteristics of the LAC

The trigger to save the spectrometer data of an event is based on the p_T of a shower in the EMLAC. This shower could be caused by an electron, photon, muon, or hadron. To distinguish potential direct photon events from events triggered by other particles there are three principal shower parameters with which to make cuts. They are the directionality, the timing, and the E_{front}/E_{total} ratio. With a timing resolution of 9.4 ns and a directionality resolution of 0.22 cm, the vast majority of the muon events can be eliminated. This is critical since muons which escape detection by the veto wall are a major source of background to direct photon physics. To distinguish between hadronic and electromagnetic showers, a cut on the ratio E_{front}/E_{total} for the energy deposited in the EMLAC is useful. A cut on E_{front}/E_{total} at a value of 0.4 will put virtually all the electromagnetic showers above this value and 60% or more of the hadronic showers below it.

Once an event has been selected as a direct photon candidate the transverse momentum of the photon must be calculated. The transverse momentum of a photon is defined as $p_T = E \sin \theta$. Since the cross section for direct photon production falls steeply with p_T , it is crucial to know the error involved in measuring p_T . The uncertainty of the transverse momentum as a function

of energy (E) and position (X, Y, Z) is:

$$\left(\frac{\delta p_T}{p_T}\right)^2 = \left(\frac{\delta E}{E}\right)^2 + \left(\frac{Z^2}{X^2 + Y^2 + Z^2}\right)^2 \left(\frac{(X\delta X)^2 + (Y\delta Y)^2}{(X^2 + Y^2)^2} + \left(\frac{\delta Z}{Z}\right)^2\right) \quad (54)$$

The (X, Y) position resolution of the EMLAC for ZMP electrons is in reasonable agreement with results from Monte Carlo. The resolution is dependent on energy primarily because of material between the calorimeter and the target. The position resolution of the EMLAC is approximately a constant 0.06 cm for electrons with energy greater than 10 GeV. Similarly the position resolution for the HALAC is 3.0 cm. The resolution of the HALAC is expected to be worse than the EMLAC because of the larger lateral fluctuations of hadronic showers and because about 60% of the showers start somewhere in the EMLAC.

The incoherent noise, gains and intrinsic resolution terms for the energy resolution of photons have been determined and are listed in Eq.'s 55-57:

$$\sigma_{in}^2(E) = (0.083)^2 \times 72(1 - \exp(-0.014 \times (E + 9.6))), \quad (55)$$

$$\sigma_{it}^2(E) = 14.5\%E, \quad (56)$$

$$\sigma_{gn}^2(E) = 2.2\%E^2, \quad E \text{ in GeV.} \quad (57)$$

The coherent noise term has not been determined, although it might be extracted from a further analysis of E/P for ZMP electrons. The error of E/P can be calculated as follows.

$$\left(\frac{\delta(E/P)}{E/P}\right)^2 = \left(\frac{\delta E}{E}\right)^2 + \left(\frac{\delta P}{P}\right)^2. \quad (58)$$

Since $\sigma_{in}(E)$, $\sigma_{it}(E)$, and $\sigma_{gn}(E)$ are known then, if $\sigma(P)$ is known, $\sigma_{co}(E)$ can be extracted. This term may be position dependent. Amplifier oscillations were seen in the calibration data that affected individual amplifier cards. Thus the coherent noise could be very large or very small depending on whether the shower overlaps a card which oscillates or not. This might present difficulties for an E/P analysis where the ZMPs do not cover the face of the detector.

For hadronic showers the resolution of the LAC is much poorer than anticipated. The unexpectedly large noise level has played havoc with the small sampling ratio of the HALAC. The result is an energy resolution of $183\%/\sqrt{E}$ for hadrons.

Now that the uncertainties for E , X , Y , and Z are to a large extent known, the uncertainty in the p_T of a shower can be calculated. Since $\delta X = \delta Y$ and $R^2 = X^2 + Y^2$, Eq.54 can be reduced to:

$$\left(\frac{\delta p_T}{p_T}\right)^2 \approx \left(\frac{\delta E}{E}\right)^2 + \left(\frac{\delta X}{R}\right)^2 + \left(\frac{\delta Z}{Z}\right)^2 \quad (59)$$

A few quick calculations show that for electromagnetic showers the contribution of the X term to $(\delta p_T/p_T)^2$ is two orders of magnitude below that of the energy term and that the contribution of the Z term is another order of magnitude down from that. The upshot of this is that the uncertainty in the p_T of a shower is essentially a function of the uncertainty in the energy:

$$\left(\frac{\delta p_T}{p_T}\right)^2 \approx \left(\frac{\delta E}{E}\right)^2 \quad (60)$$

For hadrons that shower only in the HALAC this is not true. Despite the poor energy resolution, one needs to retain the X term when calculating the uncertainty in p_T because it is comparable in size to the energy term.

When the cross section is being calculated, the number of events in each p_T bin must be weighted appropriately by a number of things. Among these is the detection efficiency of the LAC for showers. The LAC is approximately 80% efficient in detecting incident tracks of 40 GeV/c or greater. This includes hadrons, muons, electrons, and any fake tracks, remaining after cuts, in an event. If the scope is limited to just electromagnetic showers, which are of the most interest, then the LAC is nearly 100% efficient above 40 GeV/c and about 85% efficient below this point. This comes from the matching efficiency of the LAC in detecting ZMP electron tracks. If ZMP tracks are matched to uncorrelated gamma pairs then the efficiency rises to 95% below 40 GeV/c. This indicates a flaw in the reconstruction program. There may also be some relation to the

back energy problem discovered in the E/P analysis. Now that the performance of the LAC has been outlined, it would be interesting to compare it to calorimeters of similar construction

I.1.1 Comparison of LAC with other Liquid Argon Calorimeters

The most straight forward comparison of the LAC is with its immediate predecessor, the liquid argon calorimeter for Fermilab experiment E-629^[1]. This calorimeter had 2 mm lead absorber sheets and 2 mm argon gaps, which is a coarser sampling ratio than the EMLAC. This should not result a significantly different energy resolution (see Chapter III.1.2). The energy resolution for electrons of the E-629 calorimeter was parametrized by the equation:

$$\sigma^2(E) = (0.14)^2 E + (0.55)^2. \quad (61)$$

This is a slightly better result than achieved by the EMLAC for photons since Eq. 61 already contains the coherent noise term. One might have expected the situation to be reversed. However, with a nearly 2.4 radiation lengths (rl) of material between the target and the sensitive volume of the EMLAC, this is not a complete surprise.

The E-629 detector had a directionality resolution of ± 30 mr and a timing resolution of 6 ns. The EMLAC has superior directionality resolution but inferior timing resolution. The former is due to the finer lateral segmentation of the EMLAC while the latter might be the result of a less expensive electronics scheme for the EMLAC's TVCs. On the subject of hadron rejection the EMLAC has an edge. The thickness of the front sections of the two calorimeters are 10 rl for the EMLAC and 12.5 rl for the E-629 calorimeter. With an E_{front}/E_{total} cut of 0.4, the E-629 calorimeter rejects about 50% of its hadronic showers. This is a smaller percentage than achieved by the EMLAC. This is not surprising since the EMLAC is roughly seven times larger than the E-629 calorimeter in active area. This means the EMLAC is subject to larger

^[1] C. Nelson, op. cit..

systematic fluctuations in absorber and argon gap thickness. These and other effects will tend to degrade the energy resolution.

Finally, a comparison of position resolutions for the two calorimeters shows little difference for 50 GeV electrons. The EMLAC has a resolution of 0.55 mm and the E-629 calorimeter had a resolution of 0.58 mm. At an energy of 50 GeV one would not expect a big difference between the two detectors. Only at lower energies would the finer segmentation of the EMLAC result in an advantage.

A comparison of the LAC with a liquid argon calorimeter of substantially different structure can illustrate some of the trade-offs that one must balance when designing a calorimeter. The "MARS" detector was a prototype liquid argon calorimeter with 2.9 mm argon gaps and 0.9 mm aluminum absorbers^[2]. It was designed to reduce as much as possible the sampling fluctuations that limit the energy resolution for electromagnetic showers.

The energy resolution for this detector was found to be:

$$\sigma(E)/E = \sqrt{(0.08/E)^2 + (0.036/\sqrt{E})^2}. \quad (62)$$

The 3.6% intrinsic term is certainly much lower than the same term in the EMLAC. This detector has many more layers than the EMLAC (393 as opposed to 66). Even though the MARS detector had thirteen longitudinal subdivisions the channel capacitance was larger than that of the EMLAC which results in larger detector noise. Each subdivision also increases the number of electronics channels needed and thus the cost of the detector unless larger strip widths are used as in the MARS detector which used 6 cm wide strips. This results in substantially worse position resolution as evidenced by resolution achieved by the MARS detector of:

$$\sigma(x) = \sqrt{(38.5/E)^2 + (12.8/\sqrt{E})^2}. \quad (63)$$

^[2] Claudio Cerri, et.al., "MARS, A Fine Grain Aluminum-Liquid Argon Calorimeter", *Nuclear Instruments and Methods*, Vol. 214, pp. 217-235, 1983.

This would clearly be unsatisfactory for direct photon physics because the background from π^0 's would rise drastically.

IX.2 Remaining Avenues of Investigation

The most important question to answer is why E/P falls off from one as track momenta increase beyond 75 GeV/c. A determination needs to be made whether this is a problem with the tracking system or the EMLAC. In view of the fact that $\sigma^2(E_r - E_\phi)$ for the π^0 photon data deviates from the fit to the data above 75 GeV, this may well be a problem with the EMLAC. The question then remains, why? A related issue is why the EMREC consistently reconstructs energy 12% lower than the deposited energy for Monte Carlo electrons. A correction for E/P below 30 GeV needs further study before it can be implemented. In particular, the effect of the amount of energy in the back section of the calorimeter on the E/P ratio needs careful scrutiny. The zero suppression employed by the electronics is certainly a suspect in this energy region.

Another conundrum to solve is the difference in the energy resolution for electrons and photons. One might expect a difference at lower energies because electrons start to shower earlier. This would shift the energies down for the electrons relative to the photons causing larger $\sigma^2(E_r - E_\phi)$ for electrons. This difference should disappear at large energies and the curves should converge, not diverge as they do. To study this, the problems discovered in the E/P analysis need to be solved and duplicated by Monte Carlo. Then a detailed comparison of electron and photon showers can be conducted.

Among the less urgent problems to be dealt with, there are still some small misalignments of the calorimeter to be corrected for. Any rotation of the calorimeter with respect to the spectrometer coordinate system has yet to be measured and corrected for. Also, as shown in Chapter VII.12, an answer for why the detection efficiency of the EMLAC falls off below 30 GeV needs to be found. There appears to be some problem, within the reconstruction program, in correlating the r and ϕ section of the detector. Here again zero suppression may be part of the

problem. Most of the problems listed so far could potentially be corrected for in the analysis software. Unfortunately there are some things that can only be corrected for by changes in the hardware.

IX.3 Changes in the LAC that would Improve Performance

If one were to start over and build the calorimeter from scratch there are several things one might do differently. The single most important thing to change is the LAC trigger electronics. A more effective suppression of the positive image charge signal would work wonders in improving the global p_T trigger efficiency. Diodes with a smaller turn on voltage would help remedy the problem to some extent. To get at the source of the problem the lead absorbers could be replaced by multiplanar devices that would in essence be large capacitors. This would be very much like the solution used in the HALAC. This would not completely eliminate the positive going signal from the image charge, but would most probably result in a drastic reduction of its size. New manufacturing techniques in the production of lead plate would be required to maintain the present sampling ratio. This would be no small undertaking.

Next on the list would be to replace the EMLAC signal cables with lower capacitance cables and to measure the charge injection capacitors on all the LACamp calibration circuits. Signal cables with lower capacitance would significantly reduce the channel noise in the EMLAC. This would reduce the constant term in $\sigma^2(E)$. Knowing the capacitance of the LACamp charge injectors would provide a better software correction to the gains by removing a large source of uncertainty. This would greatly enhance the energy resolution at high energies by reducing the size of the quadratic term in $\sigma^2(E)$.

The problems with the HALAC are intrinsic to the structure of the device. Amplifier noise is the dominant problem with the HALAC. Too small a sampling ratio coupled with the large pad capacitances is a bad recipe for a good signal to noise ratio. The cookies could be restructured so that the argon sampling would effectively double. Using thinner steel absorber plates would

allow a finer sampling of the showers, further increasing the sampling ratio. Reducing the pad size would decrease the amplifier noise but would require larger electronics costs. The lines used to readout the pads should be made thinner to reduce capacitive pickup and the crosstalk between pads that it incurs. A more radical improvement would be to adjust the e/h ratio so that it is closer to one. This might require combining the EMLAC and HALAC into a single calorimeter. The degradation of the energy resolution for electromagnetic showers would seriously affect the ability to do direct photon physics with such a calorimeter.

In conclusion, it is fair to say the EMLAC performs in a manner that is adequate for direct photon physics. The energy resolution has some room for improvement and with further study of some remaining problems this may come to pass. The EMLAC's most vexing problem is in the affect of image charge on the trigger electronics. Improved trigger modules may alleviate much of this problem in the next data run. The HALAC is of marginal usefulness at moderate energies because of its large noise problem. This makes it difficult to measure the energy of neutral baryons which was part of its original purpose. The HALAC should still be of use in measuring the energy of high energy hadrons. This is important for energies greater than 150 GeV were the tracking resolution becomes worse than the energy resolution of the HALAC. A plan to improve the channel amplifiers could make the HALAC much more effective device. The use of lower noise amplifiers would improve the energy resolution. A significant improvement would allow the HALAC to more accurately measure hadrons of moderate energies. Failing this, only a drastic restructuring of the device would ensure that it performed at an adequate level.

Bibliography

Abramowicz, H., et. al., "The Response and Resolution of an Iron-Scintillator Calorimeter for Hadronic and Electromagnetic Showers between 10 GeV and 140 GeV", *Nuclear Instruments and Methods*, V180, pp. 429-439, (1981).

Advanced Research Projects Agency and the Cryogenics Division of the National Bureau of Standards, "Mechanical, Thermal, Electrical and Magnetic Properties of Structural Materials", *Handbook on Materials for Superconducting Machinery*, p. 8.1.3-6.1(11/76), (1974).

Altarelli G., and G. Parisi, "Asymptotic Freedom in Parton Language", *Nuclear Physics*, Vol.B126, pp.298-318, (1977).

Amaldi, Ugo, "Fluctuations in Calorimetry Measurements", *Physica Scripta*, Vol.23, pp.409-424, (1981).

Baier, R., J. Engels, and B. Peterson, "Correlation with Large Transverse Momentum Photons and Gluon Structure Functions", *Zeitschrift fur Physik C Particles and Fields*, Vol. 6, pp. 309-316, (1980).

Benson, R. S., "Characteristics of Forward Energy Production in Proton-Nucleus and Pion-Nucleus Collisions at $\sqrt{S} = 31.5$ GeV", *University of Minnesota Thesis*, (1989).

Berger, E. L., E. Braaten, and R. D. Field, "Large- p_T Production of Single and Double Photons in Proton-Proton and Pion-Proton Collisions", *Nuclear Physics B*, Vol. 239, pp.52-92, (1984).

Bromberg, Carl, *E-706 Internal Note 94*.

Carimalo, C., et.al, "Direct-Photon Pair Production in Hadron Collisions as a Check of QCD", *Physics Letters*, Vol.98B, No.1,2, pp.105-109, (1981).

Cerri, Claudio, et.al., "MARS, A Fine Grain Aluminum-Liquid Argon Calorimeter", *Nuclear Instruments and Methods*, Vol. 214, pp. 217-235, 1983.

Chicago Bridge and Iron Co., *Dewar Insulation Note*, Ref No.851553.

Contogouris, A. P., S. Papadopoulos, and C. Papavassiliou, "Large- p_T Direct Photon and Opposite-Side Photon-Hadron Correlations in QCD", *Nuclear Physics*, Vol. B179, pp. 461-476, (1981).

Cormell, L. and J. F. Owens, "High- p_T Production of Direct Photons and Jets in Quantum Chromodynamics", *Physical Review D*, Vol. 22, No. 7, pp. 1609-1616, (1980).

Crowley, A. and T. Ferbel, "Signal-Cabling and Feed-Through System for LAC, E-706 Internal Note 119.

Gross, David J. and Frank Wilczek, "Asymptotically Free Gauge Theories", *Physical Review D*, Vol. 8, No. 10, p. 3633, (1973).

Duke D. W. and J.F. Owens, "Q²-Dependent Parameterizations of Parton Distribution Functions", *Physical Review D*, Vol. 30, No. 1, pp. 49-45, (1984).

Dunlap, D., "Comments on Optimal Strip Width of LAC", *E-706 Internal Note 042*.

Dunlap, Dave, "How Front/Back Separations Affect the Shower Shape", *E-706 Internal Note 075*.

Fabjan, C. W. and T. Ludlam, "Calorimetry in High-Energy Physics", *Annual Review of Nuclear and Particle Science*, Vol. 32, pp. 335-389, (1982).

Ferbel, Tom, "Comment on Front/Back Separation for EMLAC", *E-706 internal note 056*.

Ferbel, Tom, "Remarks on E706 Calorimetry", *E-706 Internal Note 049*, (1982).

Ferbel, T. and W. R. Molzon, "Direct Photon Production in High-Energy Collisions", *Reviews of Modern Physics*, p. 181, (1984).

Gabriel, T. A., et.al., "", *Nuclear Instruments and Methods*, Vol. 134, p. 271.

Ginther, G., *Private Communication*.

Glaubman, Mike, "The Liquid Argon Hadron Calorimeter", *E-706 Internal Note 063*, (1983).

Gutierrez, P. and D. Skow, "Test of Trigger Electronics", *E-706 Internal Note 099*.

Halzen, F., M. Dechantsreiter, and D. M. Scott, "Structure of Direct-Photon Events", *Physical Review D*, Vol. 22, No. 7, (1980).

Hartman, K., *Private Communication*.

Hossain S., "Hadronic Shower Simulation in E706 Calorimeter", *E-706 Internal Note 051*, (1983).

Hossain, S., E. Pothier, and G. Ballocchi, "Photon Reconstruction in E706 Liquid Argon Calorimeter", *E-706 Internal Note 130*, (1985).

Huston, J., "Some Remarks on E706 Calorimetry", *E-706 Internal Note 055*, (1983).

Kasen, M. B. et al., "Mechanical, Electrical, and Thermal Characterization of G-10CR and G-11CR Glass-Cloth/Epoxy Laminates Between Room Temperature and 4 K" *Advances in Cryogenic Engineering Materials* (New York: Plenum Press, 1980), p.241.

Kourbanis, I., *Private Communication*.

Krawczyk, M. and W. Ochs, "Direct and Indirect Production of Photon, Lepton, and Hadron Pairs in Hadron-Hadron Collisions", *Physics Letters*, Vol.79B, No.1,2, pp.119-122, (1978).

Owens, J. F., "Large-Momentum-Transfer Production of Direct Photons, Jets and Particles", *Reviews of Modern Physics*, Vol.59, No.2, pp.465-503, (1987).

Lanaro, Armando, "A Liquid Argon Ionization Chamber for Testing Samples of Constituent Materials for the E706 LAC", *E-706 Internal Note 138*.

Lirakis, C., G. Fanourakis, "Cryogenic Tests of the Hadron Calorimeter", *E-706 Internal Note 150*, (1986).

Lobkowicz, F., "Superlad", *E-706 Internal Note 002*, (1981).

Lobkowicz, F., *E-706 Internal Note 004*, (1981).

Lukens, P. and K. Ruddick, *E-706 Internal Note 141*.

Mani, S., et al., *E-706 Internal Note 125*.

Mansour, J. P., " π^0 Production from π^- and P Beams at 530 Gev/c on Be and Cu", *University of Rochester Thesis*, Chapter IV, (1989).

Mathur, N. and S. Augst, "Measurements of Impedance of Gore Cable and Matching Amplifier", *E-706 Internal Note 123*.

Merritt, F. S., et. al., "Hadron Shower Punchthrough for Incident Hadrons of Momentum 15, 25, 50, 100, 200, and 300 GeV/c", *Nuclear Instruments and Methods*, Vol A245, pp. 27 - 34, (1986).

Miller, L. S., S. Howe, W. E. Spear, "Charge Transport in Solid and Liquid Ar, Kr, and Xe", *Physical Review*, Vol 166, No. 3, pp. 871-878, (1968).

Nelson, C., "Operational Performance of a Large Liquid Argon Photon Calorimeter", *Nuclear Instruments and Methods*, Vol. 216, pp. 381-391, (1983).

Nowak, M. and M. Praszalowicz, "Direct Photon Production Beyond Leading Log Approximation - $q + q \rightarrow \gamma + q + q$ Contribution", *Zeitschrift fur Physik C Particles and Fields*, Vol.17, pp.249-257, (1983).

Prebys, E., *Private Communication*.

Prebys, E. and F. Lobkowicz, "High Voltage Dependence of Signals in LAC", *E-706 Internal Note 163..*

Schneier, Bruce, "Results of Leakage Tests on Cryogenic Capacitors at High Voltages", *E-706 Internal Note 078*, (1983).

Schumacher, Earle E. and G. S. Phipps, "Some Physical and Metallurgical Properties of Lead-Calcium Alloys for Storage Cell Grids and Plates", *Trans. Electrochem. Soc.*, Vol. 68 (1935), p.309-319.

Sinanidis, A., " A Study of Particles Produced with High Transverse Momentum Single Photons and π^0 's in Hadronic Collisions", *Northeastern University Thesis*, Chapter 5.9, (1989).

Skow, D. D. "Feed for the RABBIT-E-706 *Internal Note 157*.

Slattery, Paul, et.al., " A Proposal to Measure Direct Photon Production at Tevatron Energies", *FNAL document P695/P706*, pp.3-8, (1981).

Touloukian, Y. S. and C. Y. Ho eds., "Thermal Expansion of Metallic Elements and Alloys", *Thermophysical Properties of Matter, The TPRC Data Series*, Vol. 12, p. 178, Plenum Pub., New York, (1975).

Touloukian, Y. S. and C. Y. Ho eds., "Thermal Expansion of Nonmetallic Materials", *Thermophysical Properties of Matter, The TPRC Data Series*, Vol. 13, p. 1443, Plenum Pub., New York, (1975).

Walker, R. L., "Identification of π^0 , η , and X^0 , CTSI internal Report, May 14, 1971.

Wigmans, R., "On the Energy Resolution of Uranium and Other Hadron Calorimeters", *Nuclear Instruments and Methods*, Vol. A259, pp. 389-429, (1987).

Willis, W. J. and V. Radeka, "Liquid-Argon Ionization Chambers as Total-Absorption Detectors", *Nuclear Instruments and Methods*, Vol. 120, pp. 221-236, (1974).

Yosef, C., "Production of High Transverse Momentum Neutral Pions in Hadronic Collisions", *Northeastern University PhD. Thesis* in preparation.